

Study of the CP violation angle ϕ_3
using DK decay modes of B meson

Department physics, Tohoku University

Naoki Kikuchi

Version 2.71

Abstract

In this thesis, I report the study of $B \rightarrow DK$ decay, using a data sample of 366 million $B\bar{B}$ pairs recorded at the $\Upsilon(4S)$ resonance with the Belle detector at the KEKB asymmetric e^+e^- storage ring. Several suppressed $B \rightarrow DK$ decays are measured. Moreover the constraints for ϕ_3 by these measurements are discussed.

Contents

1	Introduction	4
1.1	CKM model	4
1.1.1	$B^0 - \bar{B}^0$ mixing and Time-dependent CP violation	6
1.1.2	Direct CP violation	8
1.2	Determination of ϕ_3	9
1.2.1	Dalitz analysis	10
1.2.2	GWL method	10
1.2.3	ADS method	12
2	Belle detector and KEKB accelerator	15
2.1	KEKB accelerator	15
2.2	Silicon Vertex Detector / SVD	19
2.3	Central Drift Chamber / CDC	21
2.4	Aerogel Čerenkov Counter / ACC	23
2.5	Time Of Flight / TOF	27
2.6	Electromagnetic Calorimeter / ECL	30
2.7	Solenoid Magnet	31
2.8	K_L/μ Detector / KLM	31
2.9	Trigger and DAQ	34
2.10	Monte Carlo	36
3	$B^- \rightarrow DK^-$ analysis	37
3.1	Data set	37
3.2	Event selection criteria	37
3.2.1	Primary charged tracks	37
3.2.2	D reconstruction	38
3.2.3	B^- reconstruction	39
3.2.4	$q\bar{q}$ continuum backgrounds suppression	43
3.2.5	Peaking backgrounds	48
3.3	Results	52
3.3.1	Fitting the ΔE distributions	52

3.3.2	Ratio of branching fractions R_{Dh}	53
3.3.3	Charge separated yield	56
3.3.4	Constraint for ϕ_3	59
4	$B^- \rightarrow DK^{*-}$ analysis	62
4.1	Event selection criteria	62
4.1.1	K^{*-} reconstruction	62
4.1.2	B^- reconstruction	63
4.1.3	$q\bar{q}$ continuum background suppression	64
4.1.4	Peaking background	66
4.2	Results	66
4.2.1	Fitting the ΔE distributions	66
4.2.2	Ratio of branching fractions R_{Dh}	70
4.2.3	Charge separated yield	71
4.2.4	Constraint for ϕ_3	74
5	$B^- \rightarrow D^*K^-$ analysis	76
5.1	Event selection criteria	76
5.1.1	D^{*-} reconstruction	76
5.1.2	B^- reconstruction	77
5.1.3	$q\bar{q}$ continuum background suppression	77
5.1.4	Peaking background	82
5.2	Results	82
5.2.1	Fitting the ΔE distributions	82
5.2.2	Ratio of branching fractions R_{Dh}	87
5.2.3	Constraint for ϕ_3	87
6	Combining fit result	89
7	Conclusions	90
A	Cotinumum background suppression	93
B	Figure of merit technique	96

Chapter 1

Introduction

CP violation in the standard model is explained by Cabibbo-Kobayashi-Masukawa model [1]. Its effects are able to be parametalized by unitarity triangle on $\rho - \eta$ plane. These angels and sides are related to physics process which fortunately appear in B decays. So measurements of these are the precise test for the standard model(SM).

1.1 CKM model

The violation of symmetry between matter and anti-matter attract many physicists and had not be able to solve. But Kobayashi and Maskawa solve that problem by introducing 6 quarks of 3 generations within the SM framework.

The interaction lagrangian is given by

$$\mathcal{L}_{int}(x) = -\frac{g}{\sqrt{2}}\bar{\mathcal{U}}_{L,i}\gamma^\mu V_{CKM,ij}\mathcal{D}_{L,j}W_\mu + h.c. \quad (1.1)$$

where

$$\bar{\mathcal{U}} = \left(u \quad c \quad t \right), \quad \mathcal{D} = \begin{pmatrix} d \\ s \\ b \end{pmatrix}, \quad (1.2)$$

subscript L means light-handed part of these quark states, and

$$V_{CKM} = \begin{pmatrix} V_{ud} & V_{us} & V_{ub} \\ V_{cd} & V_{cs} & V_{cb} \\ V_{td} & V_{ts} & V_{tb} \end{pmatrix}. \quad (1.3)$$

In the above formalism quark states are states which diagonalize electro-weak interaction. But generally mass eigenstates(\mathcal{U} and \mathcal{D}) differs from them and are given by

$$\mathcal{U} = U_u^\dagger \mathcal{U}, \quad \mathcal{D} = U_d^\dagger \mathcal{D} \quad (1.4)$$

and U is related to V_{CKM} through

$$V_{CKM} = U_u^\dagger U_d \quad (1.5)$$

which gives quark-mixing.

There are many parameterization methods which define relative quark phase of V_{CKM} matrix elements. One of popular approximation methods is that of Wolfenstein [2] which is

$$V_{CKM} = \begin{pmatrix} 1 - \frac{\lambda^2}{2} & \lambda & A\lambda^3(\rho - i\eta) \\ -\lambda & 1 - \frac{\lambda^2}{2} & A\lambda^2 \\ A\lambda^3(1 - \rho - i\eta) & -A\lambda^2 & 1 \end{pmatrix} \quad (1.6)$$

where λ , A , ρ and η are real parameter. In this parameterization λ is Cabibo-suppression-factor and related to Cabibo angle as

$$\lambda \equiv \sin \theta_c. \quad (1.7)$$

λ and A are experimentally well measured. But ρ and η have not been measured with accurately. So its measurements is main subject of B -factory experiment, Belle and BaBar.

In the SM, CKM matrix should be unitary for probability conservation law. The orthogonality of d -column and b -column lead to a relation as

$$V_{ud}V_{ub}^* + V_{cd}V_{cb}^* + V_{td}V_{tb}^* = 0. \quad (1.8)$$

Since these terms are generally complex numbers, this relation can be represented as a triangle in a complex plane. Usually the triangle is defined as bellow

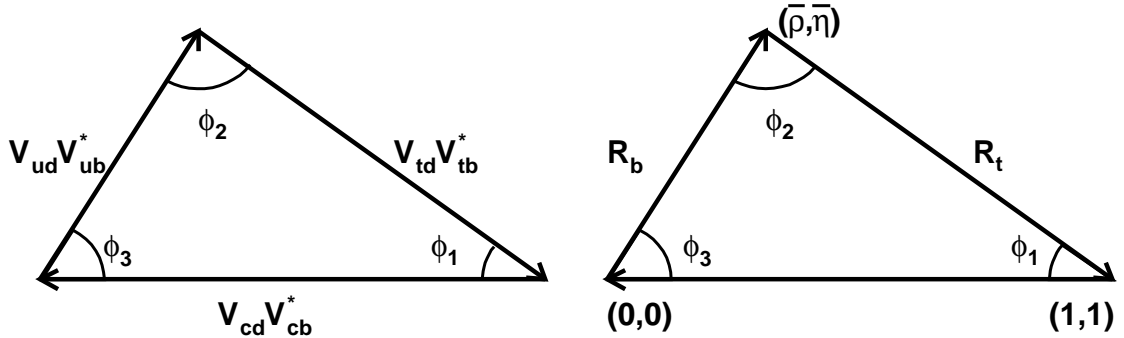


Figure 1.1: Unitarity triangle

where

$$\phi_1 \equiv \pi - \arg\left(\frac{V_{td}V_{tb}^*}{V_{cd}V_{cb}^*}\right) \quad (1.9)$$

$$\phi_2 \equiv \arg\left(\frac{V_{td}V_{tb}^*}{-V_{ud}V_{ub}^*}\right) \quad (1.10)$$

$$\phi_3 \equiv \arg\left(\frac{V_{ud}V_{ub}^*}{-V_{cd}V_{cb}^*}\right). \quad (1.11)$$

If Wolfenstein parameterization is used, that triangle converts to the triangle on $\rho - \eta$ plane as shown in Figure 1.1(right) where

$$\bar{\rho} \equiv \left(1 - \frac{\lambda^2}{2}\right)\rho \quad (1.12)$$

$$\bar{\eta} \equiv \left(1 - \frac{\lambda^2}{2}\right)\eta. \quad (1.13)$$

and sides are represented as

$$R_b \equiv \sqrt{\bar{\rho}^2 + \bar{\eta}^2} \quad (1.14)$$

$$R_t \equiv \sqrt{(1 - \bar{\rho})^2 + \bar{\eta}^2}. \quad (1.15)$$

All these elements are determined from B decays such as shown in Table 1.1.

	elements	decay mode
	ϕ_1	$B^0 \rightarrow J/\psi K^0$
angle	ϕ_2	$B^0 \rightarrow \pi^+\pi^-$
	ϕ_3	$B^- \rightarrow DK^-$
	V_{td}	$B \rightarrow \rho\gamma$
slide	V_{ub}	$B \rightarrow X_u l \nu$
	V_{cb}	$B \rightarrow X_c l \nu$

Table 1.1: Relationship between CKM elements and B decays

1.1.1 $B^0 - \bar{B}^0$ mixing and Time-dependent CP violation

assuming a time-evolutions of state are given by only linear-combination of basis, B^0 and \bar{B}^0 , it should be written as

$$i\frac{d}{dt} \begin{pmatrix} B^0 \\ \bar{B}^0 \end{pmatrix} = H \begin{pmatrix} B^0 \\ \bar{B}^0 \end{pmatrix} = \begin{pmatrix} H_{11} & H_{12} \\ H_{21} & H_{22} \end{pmatrix} \begin{pmatrix} B^0 \\ \bar{B}^0 \end{pmatrix} \quad (1.16)$$

Assuming the eigenstates of H are

$$B_H = pB^0 + q\bar{B}^0 \quad (1.17)$$

$$B_L = pB^0 - q\bar{B}^0 \quad (1.18)$$

and their eigenvalues are

$$\lambda_H = m_H - i\frac{\gamma_H}{2} \quad (1.19)$$

$$\lambda_L = m_L - i\frac{\gamma_L}{2}. \quad (1.20)$$

Then their time-evolution are given by

$$i\frac{d}{dt}B_{H,L} = \lambda_{H,L}B_{H,L} \quad (1.21)$$

$$\rightarrow B_{H,L}(t) = e^{-i\lambda_{H,L}t}B_{H,L}(0) \quad (1.22)$$

and these time-evolution can be converted to

$$B^0 = \frac{1}{2p}(B_H + B_L) \rightarrow B^0(t) \equiv \frac{1}{2p}(e^{-i\lambda_H t}B_H + e^{-i\lambda_L t}B_L) \quad (1.23)$$

$$\bar{B}^0 = \frac{1}{2q}(B_H + B_L) \rightarrow \bar{B}^0(t) \equiv \frac{1}{2q}(e^{-i\lambda_H t}B_H - e^{-i\lambda_L t}B_L) \quad (1.24)$$

and

$$B^0(t) = \frac{1}{2}[(e^{-i\lambda_H t} + e^{-i\lambda_L t})B^0 + \frac{q}{p}(e^{-i\lambda_H t} - e^{-i\lambda_L t})\bar{B}^0] \quad (1.25)$$

$$\overline{B^0(t)} = \frac{1}{2}[(e^{-i\lambda_H t} + e^{-i\lambda_L t})B^0 + \frac{p}{q}(e^{-i\lambda_H t} - e^{-i\lambda_L t})\bar{B}^0]. \quad (1.26)$$

In this line if we assume $\gamma_H \simeq \gamma_L \simeq \gamma$,

$$\bar{m} \equiv \frac{m_H + m_L}{2}, \quad \delta m \equiv m_H - m_L \quad (1.27)$$

$$\rightarrow e^{-i\lambda_H t} \pm e^{-i\lambda_L t} = e^{-imt}e^{-\frac{\gamma}{2}t}(e^{-i\frac{\delta m}{2}t} \pm e^{i\frac{\delta m}{2}t}) \quad (1.28)$$

$$= e^{-imt}e^{-\frac{\gamma}{2}t} \begin{pmatrix} 2 \cos \frac{\delta m}{2}t \\ -2i \sin \frac{\delta m}{2}t \end{pmatrix} \quad (1.29)$$

$$B^0(t) = e^{-\frac{\gamma}{2}t}(B^0 \cos \frac{\delta m}{2}t - i\frac{q}{p}\bar{B}^0 \sin \frac{\delta m}{2}t) \quad (1.30)$$

$$\overline{B^0(t)} = e^{-\frac{\gamma}{2}t}(\bar{B}^0 \cos \frac{\delta m}{2}t - i\frac{p}{q}B^0 \sin \frac{\delta m}{2}t) \quad (1.31)$$

This shows $B^0 - \bar{B}^0$ mixing.

Next let's consider time-dependent CP violation. In this case we assume B^0 and \bar{B}^0 decay to same final state and these amplitudes are defined as

$$A \equiv \langle f|H|B^0 \rangle \quad (1.32)$$

$$\bar{A} \equiv \langle f|H|\bar{B}^0 \rangle. \quad (1.33)$$

Then the amplitude of B^0 decay to f in t , $A_{B^0 \rightarrow f}(t)$, is given by

$$A_{B^0 \rightarrow f}(t) = e^{-\frac{\gamma}{2}t} \left(A \cos \frac{\delta m}{2}t - i \frac{q}{p} \bar{A} \sin \frac{\delta m}{2}t \right) \quad (1.34)$$

$$= A e^{-\frac{\gamma}{2}t} \left(\cos \frac{\delta m}{2}t - i \rho \bar{A} \sin \frac{\delta m}{2}t \right) \quad (1.35)$$

$$A_{\bar{B}^0 \rightarrow f}(t) = e^{-\frac{\gamma}{2}t} \left(\bar{A} \cos \frac{\delta m}{2}t - i \frac{p}{q} A \sin \frac{\delta m}{2}t \right) \quad (1.36)$$

$$= \bar{A} e^{-\frac{\gamma}{2}t} \left(\cos \frac{\delta m}{2}t - i \rho^{-1} \sin \frac{\delta m}{2}t \right) \quad (1.37)$$

where

$$\rho \equiv \frac{q\bar{A}}{pA}. \quad (1.38)$$

We define

$$A \equiv \frac{|\rho|^2 - 1}{|\rho|^2 + 1}, S \equiv \frac{2\text{Im}\rho}{|\rho|^2 + 1} \quad (1.39)$$

and then decay rates are calculated as

$$\Gamma_{B^0 \rightarrow f} = \frac{|A|^2}{2} (|\rho|^2 + 1) e^{-\gamma t} [1 - A \cos \delta m t + S \sin \delta m t] \quad (1.40)$$

$$\Gamma_{\bar{B}^0 \rightarrow f} = \frac{|A|^2}{2} \left| \frac{p}{q} \right|^2 (|\rho|^2 + 1) e^{-\gamma t} [1 + A \cos \delta m t - S \sin \delta m t]. \quad (1.41)$$

$$(1.42)$$

This equations show time-dependent CP violation (experimentally $|\frac{p}{q}|^2 \sim 1$).

1.1.2 Direct CP violation

Direct CP violation means $\Gamma_{B \rightarrow f} \neq \Gamma_{\bar{B} \rightarrow \bar{f}}$. It is occurred by interference of multiple decay diagrams which have different weak-phase and non-zero strong phase as shown in Figure 1.2.

In this case these amplitudes are written as

$$A_{B \rightarrow f} = A_1 + A_2 e^{i\theta_W} e^{i\delta} \quad (1.43)$$

$$A_{\bar{B} \rightarrow \bar{f}} = A_1 + A_2 e^{-i\theta_W} e^{i\delta} \quad (1.44)$$

where θ_W is the relative CP violating weak phase between two diagrams and δ is the non-CP violating strong phase.

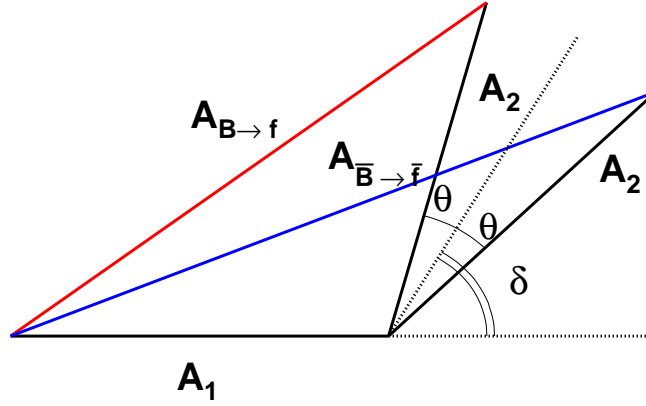


Figure 1.2: Mechanism of direct CP violation

Then the decay rates is calculated as

$$\Gamma(B \rightarrow f) = |A_1|^2 + |A_2|^2 + 2|A_1||A_2| \cos(\delta + \theta_W) \quad (1.45)$$

$$\Gamma(\bar{B} \rightarrow \bar{f}) = |A_1|^2 + |A_2|^2 + 2|A_1||A_2| \cos(\delta - \theta_W) \quad (1.46)$$

This shows direct CP violation.

In a measurement of direct CP violation if those amplitude (A_1 and A_2) are comparable, large CP violation effect is expected.

1.2 Determination of ϕ_3

The determination of ϕ_3 is still challenging, even if we use high luminosity B -factory. This is because ϕ_3 measurements needs a diagram which includes V_{ub} and it strongly suppresses a decay amplitude.

ϕ_3 is defined as

$$\phi_3 \equiv \arg\left(\frac{V_{ud}V_{ub}^*}{-V_{cd}V_{cb}^*}\right) \sim \arg(-V_{ub}), \quad (1.47)$$

where noted that in Wolfenstein parameterization (1.6), V_{ub} is the only one in the expression that has a complex phase. The measurement of ϕ_3 is equivalent to the measurement of the phase of $-V_{ub}$. Therefore we measure it through an interference between $b \rightarrow u(B^- \rightarrow \bar{D}^0(\rightarrow f)K^-)$ and $b \rightarrow c$ transition($B^- \rightarrow D^0(\rightarrow f)K^-$), where \bar{D}^0 and D^0 decay into a same final state, f .

1.2.1 Dalitz analysis

Up to now, Dalitz analysis [3] is the one which gives a most strict constraint for ϕ_3 . This analysis uses $B^- \rightarrow D[K_s\pi^+\pi^-]K^-$ decay modes and Dalitz distribution of $K_s\pi^+\pi^-$ daughters.

Dalitz distributions are given by

$$B^- : \quad M_-(m_-^2, m_+^2) = f(m_-^2, m_+^2) + r_B e^{i(\delta-\phi_3)} f(m_+^2, m_-^2) \quad (1.48)$$

$$B^+ : \quad M_+(m_+^2, m_-^2) = f(m_+^2, m_-^2) + r_B e^{i(\delta+\phi_3)} f(m_-^2, m_+^2), \quad (1.49)$$

where $m_-(m_+)$ is a invariant mass of $K_s\pi^-(K_s\pi^+)$, f is density function of m_- and m_+ , and r_B is a ratio of $B^- \rightarrow \bar{D}^0 K^-$ and $B^- \rightarrow D^0 K^-$ decay. the density function f is determined from charm-tagged continuum process $e^+e^- \rightarrow c\bar{c}$ events assuming 15 resonances (two-body decays such as $K^*(892)^\pm\pi^\mp$, $K_0^*(1430)^\pm\pi^\mp$, $K_2^*(1430)^\pm\pi^\mp$, $K^*(1680)^\pm\pi^\mp$, $K_S\rho$, $K_S\omega$, $K_S f_0(980)$, $K_S f_0(1370)$, $K_S f_2(1270)$, $K_S\sigma_1$ and $K_S\sigma_2$) and 1 non-resonance components as

$$f(m_+^2, m_-^2) = \sum_{j=1}^{15} a_j e^{i\alpha_j} \mathcal{A}_J(m_+^2, m_-^2) + b e^{i\beta}, \quad (1.50)$$

where j stands for j -th resonance, a_j and b are amplitudes, α_j and β are relative phase, and $\mathcal{A}_J(m_+^2, m_-^2)$ is the density functions of each resonances.

For example in above expression for B^- Dalitz distribution $f(m_-^2, m_+^2)$ ($f(m_+^2, m_-^2)$) is a contribution from $B^- \rightarrow D^0 K^-$ ($B^- \rightarrow \bar{D}^0 K^-$). If the CP violating phase ϕ_3 does not exist, $M_-(m_-^2, m_+^2)$ and $M_+(m_+^2, m_-^2)$ are symmetric for m_- and m_+ . While if there is a certain size ϕ_3 , we can measure it thorough the difference of Dalitz distributions as shown in Figure 1.3.

However this method has a fault. It is the large model dependence. Belle collaboration measured ϕ_3 using this method and the result [4] is

$$\phi_3 = 77^\circ_{-19^\circ}^{+17^\circ}(\text{stat}) \pm 13^\circ(\text{syst}) \pm 11^\circ(\text{model}). \quad (1.51)$$

This model dependence comes from the determination of the density function f . To determine the relative phase α_j , we use only each branching fractions. So we can not avoid assuming models to determine it.

1.2.2 GWL method

One of GWL method [5] feature is no model dependence such as Dalitz analysis.

We can determine ϕ_3 using interference between $b \rightarrow u$ and $b \rightarrow c$ decay processes which has same final state. One of interesting final state of D decays is CP eigenstate

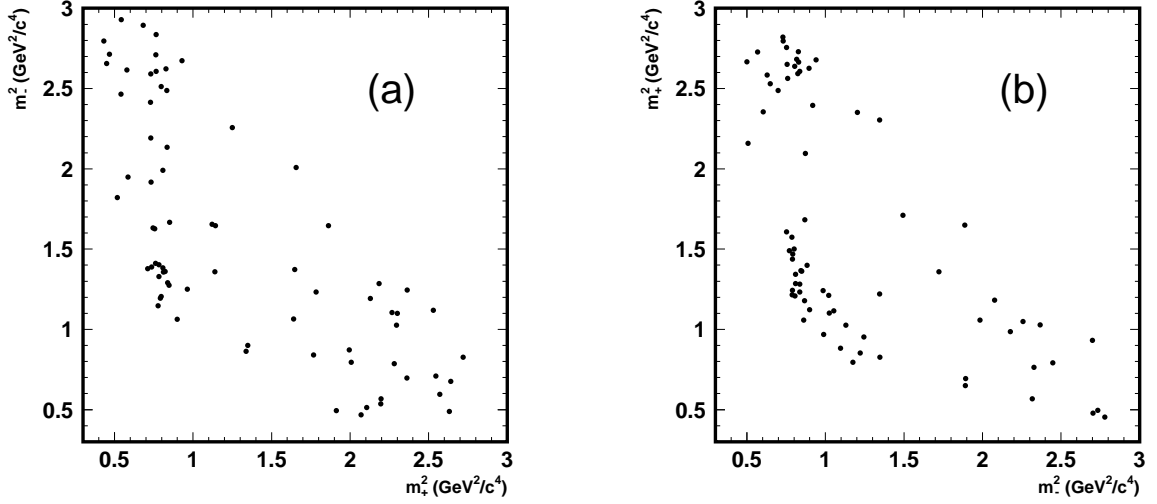


Figure 1.3: Dalitz distribution of $D \rightarrow K_s \pi^+ \pi^-$ from $B^+ \rightarrow DK^+$ (a) and $B^- \rightarrow DK^-$ (b). $m_-(m_+)$ is a invariant mass of $K_s \pi^- (K_s \pi^+)$. [4]

such as K^+K^- , $\pi^+\pi^-$ (CP-even eigenstates called D_1) and $K_s \pi^0$, $K_s \omega$, $K_s \phi$, $K_s \eta$ (CP-odd eigenstate called D_2). Since CP phase convention is arbitrary, following the phase convention $CP(D^0) = \bar{D}^0$, CP eigenstate D mesons are represented as

$$D_{1,2} = \frac{D^0 \pm \bar{D}^0}{\sqrt{2}}$$

So amplitude of $B^- \rightarrow D_{1,2}K^-$ is given by

$$A(B^- \rightarrow D_{1,2}K^-) = \frac{1}{\sqrt{2}}[A(B^- \rightarrow D^0K^-) \pm A(B^- \rightarrow \bar{D}^0K^-)]$$

In this equation, the angle between these amplitudes is given by (without strong phase δ)

$$\theta = \arg\left(-\frac{V_{ub}V_{cs}^*}{V_{cb}V_{us}}\right) \sim \arg(-V_{ub})$$

where noted that in Wolfenstein parameterization (1.6), V_{ub} is the only one in the expression that has a complex phase.

So amplitudes of $B^\mp \rightarrow D_{1,2}K^\mp$ are written as

$$A(B^- \rightarrow D_1K^-) = \frac{1}{\sqrt{2}}[|A(B^- \rightarrow D^0K^-)| + e^{-i\phi_3}e^{+i\delta}|A(B^- \rightarrow \bar{D}^0K^-)|] \quad (1.52)$$

$$A(B^+ \rightarrow D_1K^+) = \frac{1}{\sqrt{2}}[|A(B^+ \rightarrow D^0K^+)| + e^{+i\phi_3}e^{+i\delta}|A(B^+ \rightarrow \bar{D}^0K^+)|] \quad (1.53)$$

$$A(B^- \rightarrow D_2 K^-) = \frac{1}{\sqrt{2}} [|A(B^- \rightarrow D^0 K^-)| - e^{-i\phi_3} e^{+i\delta} |A(B^- \rightarrow \bar{D}^0 K^-)|] \quad (1.54)$$

$$A(B^+ \rightarrow D_2 K^+) = \frac{1}{\sqrt{2}} [|A(B^+ \rightarrow D^0 K^+)| - e^{+i\phi_3} e^{+i\delta} |A(B^+ \rightarrow \bar{D}^0 K^+)|] \quad (1.55)$$

where $\delta (\equiv \delta_D - \delta_{\bar{D}})$ is strong phase difference between $B^- \rightarrow D^0 K^-$ and $B^- \rightarrow \bar{D}^0 K^-$ decay.

By these amplitude observable values which have sensitivity for CP violation are derived as bellow

$$A_{1,2} \equiv \frac{\mathcal{B}(B^- \rightarrow D_{1,2} K^-) - \mathcal{B}(B^+ \rightarrow D_{1,2} K^+)}{\mathcal{B}(B^- \rightarrow D_{1,2} K^-) + \mathcal{B}(B^+ \rightarrow D_{1,2} K^+)} \quad (1.56)$$

$$= \frac{2r_B \sin \delta' \sin \phi_3}{1 + r_B^2 + 2r_B \cos \delta' \cos \phi_3} \quad (1.57)$$

$$R_{1,2} \equiv \frac{R^{D_{1,2}}}{R^{D^0}} \quad (1.58)$$

$$= 1 + r_B^2 + 2r_B \cos \delta' \cos \phi_3 \quad (1.59)$$

where

$$r_B \equiv \left| \frac{A(B^- \rightarrow D^0 K^-)}{A(B^- \rightarrow \bar{D}^0 K^-)} \right| \quad (1.60)$$

$$\delta' \equiv \begin{cases} \delta & \text{for } D_1 \\ \delta + \pi & \text{for } D_2 \end{cases} \quad (1.61)$$

$$R^{D_{1,2}} \equiv \frac{\mathcal{B}(B^\pm \rightarrow D_{1,2} K^\pm)}{\mathcal{B}(B^\pm \rightarrow D_{1,2} \pi^\pm)} \quad (1.62)$$

$$R^{D^0} \equiv \frac{\mathcal{B}(B^\pm \rightarrow \bar{D}^0 K^\pm)}{\mathcal{B}(B^\pm \rightarrow \bar{D}^0 \pi^\pm)}. \quad (1.63)$$

In these formalism we have 3 unknown values, r , δ' and ϕ_3 , and experimentally can get 3 independent equations (We can measure A_1 , A_2 , R_1 and R_2 , but one value is not independent because of the relation, $A_1 R_1 = -A_2 R_2$). So in principle we can solve this equation. However a fault of this method is a low sensitivity.

1.2.3 ADS method

A method which has more sensitivity of CP violation using other D decay mode is suggested [6]. It is doubly-Cabbibo-supressed decay mode such as $D^0 \rightarrow K^+ \pi^-$. Considering $B \rightarrow D[K^+ \pi^-]K^-$ there are two diagrams as shown in Figure 1.4.

Its CP asymmetry depends on the difference of decay amplitude between $B \rightarrow D^0[K^+ \pi^-]K^-$ and $B \rightarrow \bar{D}^0[K^+ \pi^-]K^-$. Actually its ratio is given by

$$\frac{\mathcal{B}(B \rightarrow D^0[K^+ \pi^-]K^-)}{\mathcal{B}(B \rightarrow \bar{D}^0[K^+ \pi^-]K^-)} \approx \lambda_c \left| \frac{V_{cb} V_{us}^*}{V_{ub} V_{cs}^*} \right|^2 \frac{\mathcal{B}(D^0 \rightarrow K^+ \pi^-)}{\mathcal{B}(\bar{D}^0 \rightarrow K^+ \pi^-)} \approx 1 \quad (1.64)$$

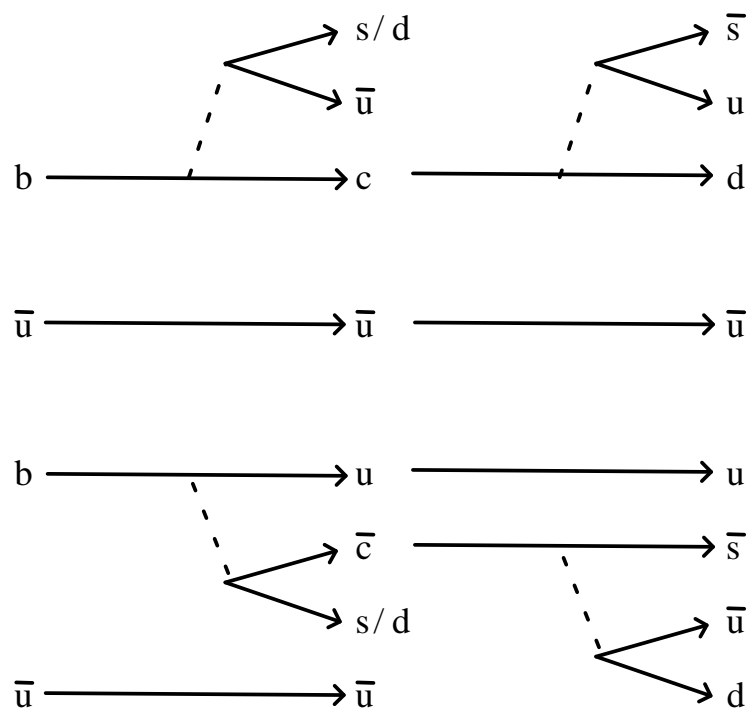


Figure 1.4: Feynman diagram of $B^- \rightarrow D[K^+\pi^-]K^-/\pi^-$ decay

where λ_c is color-suppression-factor ($\simeq 0.35$ [7]) and $\frac{\mathcal{B}(D^0 \rightarrow K^+ \pi^-)}{\mathcal{B}(D^0 \rightarrow K^+ \pi^0)} = 0.0060$ [8] from other experiment. As Figure 1.4 in this decay mode since two diagrams are comparable the interference effect is expected to be sizable. And these branching fractions are calculated as

$$\mathcal{B}(B^- \rightarrow [K^+ \pi^-] K^-) = (r_B^2 + r_D^2 + 2r_B r_D \cos(\delta - \phi_3)) |A_B|^2 |A_D|^2 \quad (1.65)$$

$$\mathcal{B}(B^+ \rightarrow [K^- \pi^+] K^+) = (r_B^2 + r_D^2 + 2r_B r_D \cos(\delta + \phi_3)) |A_B|^2 |A_D|^2 \quad (1.66)$$

where

$$r_B \equiv \left| \frac{A(B^- \rightarrow \bar{D}^0 K^-)}{A(B^- \rightarrow D^0 K^-)} \right| \quad (1.67)$$

$$r_D \equiv \left| \frac{A(D^0 \rightarrow K^+ \pi^-)}{A(D^0 \rightarrow K^- \pi^+)} \right| \quad (1.68)$$

$$A_B \equiv A(B^- \rightarrow D^0 K^-) \quad (1.69)$$

$$A_D \equiv A(D^0 \rightarrow K^- \pi^+) \quad (1.70)$$

$$\delta \equiv \delta_B + \delta_D \quad (1.71)$$

$\delta_B(\delta_D)$ is the strong phase difference between the two $B(D)$ decays.

We have already know r_D , A_B , A_D from other measurements and essentially the values we want to know are ϕ_3 , r_B and δ . if we combine another result of D decay mode such as $D \rightarrow K_S \pi^0$, we can get 4 equation. So we can solve this equation. Moreover if we combine more modes we can give a more strict constraint for ϕ_3 .

Chapter 2

Belle detector and KEKB accelerator

We need large $B\bar{B}$ samples to study sides and angles of CKM unitarity triangles thorough B -meson decays. Asymmetric e^+e^- collider KEKB at KEK(High energy Research Organization) can produce $B\bar{B}$ pairs with high luminosity. The Belle detector is a large-solid-angle spectrometer to accumulate the B -meson decays and have been constructed at the interaction point(IP) of KEKB.

In this chapter, details of the KEKB accelerator and the Belle detector are described and figures are taken from [9].

2.1 KEKB accelerator

The KEKB is specially designed to produce B -mesons with high luminosity. To determine the time-dependent CP violation we have to measure the time difference between CP-side and tag-side of B -meson decays. Since this time difference is too small to directly measure it, we measure it using Lorentz boost. So the KEKB is asymmetric e^+e^- collider. The energy of electron and positron beams are 8 GeV and 3.5 GeV, respectively. This is concerned to avoid ion trapping, which happens only at low energy, in electron ring. Its center-of-mass energy is 10.58 GeV, just $\Upsilon(4S)$ resonance, and the Lorentz boost parameter $\beta\gamma$ is 0.425. By this Lorentz boost B -meson can typically flight 200 μm which is measurable for experimentalists. The KEKB has two beam rings as shown in Figure 2.1. The electron ring is so-called HER(High Energy Ring) and the positron ring is so-called LER(Low Energy Ring). These rings located in TRINSTAN tunnel with circumference of about 3 km. A only interection point is located in Tsukuba Area. KEKB has a finite crossing angle of 11 mrad to avoid parasitic collision near the interaction point.

In Decemember 19th 2005, we archive $1.6270 \times 10^{34} \text{cm}^{-2} \text{s}^{-1}$ and our accumulated lunocity exceeded 0.5ab^{-1} .

	LER	HER	unit
Horizontal Emittance	18	24	nm
Beam current	1730	1261	mA
Number of bunches	1388		
Bunch current	1.25	0.909	mA
Bunch spacing	2.1		m
Bunch trains	1		
Total RF volatage Vc	8	15	MV
Synchrotron tune	-0.0249	-0.0226	
Betatron tune	45.505/43.535	44.511/41.577	
beta's at IP	59/0.65	56/0.62	cm
Estimated vertical beam size at IP	2.1	2.1	mm
beam-beam parameters	0.110/0.092	0.073/0.056	
Beam lifetime	140@1700	179@1261	min.@mA
Peak luminosity	15.62		$10^{33}/\text{cm}^2/\text{sec}$
Luminosity records	per day / 7days/ 30days 1.178/7.358/29.02		fb^{-1}

Table 2.1: The machine parameters of KEKB

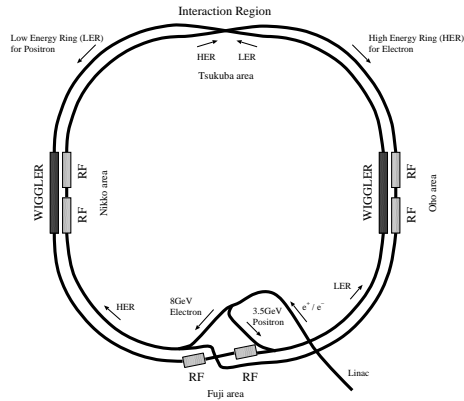


Figure 2.1: KEKB accelerator

Detector	Device	Configuration	Readout	Performance
Beam pipe	Beryllium double-wall	Cylindrical $r=2.0 \rightarrow 1.5\text{cm}$		Helium gas cooling Be/He/Be
SVD1	Double Sided Si Strip	3 layers, $300\mu\text{m}$ -thick $r=3.0 \sim 5.8\text{cm}$ $23^\circ < \theta < 139^\circ$	81.92K	$\sigma_{r-\phi} = 19 \oplus 54/p\beta \sin^{3/2} \theta \mu\text{m}$ $\sigma_z = 42 \oplus 44/p\beta \sin^{5/2} \theta \mu\text{m}$
↓ SVD2		4 layers, $300\mu\text{m}$ -thick $r=2.0 \sim 5.8\text{cm}$ $17^\circ < \theta < 150^\circ$	110.59K	$\sigma_{r-\phi} = 22 \oplus 36/p\beta \sin^{3/2} \theta \mu\text{m}$ $\sigma_z = 28 \oplus 32/p\beta \sin^{5/2} \theta \mu\text{m}$
CDC	Small Cell Drift Chamber	Anode: 50 layers Cathode: 3 layers $r=8 \sim 88\text{cm}$ $z=-79 \sim +160\text{cm}$	A: 8.4K C: 1.5K	$\sigma_t/p_t = (0.20p_t \oplus 0.29/\beta)\%$ $\sigma_{dE/dx} = 7\%$
ACC	Silica Aerogel $n=1.01 \sim 1.03$	Barrel: 960 Endcap: 228 FM-PMT readout	1,788	$K/\pi: 1.2 < p < 3.5\text{GeV}/c$
TOF	Scintillator	$\phi: 128$ segmentation $r=120\text{cm}$ Length=3m	128×2	$\sigma_t = 100\text{ps}$ $K/\pi: p < 1.2\text{GeV}/c$
TSC		$\phi: 64$ segmentation	64	
ECL	CsI(Tl)	Barrel: $r=125 \sim 162\text{cm}$ Endcap: $z=-102/+196\text{cm}$	6624 1152(FWD) 960(BWD)	$\sigma_E/E = 1.3\%/\sqrt{E}$ $\sigma_{pos} = 0.5\text{cm}/\sqrt{E}$
Solenoid magnet		$r=170\text{cm}$		Nb-Ti-Cu alloy B=1.5T
KLM	RPC	Barrel: 14 layers Endcap: 15 layers	$\theta: 16\text{K}$ $\phi: 16\text{K}$	$K_L: \Delta\theta, \Delta\phi = 30\text{mrad}$
EFC	BGO	$2 \times 1.5 \times 12\text{cm}^3$	$\theta: 5$ $\phi: 32$	

Table 2.2: Sub-detectors of Belle detector

Belle

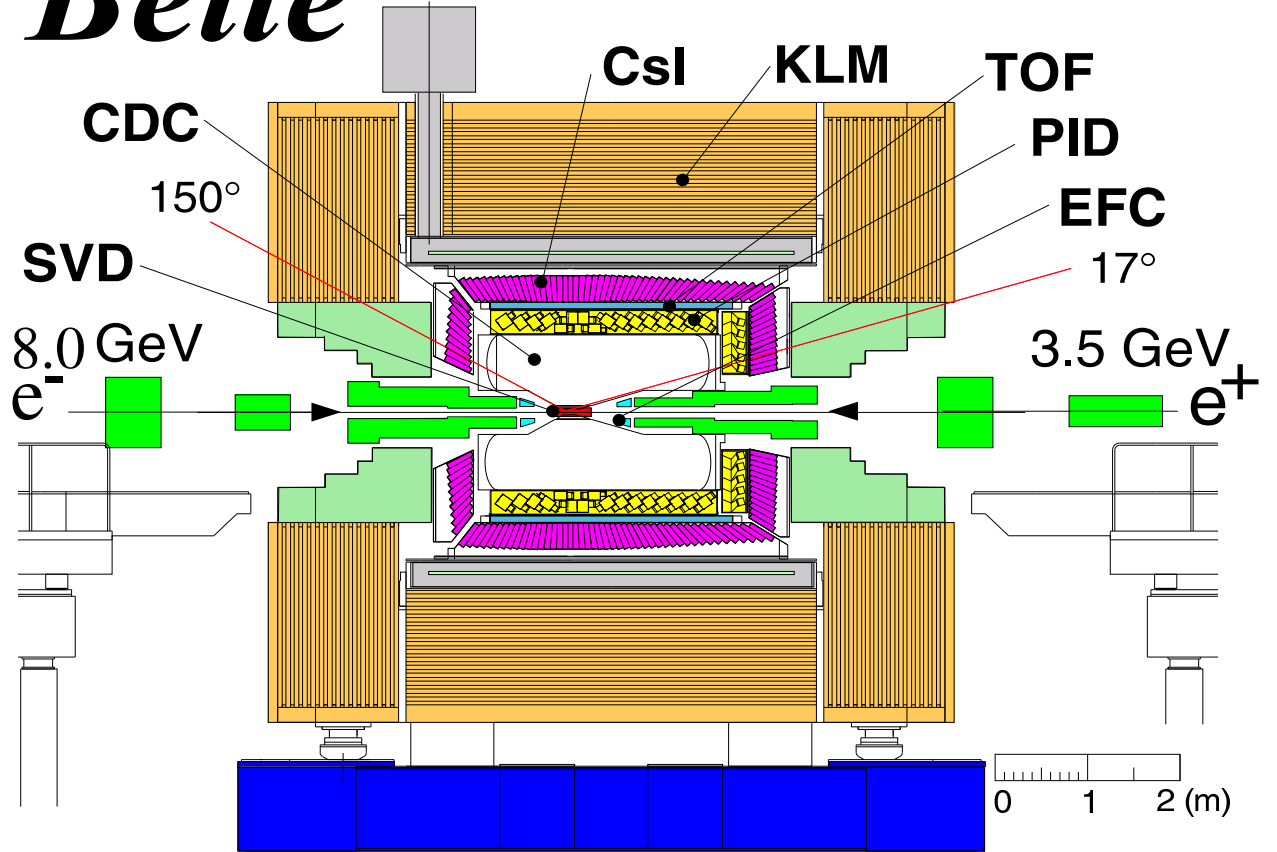


Figure 2.2: Side view of Belle detector

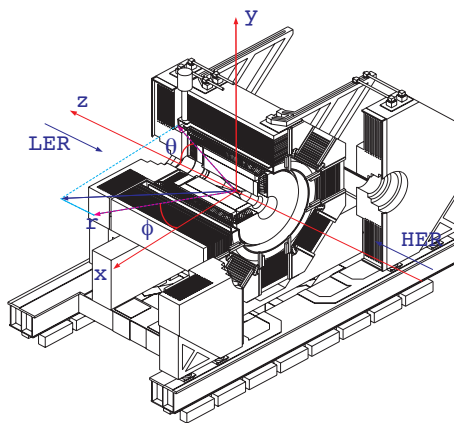


Figure 2.3: The definition of belle coordinate

2.2 Silicon Vertex Detector / SVD

SVD is located in most inner part of Belle. Its main purposes are vertexing of B -meson decay points. SVD is most important detector to measure time-dependent CP violation. We measure time-dependent CP violation through measurements of z position difference in two B -mesons decays.

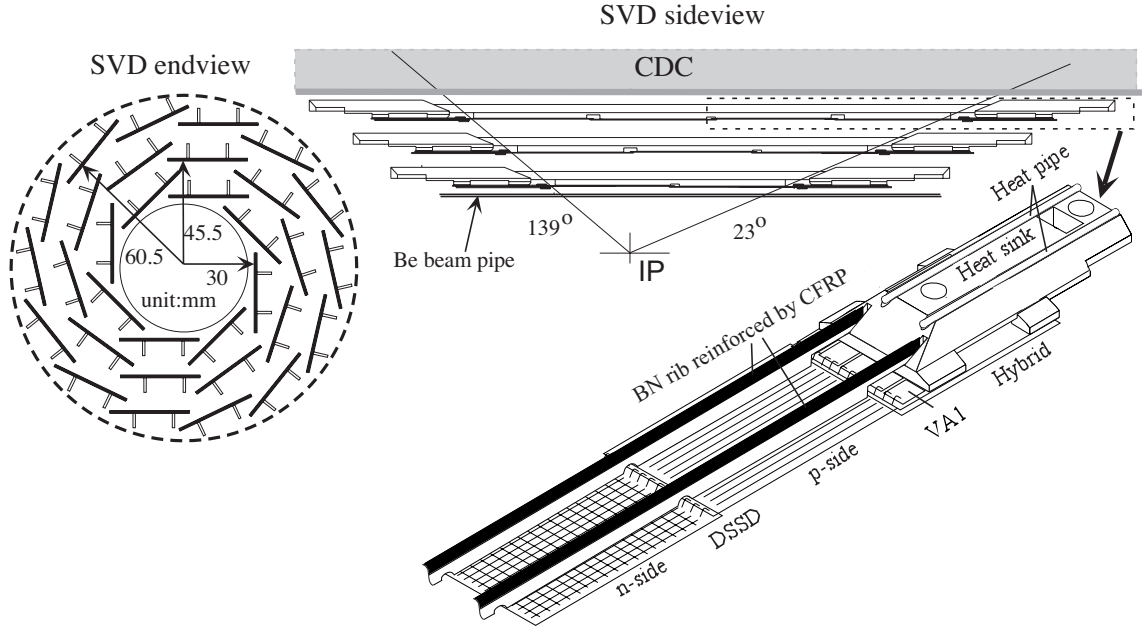


Figure 2.4: SVD1 configuration

Belle used SVD1 and is using SVD2. SVD1 is designed to have radiation tolerance up to 1 MRad. Since in summer of 2002 its radiation exceeds its limitation, SVD is replaced. In that time some up-grade is also applied for SVD. Its main feature is not only increase of radiation tolerance but also close to IP in order to improve vertex resolution.

	SVD1	SVD2
number of layers	3	4
radius of inner layer	3.0 cm	2.0 cm
acceptance	$23^\circ < \theta < 139^\circ$	$23^\circ < \theta < 139^\circ$

Table 2.3: Comparison of SVD1 and SVD2

Figure 2.5 and Figure 2.6 shows a configuration of SVD2. SVD2(SVD1) has 4(3) cylindrical detectino layers consisting units of Double-sided Silicon Strip Detectors(so-called

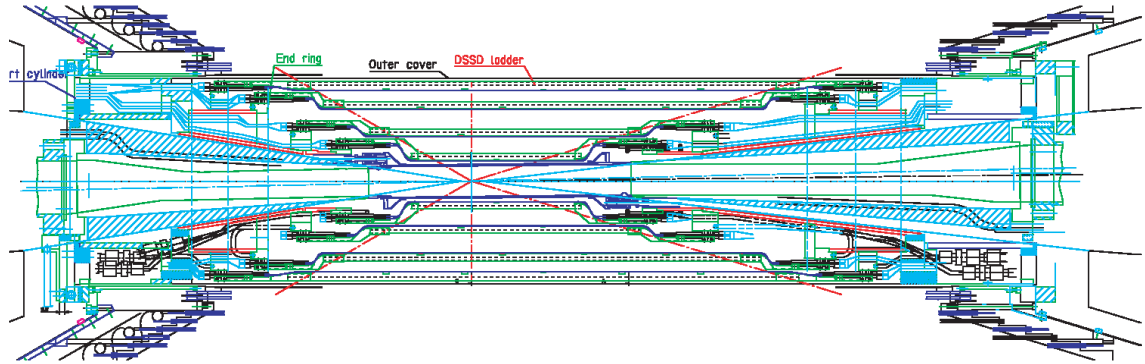


Figure 2.5: Side view of SVD2

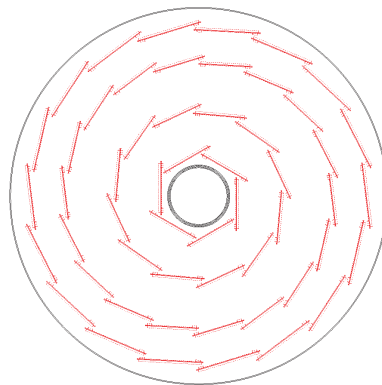


Figure 2.6: End view of SVD2

DSSD) with $300 \mu\text{m}$ thickness. As shown in Figure 2.7 the impact parameter resolution at IP for SVD1 is

$$\sigma_{r-\phi} = (19.2 \oplus \frac{54.0}{p\beta} \sin^{3/2} \theta) \mu\text{m}$$

$$\sigma_z = (42.2 \oplus \frac{31.9}{p\beta} \sin^{5/2} \theta) \mu\text{m}$$

and in the case of SVD2 one is

$$\sigma_{r-\phi} = (21.9 \oplus \frac{35.5}{p\beta} \sin^{3/2} \theta) \mu\text{m}$$

$$\sigma_z = (27.8 \oplus \frac{31.9}{p\beta} \sin^{5/2} \theta) \mu\text{m}$$

where the first term is detector native resolution, the second term is an effect of coulomb multiple scattering and \oplus stands for quadratic-sum.

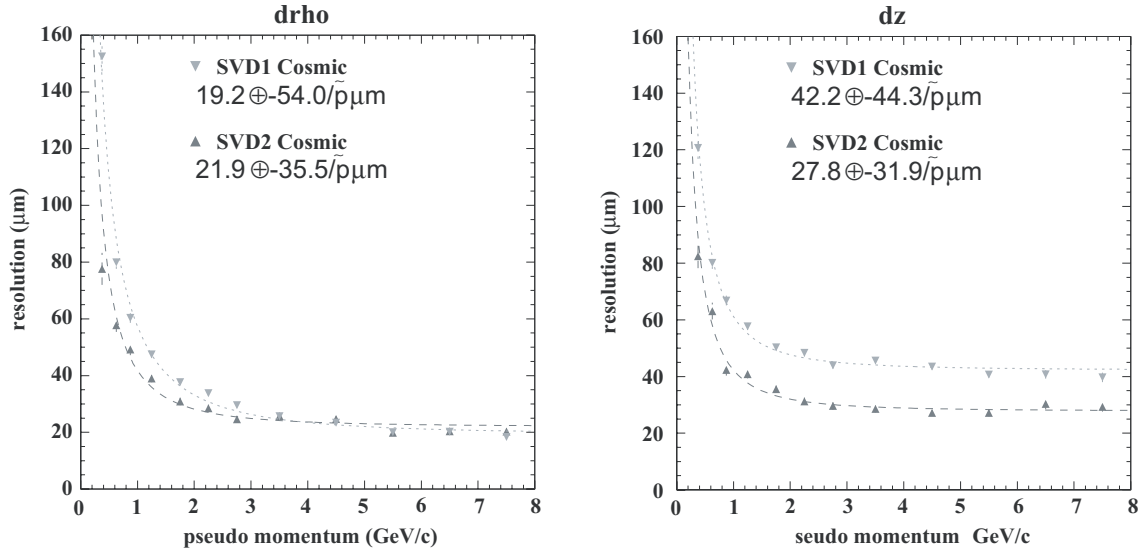


Figure 2.7: Impact parameter resolution of SVD for $r - \phi$ and z

2.3 Central Drift Chamber / CDC

Roles of CDC are tracking, momentum measurements and particle identification (PID) using dE/dx measurements of charged tracks.

Figure 2.8 shows configuration of CDC. CDC covers the polar angle region $17^\circ < \theta < 150^\circ$ and the region from 8cm to 88cm in the direction of radial. CDC has a total of 50

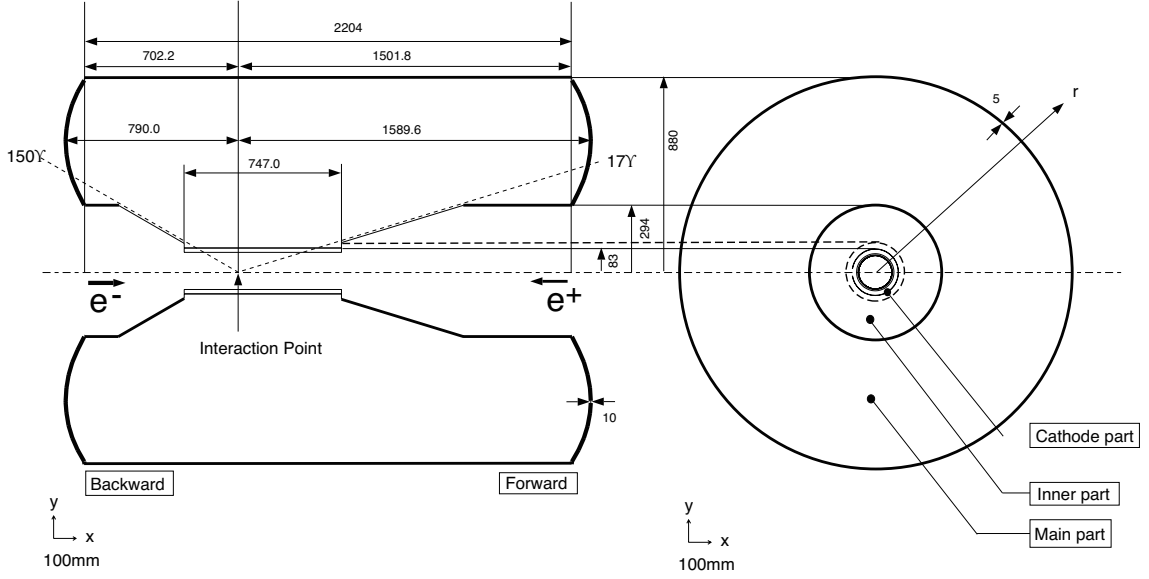


Figure 2.8: CDC configuration

sense wire layers (32 axial wire layers and 18 stereo wire layers) and 3 cathode strip layers. The stereo angles range from 42.5 mrad to 72.1 mrad. A 50% helium-50% ethane gas mixture is used in CDC. In order to minimize Coulomb multiple scatterings, a gas which has low atomic number is selected. It contributes to good momentum determinations.

The spatial resolution is about 130 μm . The transverse momentum resolution is

$$\sigma_t/p_t = (0.20p_t \oplus 0.29/\beta)\%$$

In CDC the measurement of dE/dx plays an important role for particle identification. The kind of particles are distinguished by the difference of energy loss in the drift chamber which is given by the Bethe-Bloch formula as

$$-\frac{dE}{dx} = \frac{4\pi N_0 z^2 e^4 Z}{mv^2 A} \left[\ln\left(\frac{2mv^2}{I(1-\beta^2)}\right) - \beta^2 \right]$$

where

- N_0 : Avogadro's number
- Z : atomic number
- A : the atoms mass number of gas
- I : effective ionization potential
- m : mass of passing particle

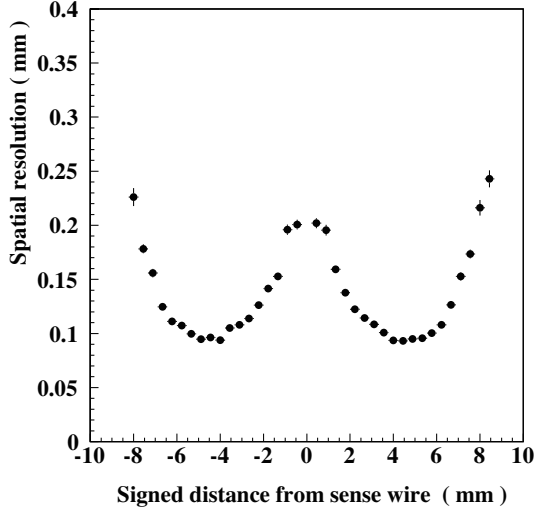


Figure 2.9: CDC spatial resolution

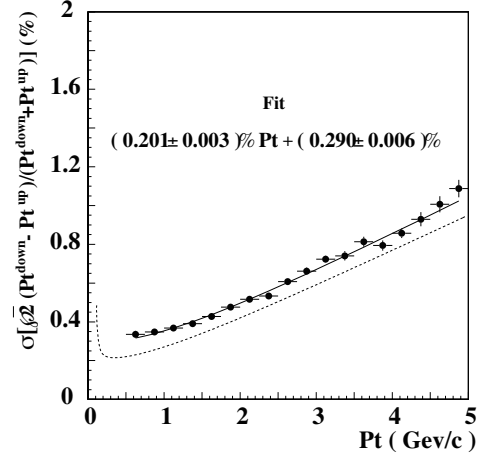


Figure 2.10: CDC momentum resolution

Actually some kind of particles are separated by dE/dx measurements as shown in Figure 2.11. Of course, CDC also has enough dE/dx resolution to identify the kind of particle effectively as shown in Figure 2.12.

2.4 Aerogel Čerenkov Counter / ACC

ACC is a threshold Čerenkov Counter. ACC is also the sub-detector for particle identification and compensate lack of PID ability of CDC(dE/dx measurement) and TOF(Time-of-flight) as shown in Figure 2.13.

Figure 2.14 shows configuration of ACC and Figure 2.15 shows a module of ACC. ACC has 960 modules for barrel region and 228 modules for forward endcap region. Due to KEKB asymmetric beams, final state particles which have high momentum are emitted with large polar angle and one which have low momentum are emitted with small polar angle. So ACC take into account of this condition and is optimized by varying refraction indices depending on the position of each ACC module.

When a particle passes a medium by the velocity which is faster than light speed in the medium, a cone of Čerenkov radiation is emitted. The half angle, θ_c , of it is given by

$$\cos \theta_c = \frac{1}{n\beta} = \frac{1}{n} \sqrt{1 + \left(\frac{m}{p}\right)^2}$$

where $\beta = v/c$ (v is velocity of a particle), n is refraction index, m is mass of a particle and p is momentum of a particle. In ACC fine-mesh photo-multiplier-tube(FM-PMT) is

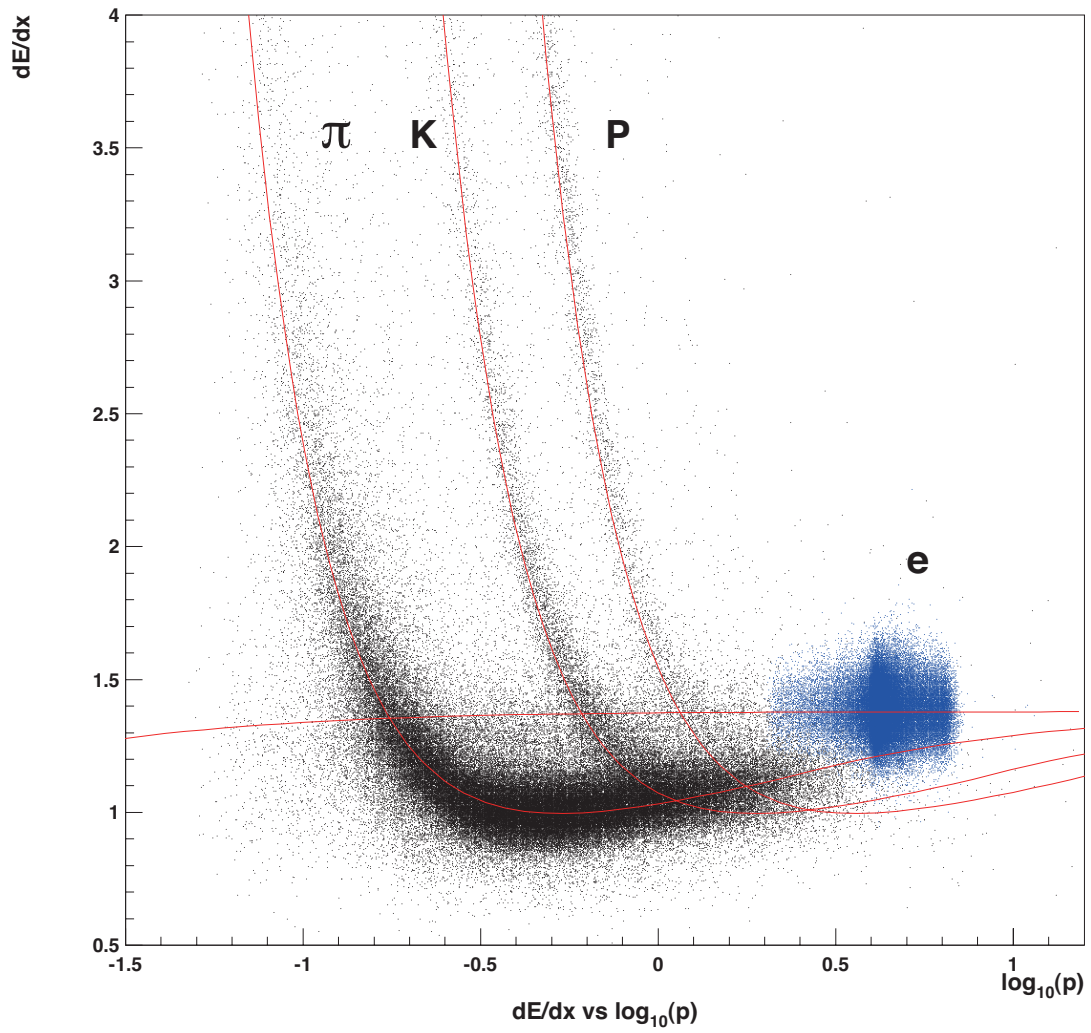


Figure 2.11: CDC dE/dx measurement

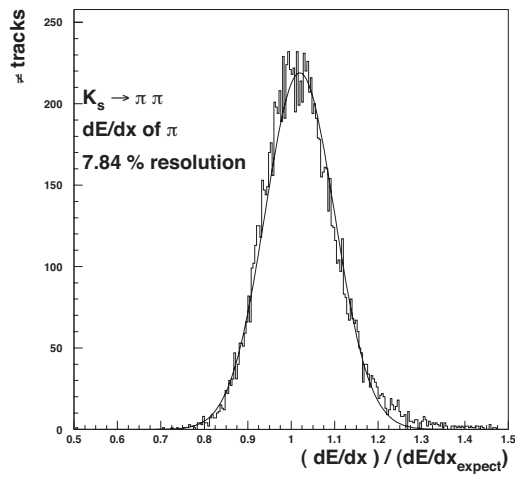


Figure 2.12: CDC dE/dx resolution

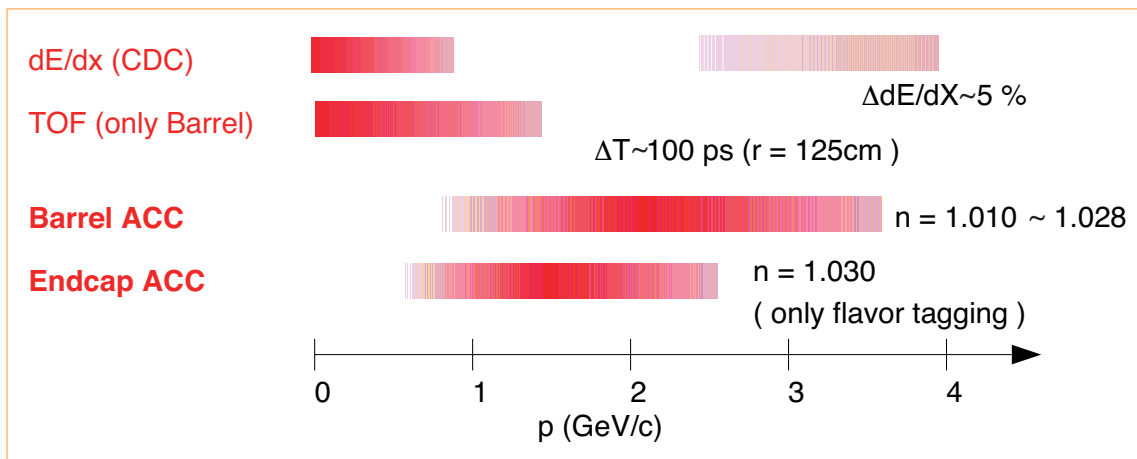


Figure 2.13: PID coverage momentum region of each sub-detectors

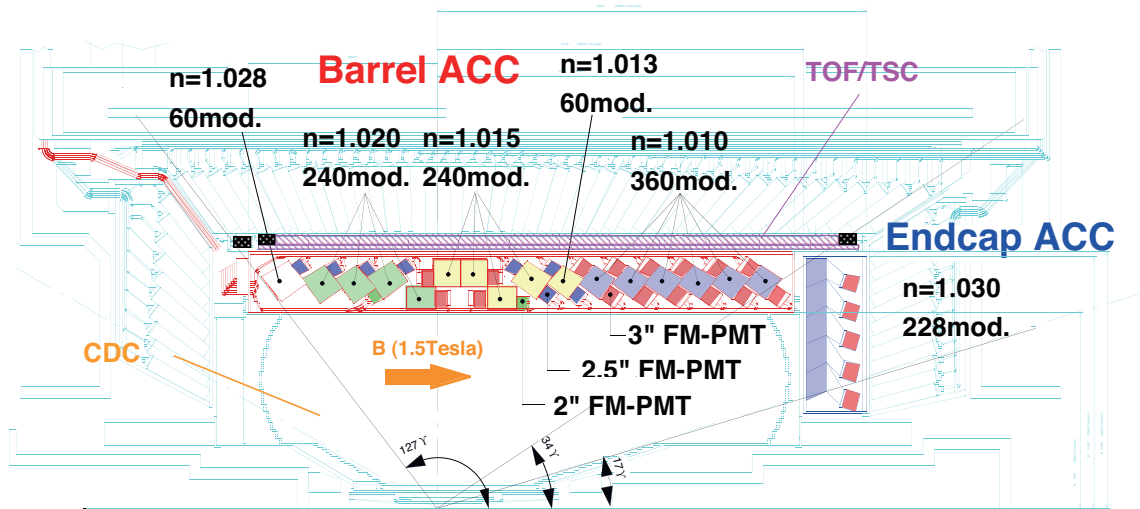
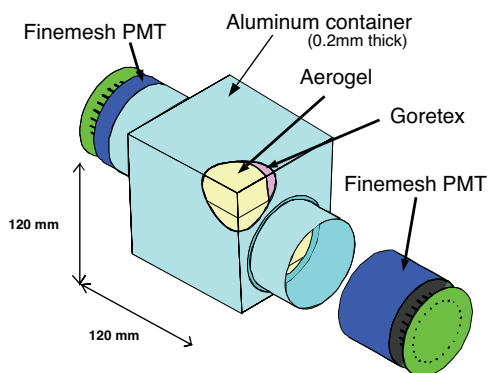


Figure 2.14: ACC configuration

a) Barrel ACC Module



b) Endcap ACC Module

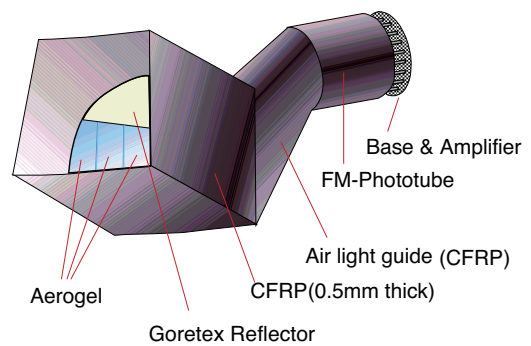


Figure 2.15: ACC module

employed for the operation in magnetic field, since usual photo multiplier doesn't work in magnetic field. It's schematic view is shown in Figure 2.16. And its performance is certainly confirmed in magnetic field as shown in Figure 2.17.

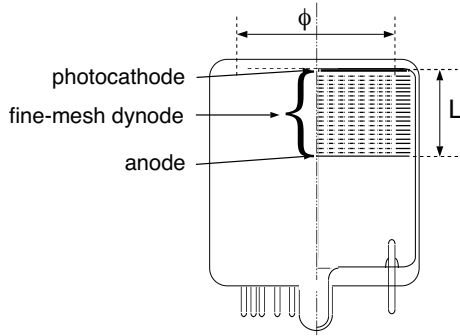


Figure 2.16: FM-PMT schematic view

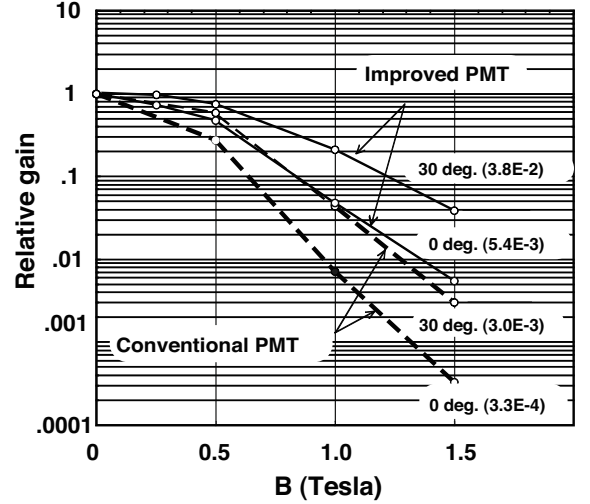


Figure 2.17: FM-PMT performance with magnetic field

Actually for particle separation, ACC uses light yield of FM-PMT as shown in Figure 2.18. For K/π separation, ACC works well in over 1 GeV/c momentum region as shown in Figure 2.19 and provide low miss identification probability as shown in Figure 2.20.

2.5 Time Of Flight / TOF

TOF provides us with K/π separation information in the low momentum region below about 1.2 GeV/c.

Figure 2.21 shows TOF and TSC module. Belle TOF subdetector consists TOF module and Trigger Scintillation Counter(TSC). TOF is located at the position of 120 cm in radius from IP. TOF has 128 TOF modules and 64 TSC modules which are segmented in the direction of ϕ . TSC is used for trigger timing signal of Belle.

By TOF, mass of a particle is determined as

$$m^2 = \left(\frac{1}{\beta^2} - 1\right)p^2 = \left(\left(\frac{cT_{TOF}}{L_{path}}\right)^2 - 1\right)p^2$$

where T_{TOF} is a measurements of TOF and L_{path} and p^2 are determined by CDC. Figure 2.22 and Figure 2.23 show particle identification performance of TOF.

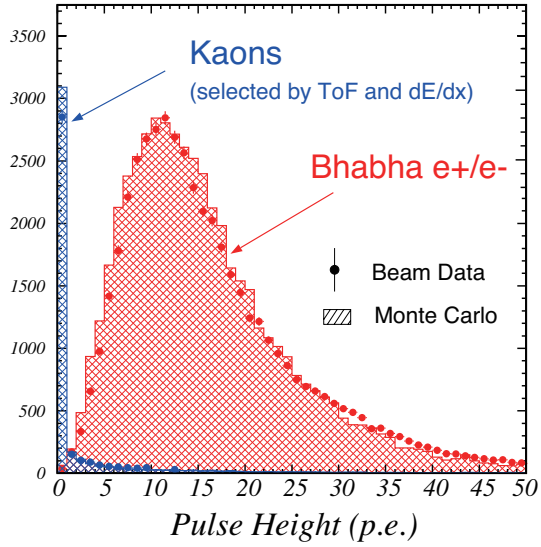


Figure 2.18: Light yield difference between K and e

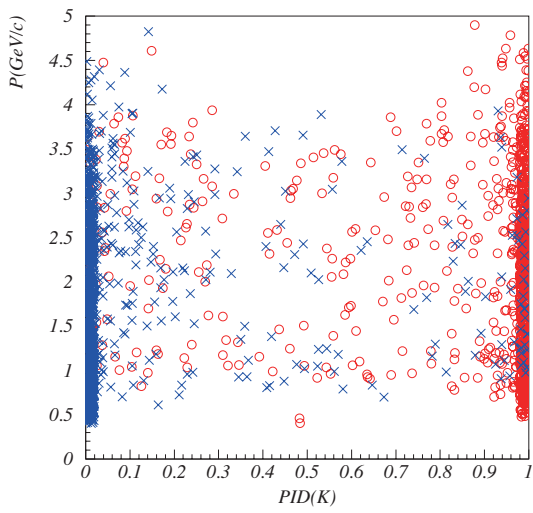


Figure 2.19: ACC PID performance for K/π separation. Red points show K tracks and blue points show π tracks.

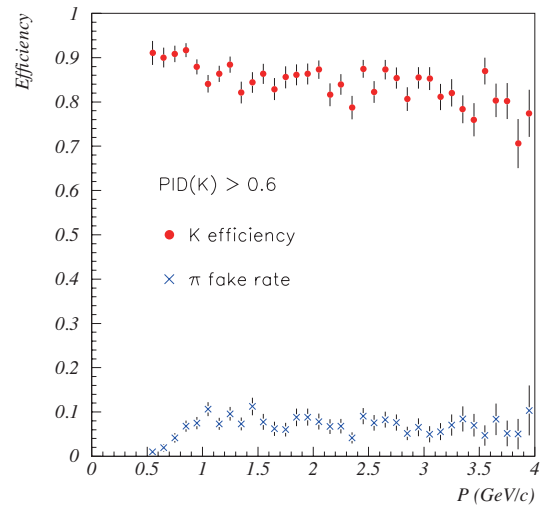


Figure 2.20: K efficiency and π miss identification probability of ACC

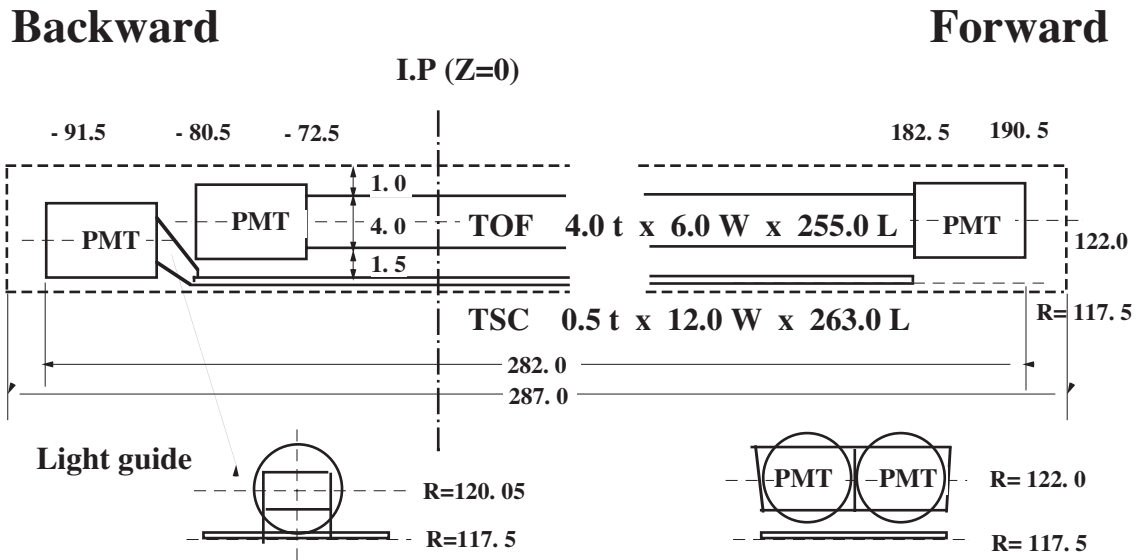


Figure 2.21: TOF and TSC

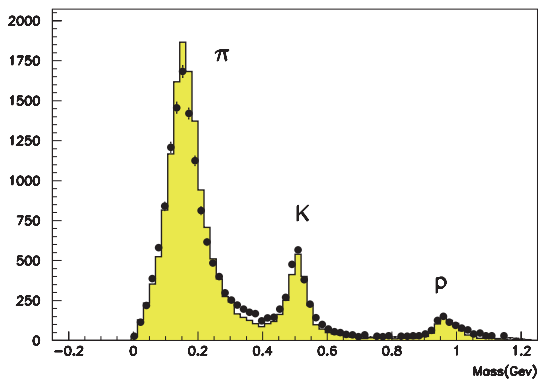


Figure 2.22: TOF PID performance

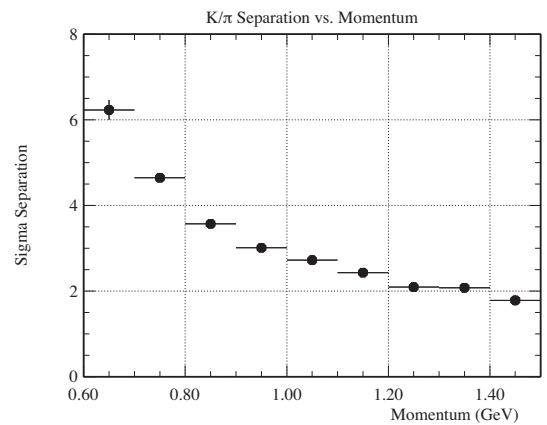


Figure 2.23: K/π separation of TOF PID

2.6 Electromagnetic Calorimeter / ECL

ECL is mainly designed to detect photons and to identify electrons.

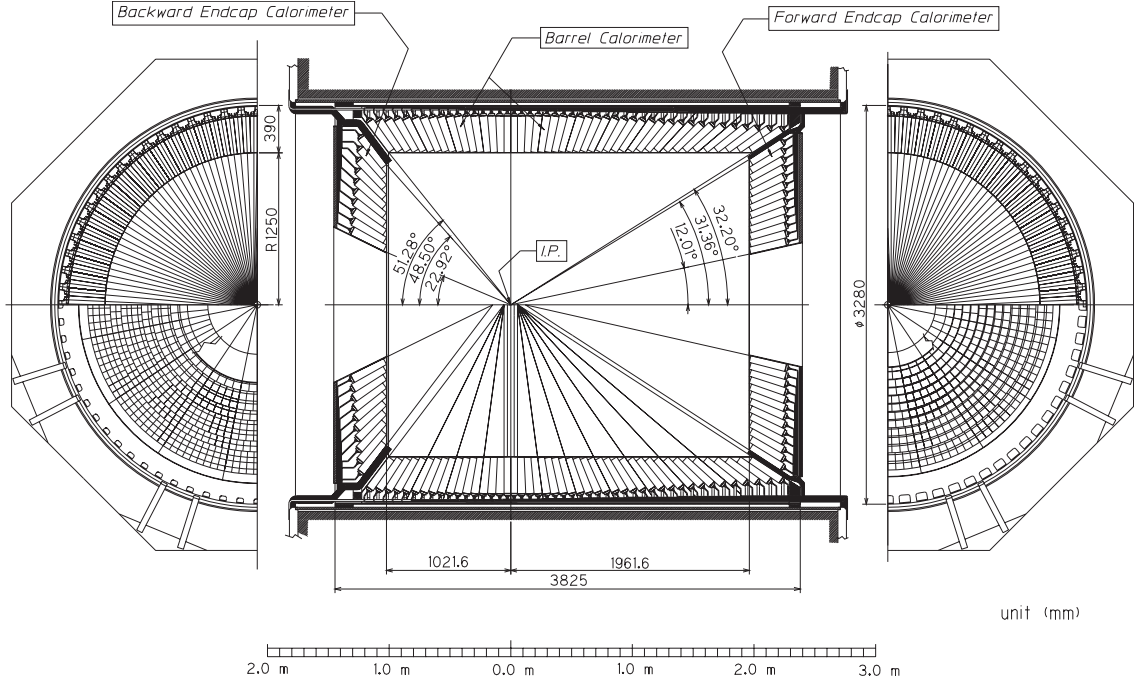


Figure 2.24: ECL configuration

Figure 2.24 shows a configuration of ECL. Figure 2.25 shows a module of ECL. ECL is located inside of Solenoid Magnet to improve position and energy resolution of photons. ECL has 8,736 $CsI(Tl)$ crystals in total and covers polar angle region $17^\circ < \theta < 150^\circ$. In Belle we use CsI crystal which is doped with thallium to increase light yields.

Electrons and photons are detected using electromagnetic shower. When a particle passes the crystal, it makes a cascade of pair-production and brehmstrahlung. And then finally visible photons are created and they are read-out by photodiodes. In the case of electron and photon, its energy typically loses almost of their energy. The total light yields are proportional to their energy. To prevent the shower leakage ECL crystal has 30 cm length which corresponds to radiation length (X_0) of 16.1. The ECL energy measurements are calibrated crystal by crystal using a large sample of Bhabha events. Energies of Bhabha event are well known and given by a function of scatter angle. Actually its resolution is

$$\sigma_E/E = (0.066/E \oplus 0.81/E^{1/4} \oplus 1.34)\%$$

and position resolution is

$$\sigma_x = (3.4/E \oplus 1.8/E^{1/4} \oplus 0.27)\text{mm}$$

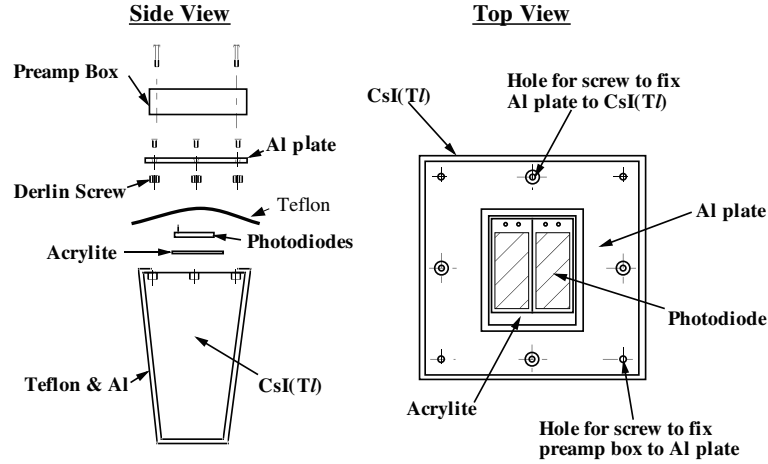


Figure 2.25: ECL module

where the unit of energy, E , is GeV.

2.7 Solenoid Magnet

To measure momentums of particle using curvature of particle's trajectory, Solenoid Magnet provides Belle with 1.5 T magnetic field in the direction of z -axis, beam.

Belle Solenoid Magnet is made of supre-conducting niobium-titanium-copper. And its cooling is provided by liquid helium circulating.

Using a curvature, we determine a momentum of charged particle as

$$p_T = qBr$$

and if we use SI units, it's able to change to useful formula as

$$p_T = 0.3qBr$$

where $p_T[\text{GeV}/c]$ is transverse momentum, $q[\text{C}]$ is charges of particle, $B[\text{T}]$ is magnetic field and $r[\text{m}]$ is curvature.

2.8 K_L/μ Detector / KLM

KLM is designed to identify μ and detect K_L . In addition to these purpose KLM also works as a return-yoke of Solenoid Magnet.

Figure 2.28 shows a configuration of KLM. Figure 2.29 shows a construction of super-layer RPC(Resistive Plate Chamber). KLM has 14 or 15 layers for Barrel and Endcap

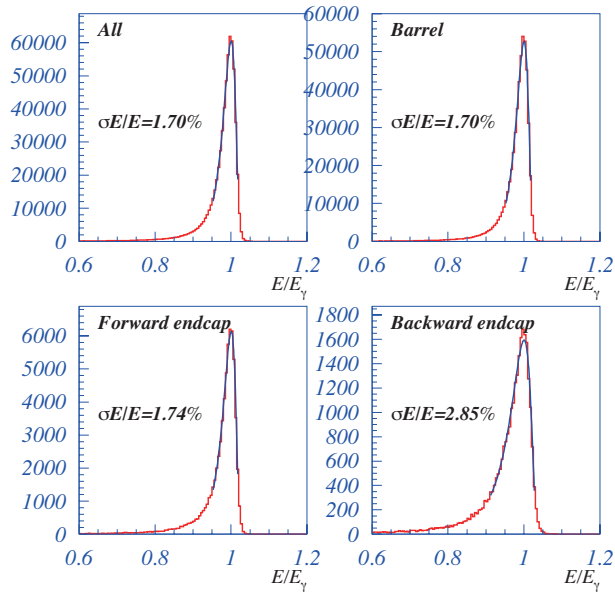


Figure 2.26: ECL energy resolution

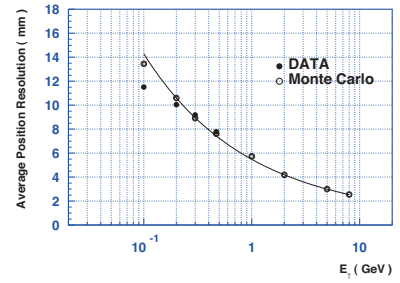


Figure 2.27: ECL spatial resolution

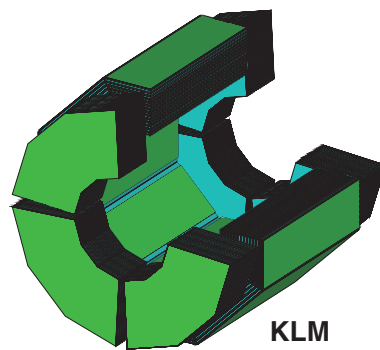


Figure 2.28: KLM configuration

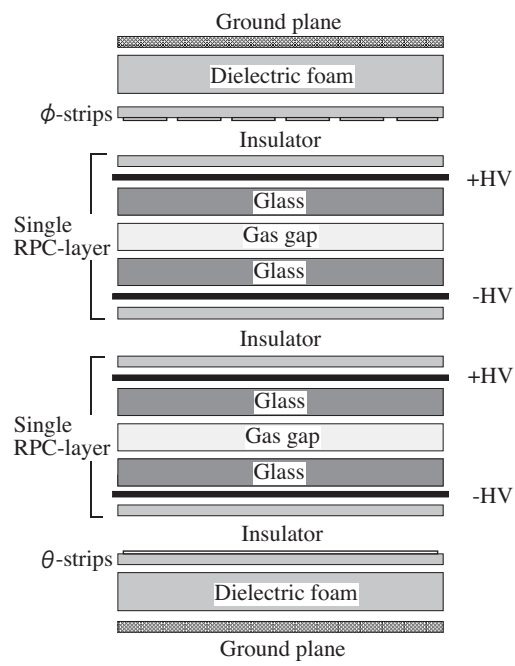


Figure 2.29: Structure of super-layer

part, respectively. In each region different shape RPC layers are used as shown in Figure 2.30 and Figure 2.31. Each layer consists super-layer RPC and 4.7 cm iron plate. KLM covers polar angle region of $20^\circ < \theta < 150^\circ$.

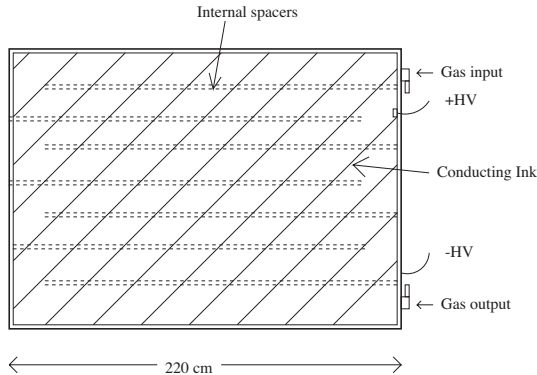


Figure 2.30: Barrel RPC

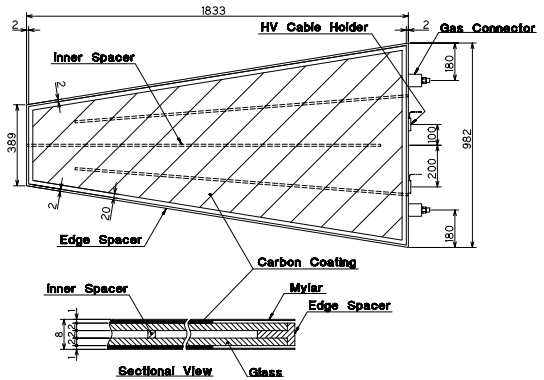


Figure 2.31: Endcap RPC

Because a difference of mass between μ (106MeV) and π (140MeV) is too close to distinguish by other sub-detectors we need a special μ detector. There for μ identification is important. Because the gold-plated mode of $\sin 2\phi_1$ measurements is $B^0 \rightarrow J/\psi(\rightarrow \mu^+ \mu^-) K_s$.

In KLM we mainly distinguish μ from π using number of penetrated KLM layers. Therefore because K_L is neutral hadrons detections of it is difficult. However K_L sometimes plays important role in B physics (e.g. $B^0 \rightarrow J/\psi K_L$). This mode is used for extraction of $\sin 2\phi_1$. So we detect K_L using hadron shower.

2.9 Trigger and DAQ

The Belle trigger system has 3 layers, hardware trigger(Level 1), on-line software trigger(Level 3) and off-line software trigger(Level 4).

The central trigger system of hardware trigger is called as Global Decision Logic(GDL). GDL combines trigger signals from sub-detectors as Figure 2.32. In this stage events are selected mainly based on track and energy deposit information. GDL roughly categorizes events and makes a decision to take data within 2.2 μ sec from a beam crossing. GDL has some flexibility to keep the trigger rate within tolerance of the DAQ system. For example basically we do not have special reason to take Bhabha events for physic analysis. But we need a few events for a luminosity measurement and ECL calibration. So we set the trigger condition to take these events sometimes, not always. However its rate is suppressed not to disturb data taking of physical interesting events. If GDL decide to take a event it provide

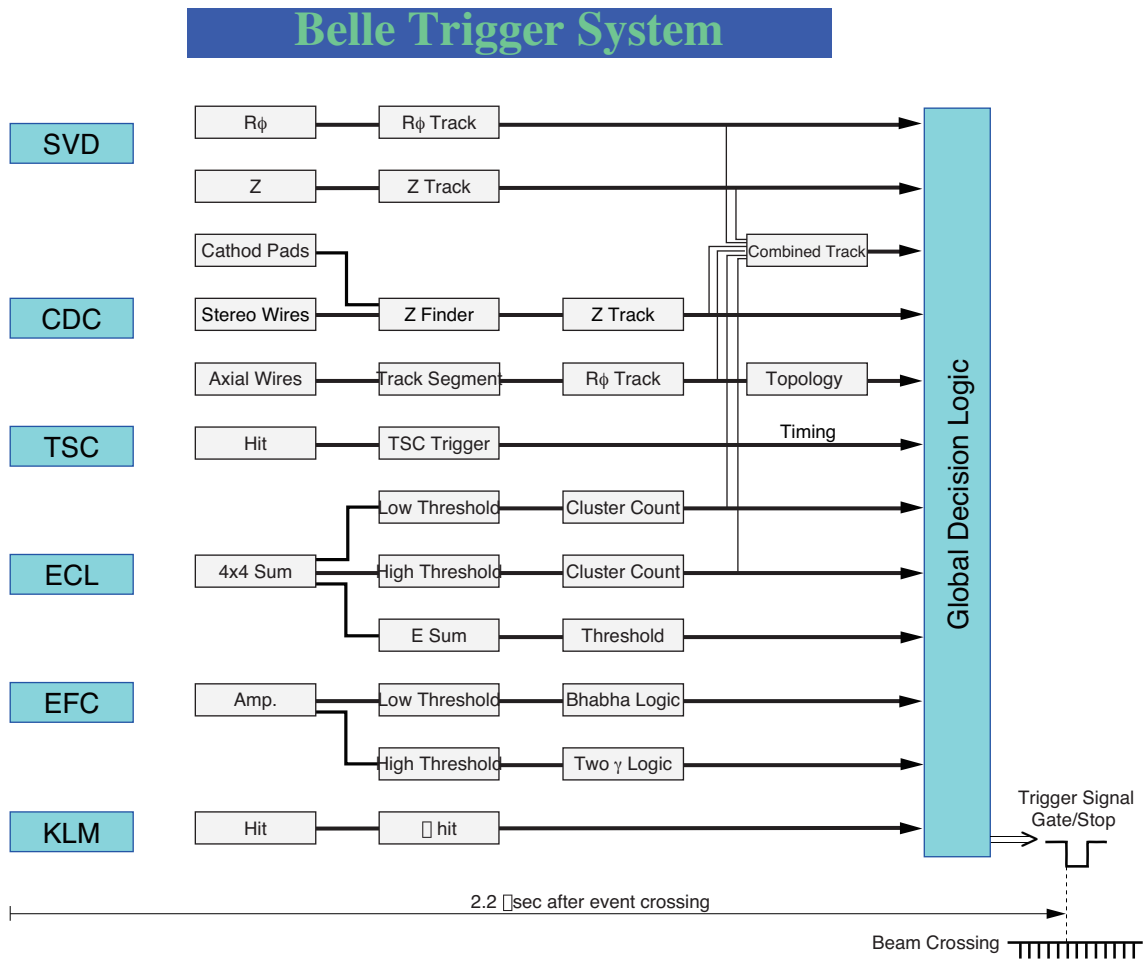


Figure 2.32: Trigger scheme

sub-detectors with common stop signals of TDCs and gate signals of ADC. Then readout data is transferred to the event builder.

Shipped data from the event builder is selected by on-line software trigger. On-line software trigger consists ultra fast tracking finder which select about 60% events based on the z vertex position. Then the selected events are sent to Offline Computing Farm.

The recored events are processed using more precise filter, off-line software trigger. The events passing off-line software trigger are send to the Data Storage Tape(DST) production chain. In this stage tables of tracking, gamma energy, PID information and etc, are made for physic analysis.

2.10 Monte Carlo

Belle corroboration use EvtGen to make Monte Carlo events based on the decay table which is updated Belle corroboration frequently. That generated events are processed using a detector full-simulator based on GEANT3.

Using it "generic" Monte Carlo and "rare" Monte Carlo is generated. It's difference is including decay modes and factor of data size. "generic" Monte Carlo includes decay mode up to $\mathcal{O}(10^{-5})$ and has 3 times larger data set which corresponds to the real experiment data. On the other hand "rare" Monte Carlo includes decay mode up to $\mathcal{O}(10^{-7})$ and has 25 larger times data set to carefully check the effect of rare decay. Therefore we can also make signal Monte Carlo we want. Signal Monte Carlo is usually used for an estimation of signal efficiency.

Chapter 3

$B^- \rightarrow DK^-$ analysis

In this chapter the procedure of $B^- \rightarrow DK^-$ reconstruction which consists event selection criteria, backgrounds, and signal extraction, is described.

Although our interest is the suppressed decay, $B^- \rightarrow D_{sup}[K^+\pi^-]K^-$, the favored decay, $B^- \rightarrow D_{fav}[K^-\pi^+]K^-$ whose statistics is enough to suppress systematic uncertainties, is also analyzed. Because the difference between suppressed and favored mode is only charge of D daughters and their kinematics are same, by taking the ratio of these yields, most of systematic uncertainties such as detection efficiency, PID cut, event shape LR cut and etc. are cancelled.

In addition to $B^- \rightarrow DK^-$ mode $B^- \rightarrow D\pi^-$ is also analyzed for cross check.

3.1 Data set

In this analysis, as shown in Figure 3.1 366 fb⁻¹ of data set (experiment number 7 ~ 41) which corresponds to 386 million $B\bar{B}$ pairs recorded at the $\Upsilon(4S)$ resonance with Belle is used.

3.2 Event selection criteria

Firstly a list of event selection criteria is shown. Then the detail description of that is shown below the list. The same style is used for each selection criteria in this thesis.

3.2.1 Primary charged tracks

- $|dr| < 5$ mm, $|dz| < 5$ cm

To suppress beam backgrounds, charged tracks are required to have a point of closest approach to the beam line within ± 5 mm of IP in the direction perpendicular to beam axis, dr , and ± 5 cm in the direction parallel to the beam axis, dz .

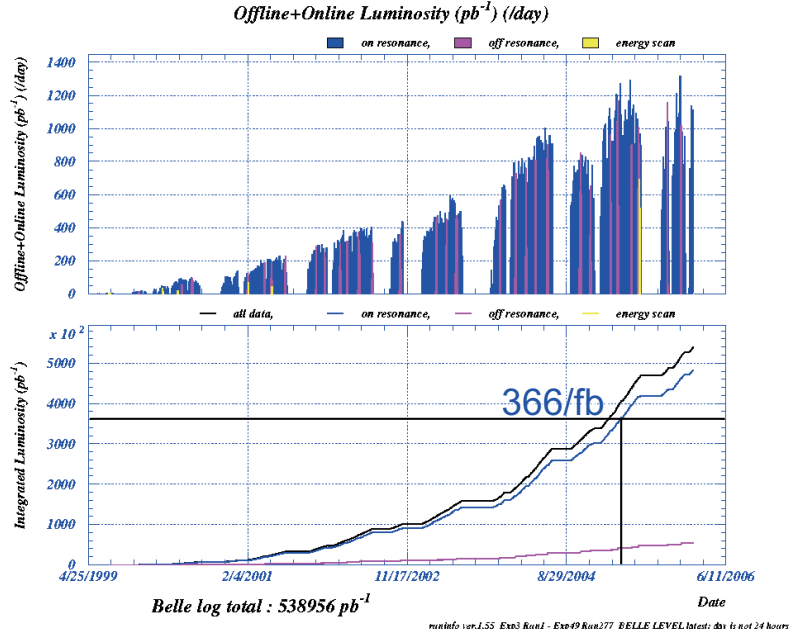


Figure 3.1: Belle luminosity

3.2.2 D reconstruction

- K tracks : $LR(K/\pi) > 0.4$
- π tracks : $LR(K/\pi) < 0.7$
- $1.850 < M(K\pi) < 1.879[\text{GeV}/c^2](2.5\sigma)$

D mesons are reconstructed by combining two oppositely charged tracks.

To distinguish K tracks from π tracks, we use likelihood ratio between K and π which is constructed using Kaon(pion) likelihoods, $\mathcal{L}_K(\mathcal{L}_\pi)$, based on dE/dX measurements, Čerenkov counter(ACC) information and Time-of-Flight(TOF) and calculated as

$$LR(K/\pi) = \mathcal{L}_K/\mathcal{L}_\pi \quad (3.1)$$

$$\mathcal{L}_{K,\pi} = \mathcal{L}_{K,\pi}^{dE/dx} \times \mathcal{L}_{K,\pi}^{ACC} \times \mathcal{L}_{K,\pi}^{TOF}. \quad (3.2)$$

In this case we require $LR(K/\pi) = \mathcal{L}_K/\mathcal{L}_\pi > 0.4$ for K and $LR(K/\pi) < 0.7$ for π . In this momentum region K and π efficiencies are 0.987 and 0.986, and their fake rate(the probability that $\pi(K)$ tracks are identified as $K(\pi)$) are 0.051 and 0.079, respectively.

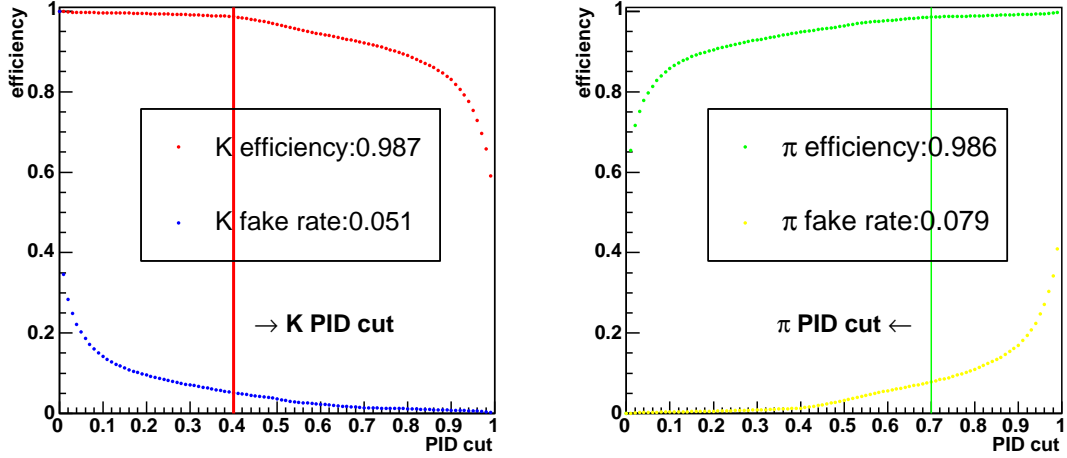


Figure 3.2: PID performance of D daughters, K (left) and π (right). This shows the efficiency and fake rate as a function of PID cut value. This data set is taken from Monte Carlo.

D candidates are required to have an invariant mass within $\pm 2.5\sigma$ of the nominal D mass, $1.850 < M(K\pi) < 1.879[\text{GeV}/c^2]$. And to suppress contaminations from favored decay if K and π mass assignments are exchanged and its mass is within D mass signal region, the event is vetoed.

To improve the momentum determination of B mesons, tracks of D candidates are refitted by constraining the invariant mass to the nominal D mass and the track origin to the reconstructed vertex position (mass-vertex fit).

3.2.3 B^- reconstruction

- prompt K tracks : $LR(K/\pi) > 0.6$
- prompt π tracks : $LR(K/\pi) < 0.2$
- $5.27 < M_{bc} < 5.29[\text{GeV}/c^2]$
- $|\Delta E| < 0.05[\text{GeV}]$

B^- candidates are reconstructed by combining the D candidate which satisfies the condition and a prompt particle candidate. For prompt particles, PID LR cut is tighter than daughter tracks of D^0 candidates to suppress the contamination from $B \rightarrow D\pi^-$ mode for $B \rightarrow DK^-$ mode.

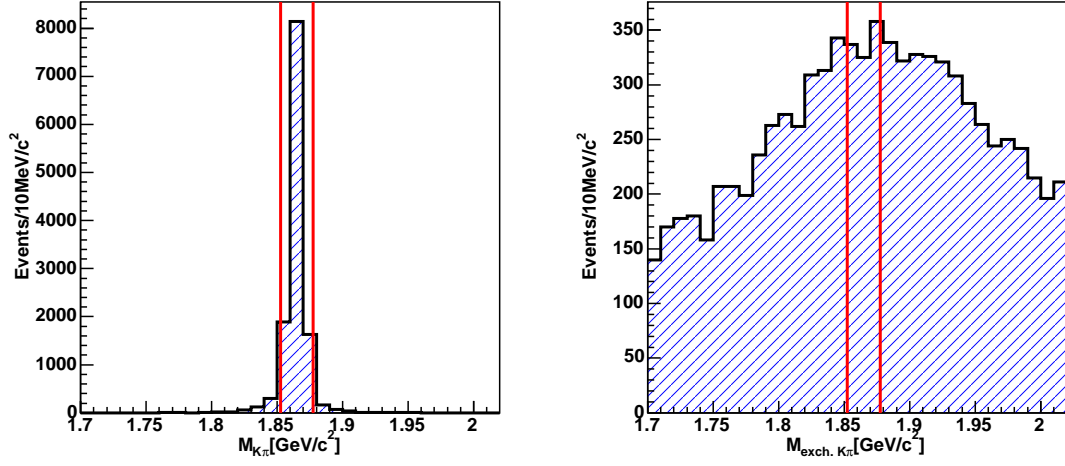


Figure 3.3: The mass distribution of $K\pi$ pair(left) and the exchanged mass distribution(right).This data set is taken from Monte Carlo.

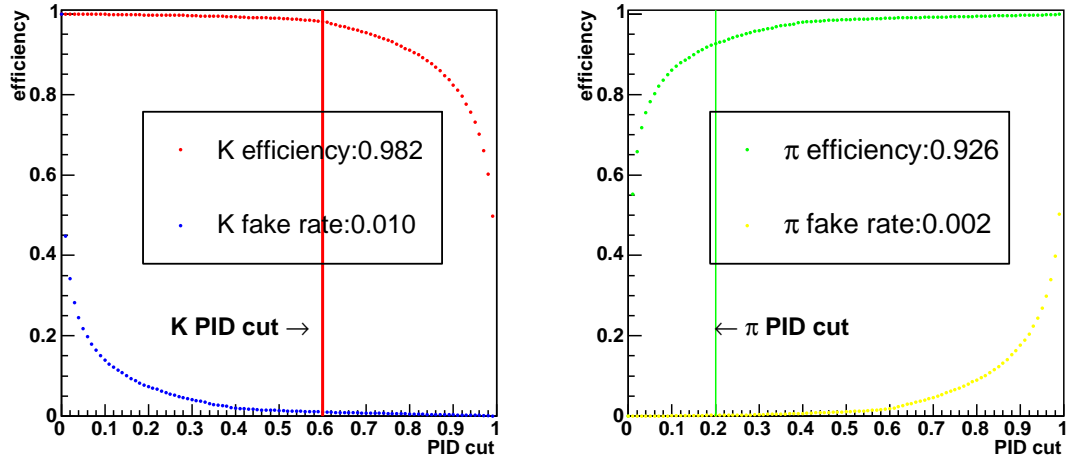


Figure 3.4: PID performance of prompt particles, K (left) and π (right).This data set is taken from Monte Carlo.

In addition to these cuts, to identify the signal we use two kinematic variables, the energy difference

$$\Delta E \equiv E_D + E_{K(\pi)} - E_{beam} \quad (3.3)$$

and the beam-energy-constrained mass

$$M_{bc} \equiv \sqrt{E_{beam}^2 - (\vec{p}_D + \vec{p}_{K(\pi)})^2}, \quad (3.4)$$

where E_D is the energy of the D candidates, $E_{K(\pi)}$ is the energy of the $K(\pi)$ and E_{beam} is the beam energy, all evaluated in the center of mass (CM) frame. \vec{p}_D and $\vec{p}_{K(\pi)}$ are the momentum of the D and $K(\pi)$ in the cm frame. Figure 3.6 and Figure 3.5 show typical distributions of ΔE and M_{bc} .

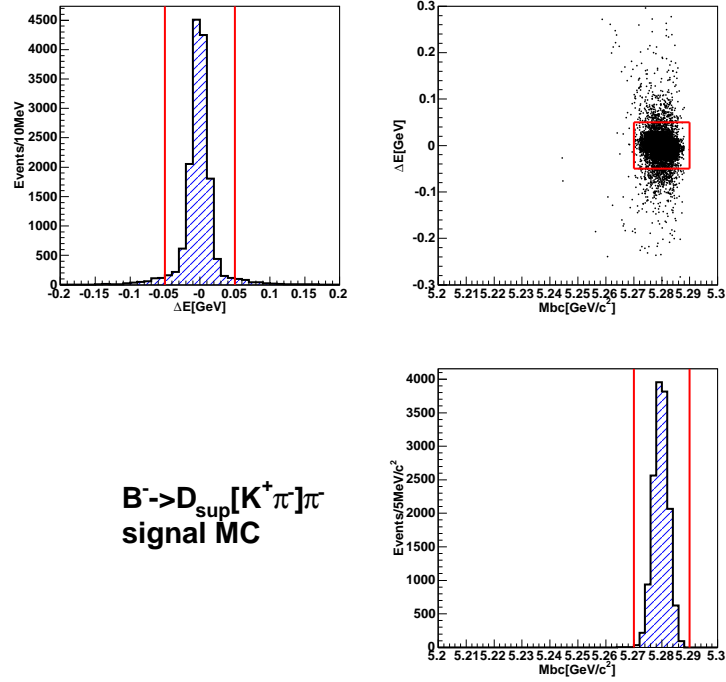


Figure 3.5: ΔE and M_{bc} distribution of $B^- \rightarrow D_{sup}\pi^-$ signal Monte Carlo events

If there are multiple-candidates in a event, we choose the best candidate on the basis of χ^2 determined from

$$\chi^2 = \left(\frac{m_{k\pi} - m_{D^0 nominal}}{\sigma_D}\right)^2 + \left(\frac{M_{bc} - 5.285}{\sigma_{M_{bc}}}\right)^2 \quad (3.5)$$

where σ represents experimental resolution.

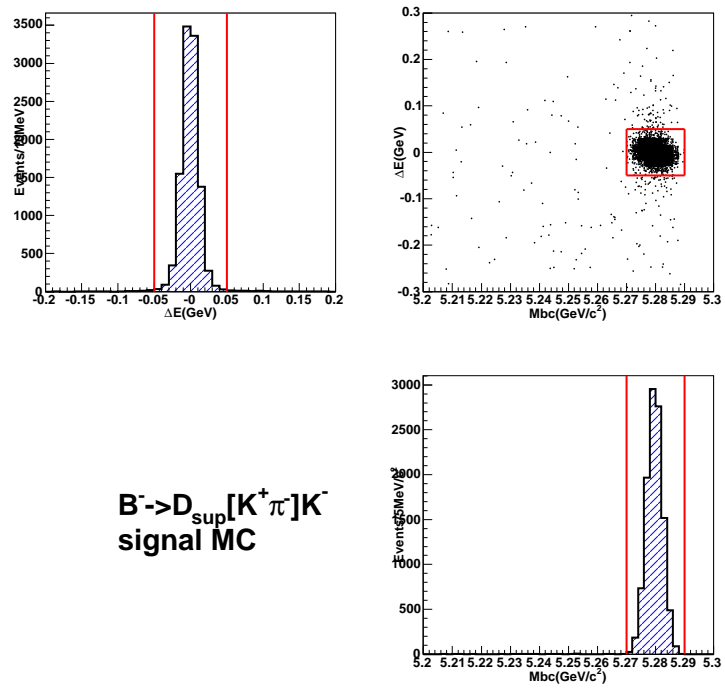


Figure 3.6: ΔE and M_{bc} distribution of $B^- \rightarrow D_{sup}K^-$ signal Monte carlo events

3.2.4 $q\bar{q}$ continuum backgrounds suppression

- DK mode: $LR_{(KSF\bar{W}, \cos\theta_B)} > 0.91$
- $D\pi$ mode: $LR_{(KSF\bar{W}, \cos\theta_B)} > 0.74$

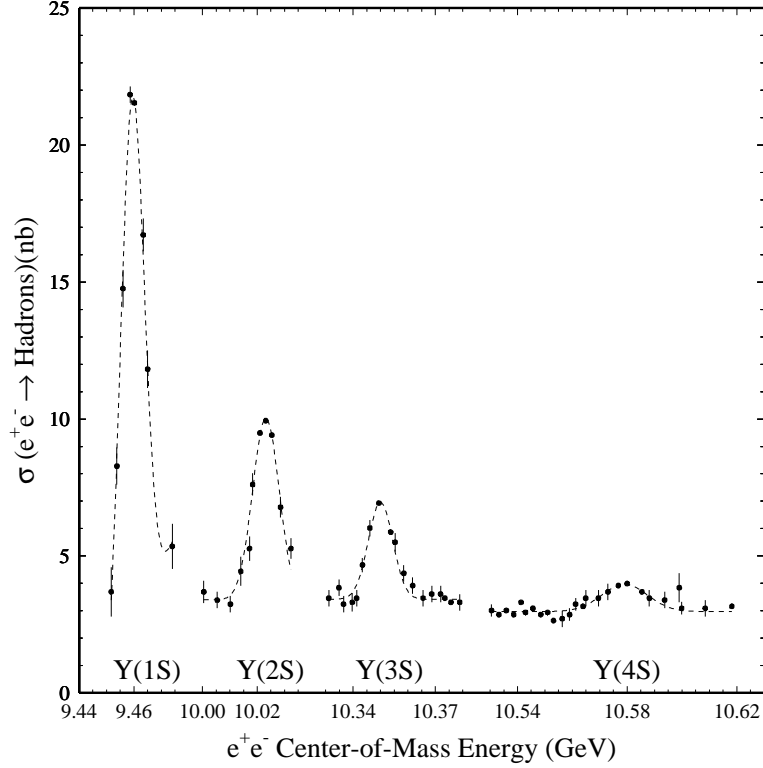


Figure 3.7: $e^+e^- \rightarrow \text{hadron}$ cross-section

As shown in Figure 3.7, around $\Upsilon(4S)$ resonance there are 3 times larger $q\bar{q}$ background than $B\bar{B}$ events. Actually as shown in Figure 3.8 and Figure 3.9 large $q\bar{q}$ backgrounds are seen with "uds" and "charm" Monte Carlo. The difference between $B\bar{B}$ events and $q\bar{q}$ background is only event topology. The decay shape of $q\bar{q}$ event is spherical, and one of $B\bar{B}$ is jet-like. To suppress this large background from two-jet like $e^+e^- \rightarrow q\bar{q}$ ($q = u, d, s, c$) continuum processes, variables that characterize the event topology are used.

There are some methods to characterize it, thrust angle (Figure 3.10 left), super Fox Wolfram method (so-called SFW, Figure 3.10 right) and improved SFW technique (so-called KSF\bar{W}, Figure 3.11). In detail, refer to Appendix A. So we compare these methods as shown in Figure 3.12. By this result to suppress background and retain efficiency simultaneously KSF\bar{W} method looks most preferable than other methods. So in this thesis KSF\bar{W} method is used for event shape characterization.

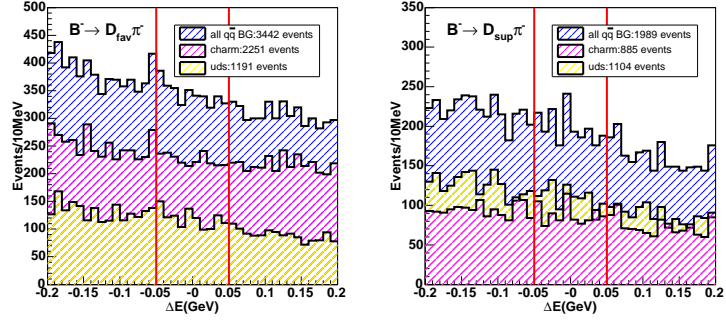


Figure 3.8: $q\bar{q}$ background for $B^- \rightarrow D\pi^-$ decay mode with "uds" and "charm" Monte Carlo. The numbers of events within ΔE signal region (inside of red lines) are shown.

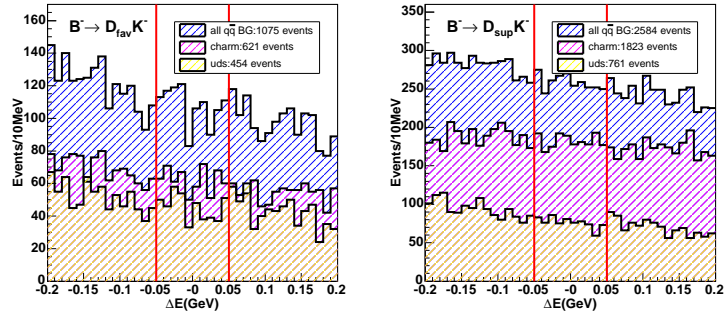


Figure 3.9: $q\bar{q}$ background for $B^- \rightarrow DK^-$ decay mode with "uds" and "charm" Monte Carlo. The numbers of events within ΔE signal region (inside of red lines) are shown.

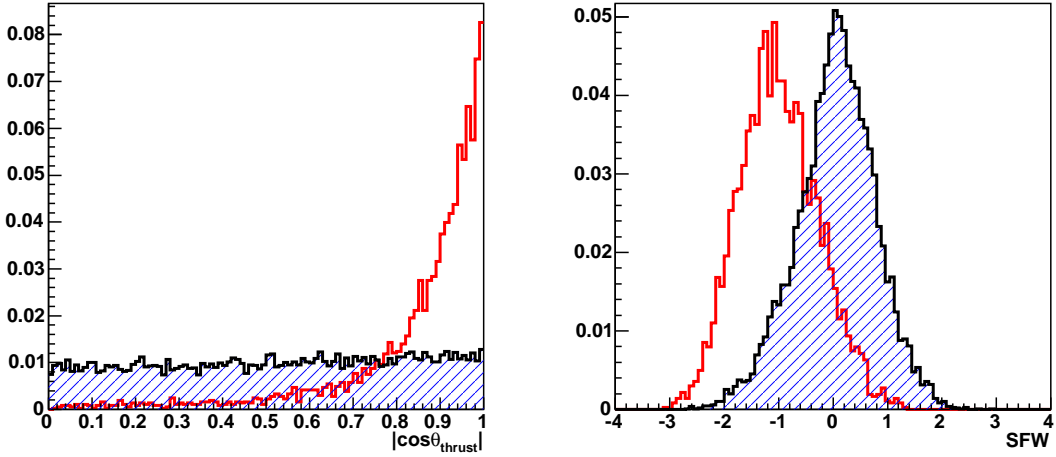


Figure 3.10: The $\cos\theta_{thrust}$ distribution(left) and SFW value distribution(right).In these plot blue hatched histogram is signal Monte Carlo and red histogram is M_{bc} sideband data.

Furthermore, $\cos\theta_B$, the angle in the CM system of the B flight direction with respect to the beam axis, is also used to distinguish $B\bar{B}$ events from continuum events. The angular distribution of $B\bar{B}$ pair is proportional to $\sin^2\theta_B$ because the spin and parity of $\Upsilon(4S)$ are $J^P = 1^-$, while one of continuum background is essentially uniform as shown in Figure3.13.

These two independent variables, KSFW and $\cos\theta_B$, are combined to form a likelihood ratio

$$LR_{(KSFW, \cos\theta_B)} = \mathcal{L}_{sig}/(\mathcal{L}_{sig} + \mathcal{L}_{cont}) \quad (3.6)$$

$$\mathcal{L}_{sig(cont)} = \mathcal{L}_{sig(cont)}^{KSFW} \times \mathcal{L}_{sig(cont)}^{\cos\theta_B}, \quad (3.7)$$

where \mathcal{L}_{sig} and \mathcal{L}_{cont} are likelihoods defined from KSFW and $\cos\theta_B$ distributions for signal and continuum backgrounds, respectively.

We optimize the LR requirement by maximizing "figure of merit"(F.o.M) which is defined as

$$(F.o.M) \equiv \frac{S}{\sqrt{S+N}}, \quad (3.8)$$

where S and N denote the expected number of signal and background events in the signal region.

The expected number of signal events are calculated from $B^- \rightarrow D_{sup}K^-$ previous results by Belle [10]. The efficiency is obtained from signal Monte Carlo. For background

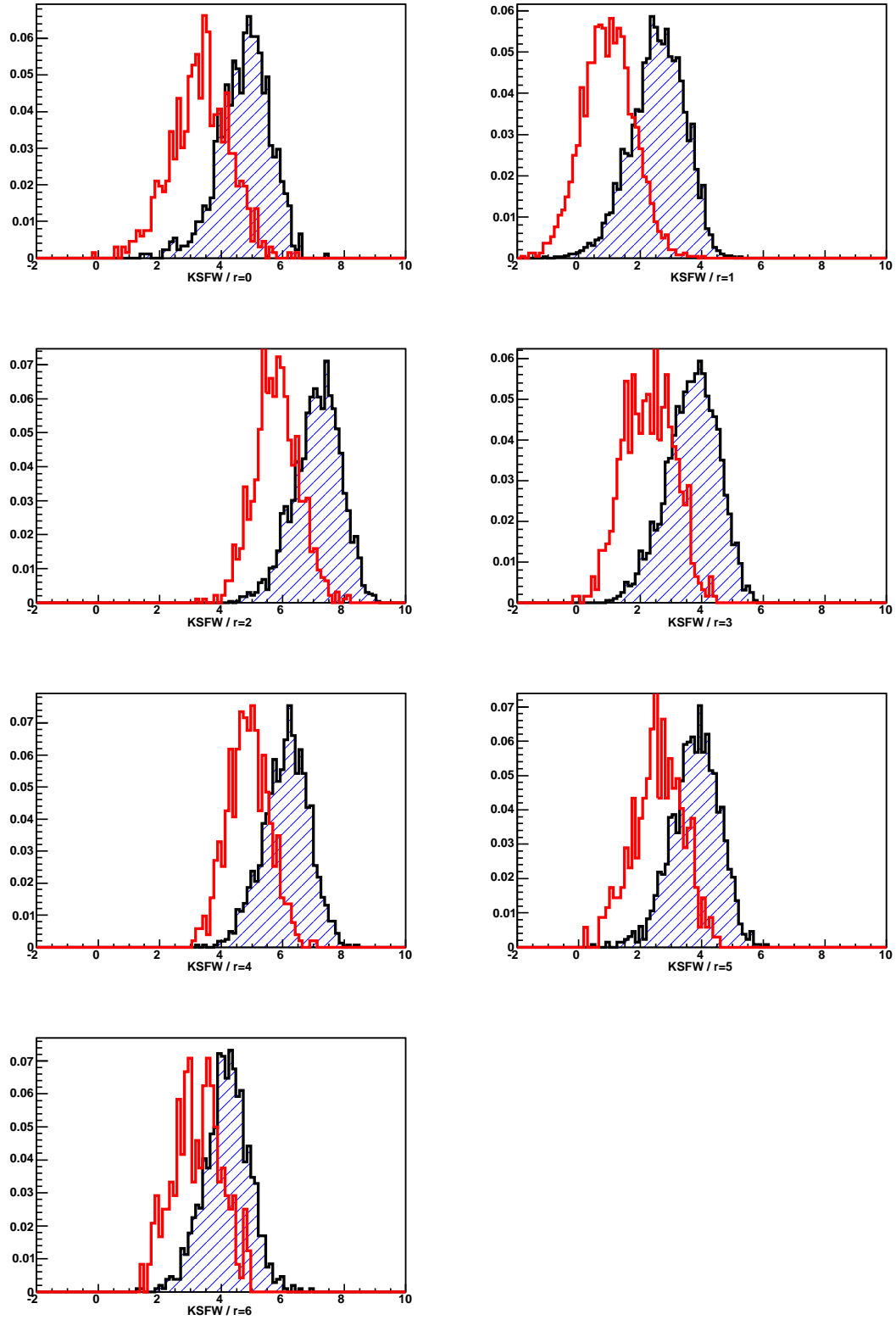


Figure 3.11: KSFW value distribution. These plot shows KSFW value distribution of each missing-mass-square bin. Blue hatched histogram is signal Monte Carlo and red histogram is M_{bc} sideband data.

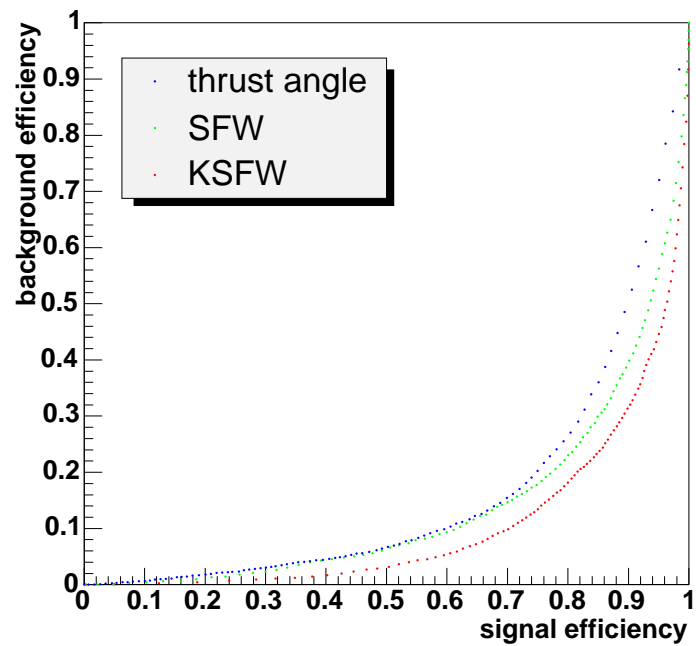


Figure 3.12: The comparison of continuum backgrounds suppression methods

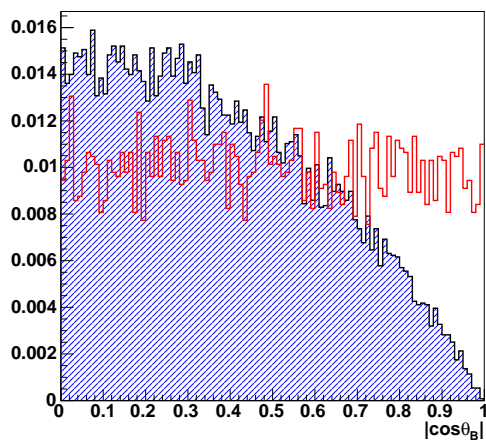


Figure 3.13: $\cos \theta_B$ distribution. θ_B is a B flight direction respect to beam axis. Hatched histogram is signal Monte Carlo and red histogram is M_{bc} sideband data.

Mode	#(signal)	#(background)	Expected \mathcal{B}	Efficiency(%)
$B^- \rightarrow D_{fav}\pi^-$	56154	2654	1.9×10^{-4}	38.3
$B^- \rightarrow D_{sup}\pi^-$	197	1507	6.6×10^{-7}	38.7
$B^- \rightarrow D_{fav}K^-$	3691	814	1.4×10^{-5}	34.2
$B^- \rightarrow D_{sup}K^-$	85.4	1955	3.2×10^{-7}	34.6

Table 3.1: Expected number of signal and background events with 366 fb^{-1} data set ($386 \times 10^6 B\bar{B}$ pairs). These efficiencies are ones before event shape variable cut. These numbers of background events are estimated from "uds" and "charm" Monte Carlo events whose size are 532 fb^{-1} corresponding to 3 times events of experimental number 21 to 37(177.4 fb^{-1}).

its number of events are estimated from "uds" and "charm" Monte Carlo. Background reduction rate depending LR cut point is obtained from M_{bc} sideband($5.2 < M_{bc} < 5.26$ [GeV/c^2] and $|\Delta E| < 0.2$ [GeV]) data because of low reliability for QCD dynamics in Monte Carlo. In M_{bc} sideband $q\bar{q}$ events are dominant comparing to $B\bar{B}$ events. So M_{bc} sideband data is a good sample of continuum background.

For $B^- \rightarrow D_{sup}K^-(\pi^-)$ we require $LR > 0.86(0.73)$, which retains 48.6% (66.9%) of the signal and removes 98.0% (91.4%) of the continuum background as Figure 3.14 and Figure 3.15. To cancel the systematics, same cut as the suppressed mode is applied to the favored mode.

3.2.5 Peaking backgrounds

- KK veto: $1.843 < M(KK) < 1.894[\text{GeV}/c^2]$ for $B^- \rightarrow D_{sup}K^-$ decay

To check the background source, "generic Monte Carlo" which consists decays up to $\mathcal{O}(10^{-5})$ and "rare Monte Carlo" which consists decays up to $\mathcal{O}(10^{-7})$ are used as Figure 3.16 and Figure 3.17.

For $B^- \rightarrow D_{sup}K^-$, one can have a contribution from $B^- \rightarrow D\pi^-$, $D \rightarrow K^+K^-$, which has the same final state and can make peak under the signal region of M_{bc} and ΔE . In order to reject these events, the event satisfying $1.843 < M(KK) < 1.894[\text{GeV}/c^2]$ is vetoed.

Furthermore, three-body charmless decays $B^- \rightarrow K^+K^-\pi^-$ and $B^- \rightarrow K^+\pi^-\pi^-$ can peak inside the signal region for $B^- \rightarrow D_{sup}K^-$ and $B^- \rightarrow D_{sup}\pi^-$, respectively. These peaking backgrounds can not be removed by veto. So their effects are estimated from the ΔE distributions of events in a D mass sideband, corresponding to $\pm(2.5 - 10)\sigma$ away from the nominal D mass ($1.807 < M(K\pi) < 1.850[\text{GeV}/c^2]$ and $1.879 < M(K\pi) < 1.937[\text{GeV}/c^2]$). We fit these distributions, which are shown in Figure 3.18, using a procedure similar to that used for signal event candidates(described later).

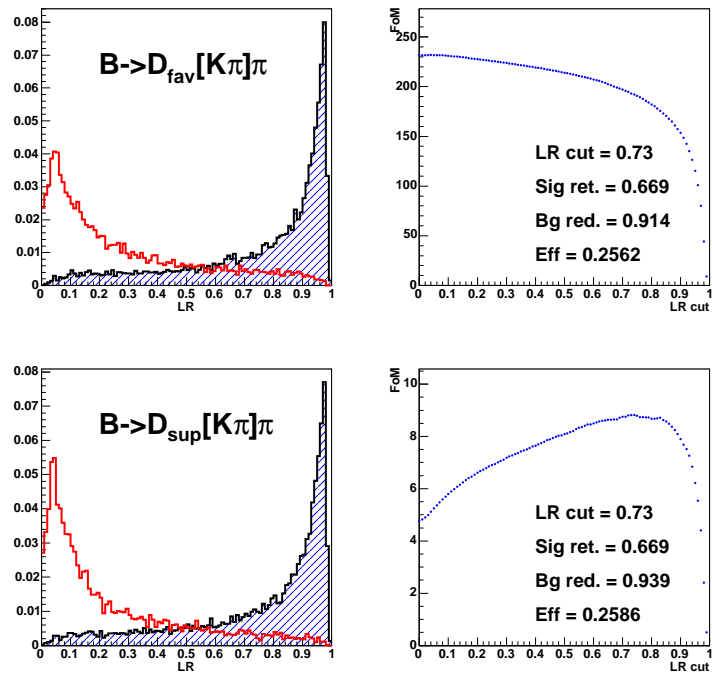


Figure 3.14: Event shape likelihood ratio distribution(left) and The "figure of merit" distribution(right) of $B^- \rightarrow D_{fav}^- \pi^-$ (top) and $B^- \rightarrow D_{sup}^- \pi^-$ (bottom)

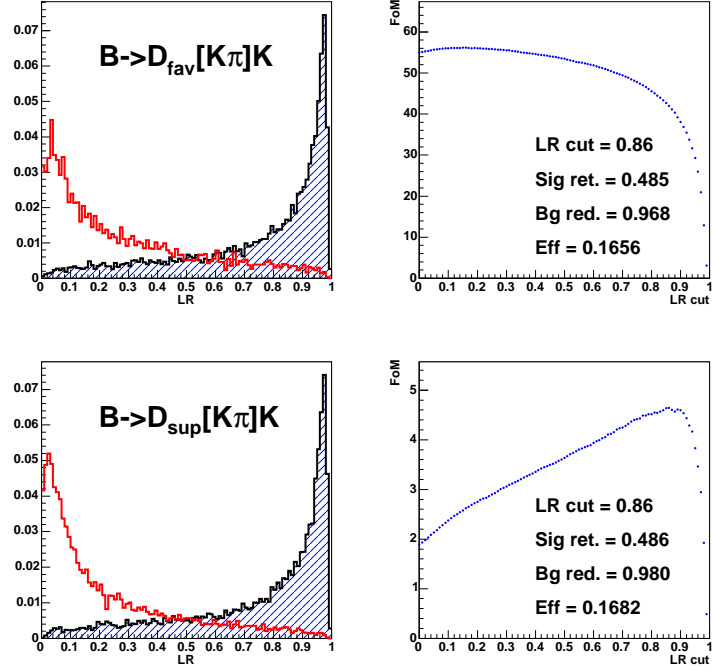


Figure 3.15: Event shape likelihood ratio distribution(left) and The "figure of merit" distribution(right) of $B^- \rightarrow D_{fav}^- K^-$ (top) and $B^- \rightarrow D_{sup}^- K^-$ (bottom)

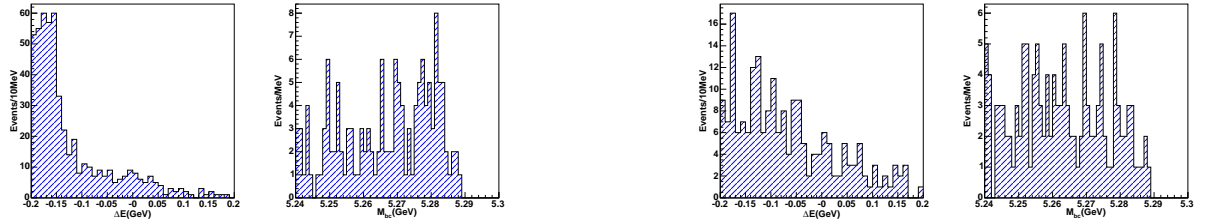


Figure 3.16: ΔE and M_{bc} distributions of generic Monte Carlo for $B^- \rightarrow D_{sup}^- \pi^-$ (left) and $B^- \rightarrow D_{sup}^- K^-$ (right)

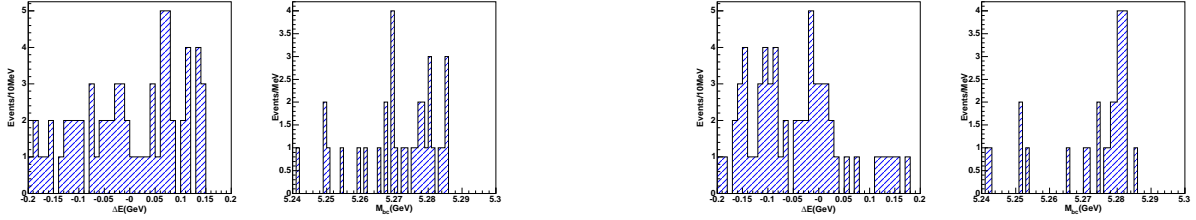


Figure 3.17: ΔE and M_{bc} distributions of rare Monte Carlo for $B^- \rightarrow D_{sup}\pi^-$ (left) and $B^- \rightarrow D_{sup}K^-$ (right)

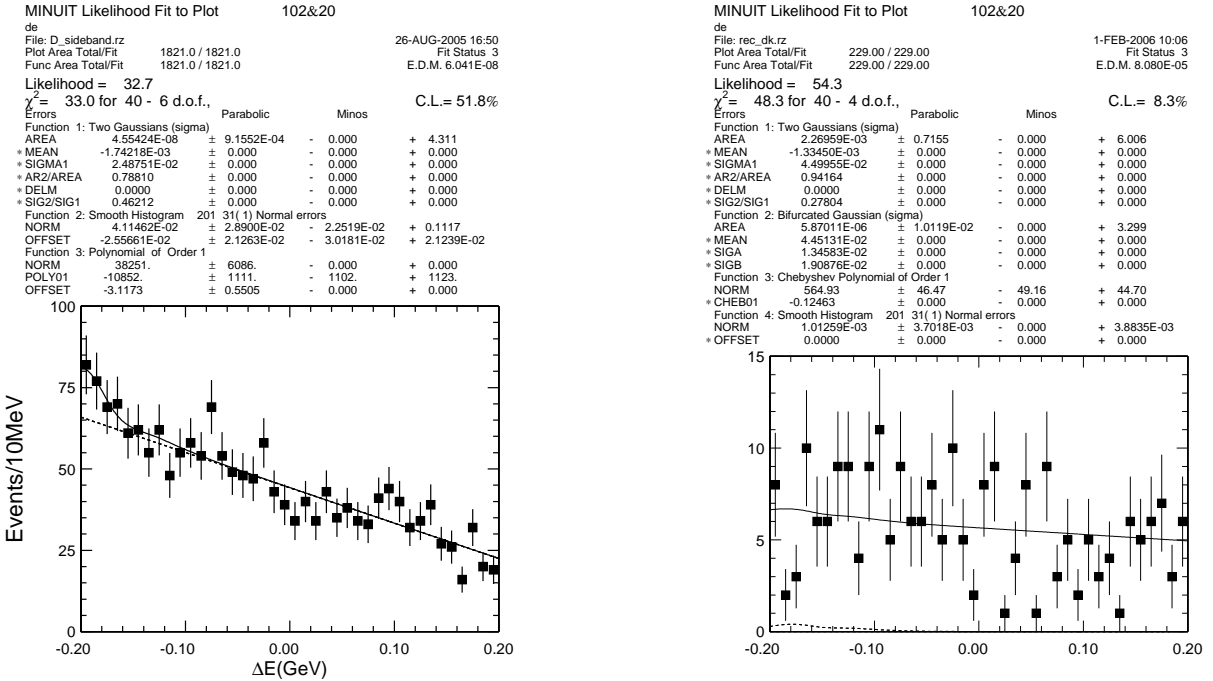


Figure 3.18: ΔE distribution of D mass sideband for $B^- \rightarrow D_{sup}\pi^-$ (left) and $B^- \rightarrow D_{sup}K^-$ (right) mode

For $B^- \rightarrow D_{sup}\pi^-$, the peaking background estimated by fitting the plot is consistent with zero. Since the Standard Model prediction for the $B^- \rightarrow D_{sup}\pi^-$ branching fraction is smaller than 10^{-11} [11], this background contribution is ignored.

For $B^- \rightarrow D_{sup}K^-$, its yield is also consistent with zero.

3.3 Results

3.3.1 Fitting the ΔE distributions

Component	Function	Parameter	Fit	$D\pi$	DK
Signal	Double-Gaussian	area	float		
		mean	float→fix		
		σ_1	float→fix	○	○
		area ₂ /area ₁	fix		
		σ_2/σ_1	fix		
$q\bar{q}$	Linear function	area	float	○	○
		slope	fix		
$B\bar{B}$	Smoothed-histogram	area	float	○	○
feed-across	Bifurcated-Gaussian	area	float		
		mean	fix	×	○
		σ_1	fix		
		σ_2	fix		

Table 3.2: fitting component for $B^- \rightarrow D\pi^-/K^-$

To extract signal yield, ΔE -fit is done assuming some fitting components as shown in Table 3.2. Regarding signal although its shape is naturally Breit-Wigner function, it is convoluted by experimental resolution as Gaussian. So in this case, double Gaussian which is sum of narrow width and wide width Gaussian, is good approximation. The mean and width are floated in favored mode fitting. In the suppressed mode, these values are fixed to corresponding the favored mode results. The ratio of area and width are fixed to the value of corresponding signal Monte Carlo.

Regarding $q\bar{q}$ background, its shape is modeled as a linear function. Its slope is determined from "uds" and "charm" Monte Carlo.

Backgrounds from other B decays, distribute as shown in Figure 3.19. $B^- \rightarrow D\rho^-$ and $B^- \rightarrow D^*\pi^-$ distribute in the negative ΔE region and make a small contribution to the signal region. These background shape is modeled as a smoothed histogram from generic Monte Carlo.

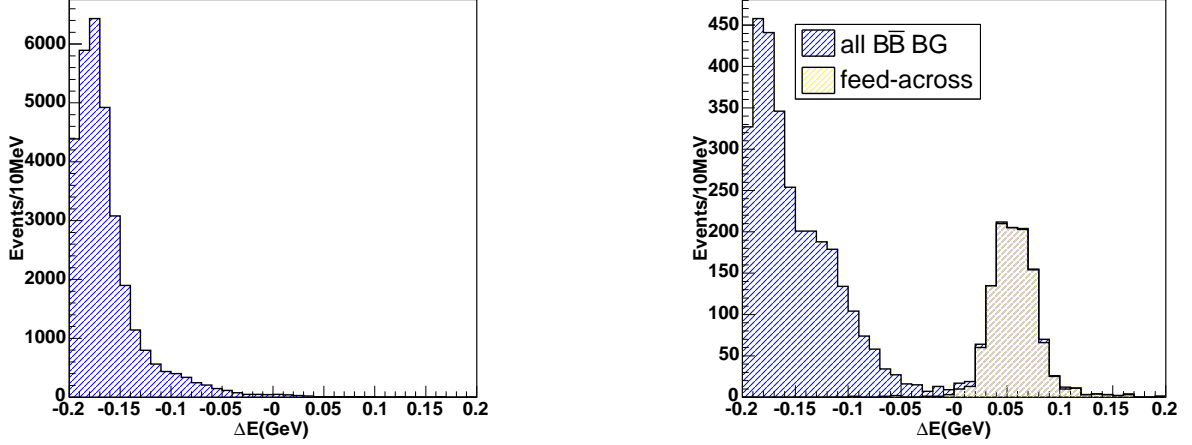


Figure 3.19: $B\bar{B}$ background for $B^- \rightarrow D_{fav}\pi^-$ (left) and $B^- \rightarrow D_{fav}K^-$ (right)

For $B^- \rightarrow DK^-$ decay mode, there is an additional component due to feed-across from $D_{fav}\pi^-$ as shown in Figure 3.19 by particle miss identification. Its contribution is modeled as a Gaussian shape that has different widths on the left and right sides of the peak (so-called Bifurcated-Gaussian), since the shift caused by wrong mass assignment makes the shape asymmetric. The widths and mean are determined by $B^- \rightarrow D_{fav}\pi^-$ data reconstruction with changing mass assignment for K .

The fit results are shown in Figure 3.20. The numbers of events for $B^- \rightarrow D_{sup}h^-$ and $B^- \rightarrow D_{fav}h^-$ are given in Table 5.1.

Mode	Efficiency(%)	Signal Yield
$B^- \rightarrow D_{fav}\pi^-$	25.6 ± 0.3	15051 ± 126.8
$B^- \rightarrow D_{sup}\pi^-$	25.9 ± 0.3	52.2 ± 10.5
$B^- \rightarrow D_{fav}K^-$	16.6 ± 0.2	723 ± 31
$B^- \rightarrow D_{sup}K^-$	16.8 ± 0.2	10.1 ± 5.9

Table 3.3: Efficiency and signal yields.

3.3.2 Ratio of branching fractions R_{Dh}

Ratios of product branching fractions, defined as

$$R_{Dh} \equiv \frac{\mathcal{B}(B^- \rightarrow D_{sup}h^-)}{\mathcal{B}(B^- \rightarrow D_{fav}h^-)} = \frac{N_{D_{sup}h^-}/\epsilon_{D_{sup}h^-}}{N_{D_{fav}h^-}/\epsilon_{D_{fav}h^-}},$$

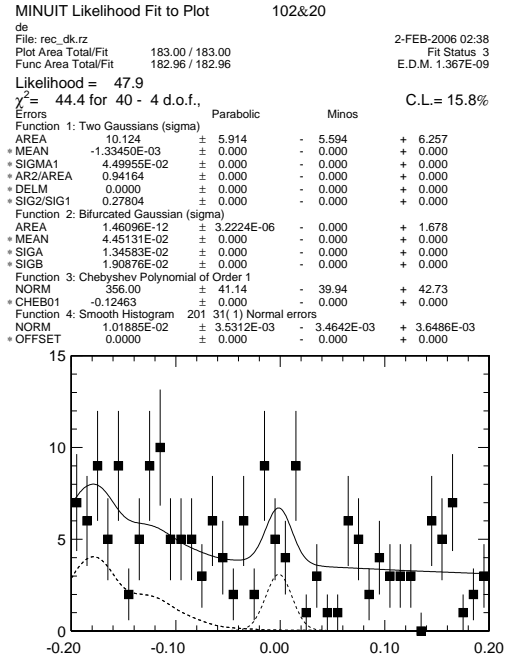
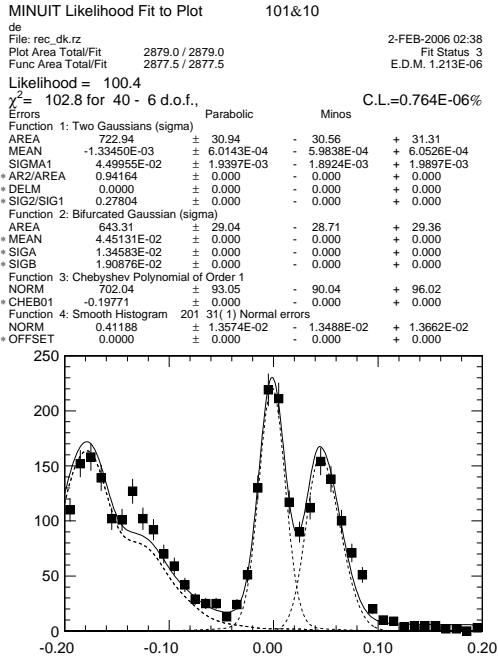
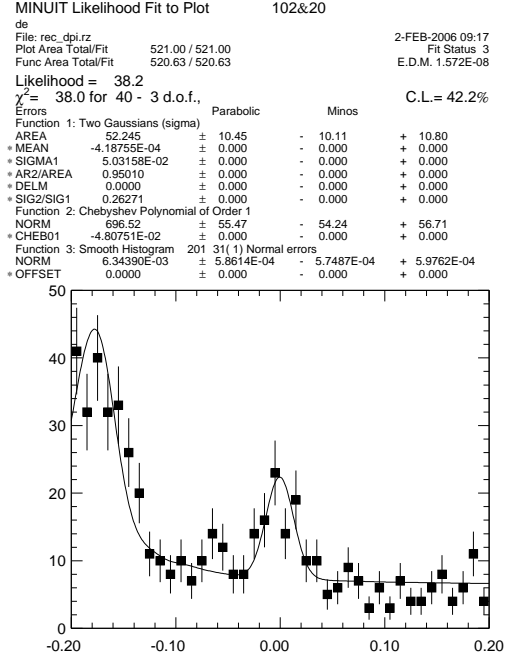
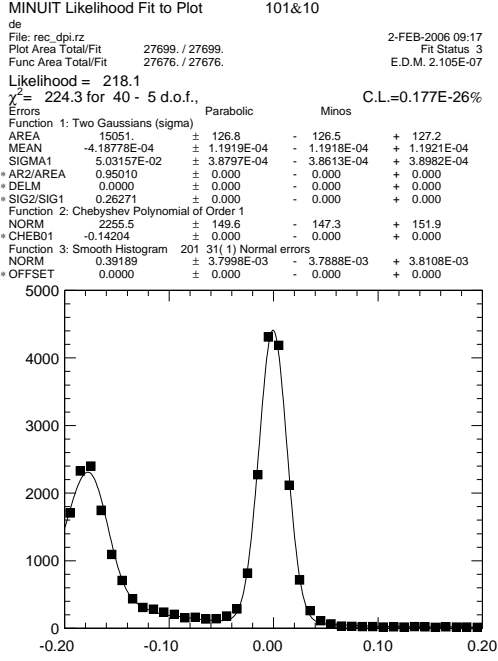


Figure 3.20: ΔE -fit result of $B^- \rightarrow D_{fav}\pi^-$ (top right), $B^- \rightarrow D_{sup}\pi^-$ (top left), $B^- \rightarrow D_{fav}K^-$ (bottom right) and $B^- \rightarrow D_{sup}K^-$ (bottom left).

are calculated where $N_{D_{sup}h^-}$ ($N_{D_{fav}h^-}$) and $\epsilon_{D_{sup}h^-}$ ($\epsilon_{D_{fav}h^-}$) are the number of signal events and the reconstruction efficiency for the decay $B^- \rightarrow D_{sup}h^-$ ($B^- \rightarrow D_{fav}h^-$), and are given in Table 5.1. We obtain

$$R_{DK} = (1.4 \pm 0.8(stat) \pm 0.1(syst)) \times 10^{-2},$$

$$R_{D\pi} = (3.5 \pm 0.7(stat)) \times 10^{-3}.$$

Since the signal for $B^- \rightarrow D_{sup}K^-$ is not significant, we set an upper limit as

$$R_{DK} < 2.8 \times 10^{-2} \quad 90\% \text{ confidence level}$$

where we take the likelihood function as a Gaussian distribution with width given by the quadratic sum of statistical and systematic errors, and the area is normalized in the physical region of positive branching fraction.

Most of the systematic uncertainties from the detection efficiencies and the particle identification are canceled by taking the ratios, since the kinematics of the $B^- \rightarrow D_{sup}h^-$ and $B^- \rightarrow D_{fav}h^-$ processes are similar. The systematic errors are due to uncertainties in the yield extraction and the efficiency difference between $B^- \rightarrow D_{sup}h^-$ and $B^- \rightarrow D_{fav}h^-$ as listed in Table 3.4.

Mode	$B^- \rightarrow D_{fav}K^-$	$B^- \rightarrow D_{sup}K^-$
signal shape	$\pm 0.4\%$	$\pm 4.6\%$
$q\bar{q}$ background	$\pm 0.2\%$	$\pm 1.3\%$
feed-across shape	$\pm 1.1\%$	$\pm 0.1\%$
$B\bar{B}$ background	$\pm 0.7\%$	$\pm 0.8\%$
efficiency	$\pm 0.4\%$	$\pm 0.4\%$
total	$\pm 1.4\%$	$\pm 4.9\%$

Table 3.4: Systematic uncertainties for $B^- \rightarrow D_{fav}K^-$ and $B^- \rightarrow D_{sup}K^-$ signal yield

The uncertainties in the signal shapes, the $q\bar{q}$ background shapes and feed-across shape are determined by varying the shape of the fitting function by $\pm 1\sigma$ which is fitting-error of reference. The uncertainties in the $B\bar{B}$ background shapes are determined by fitting the ΔE distribution in the region $-0.07 < \Delta E < 0.20$ [GeV] ignoring the $B\bar{B}$ background contributions. The uncertainties in the efficiency differences are determined using signal MC.

The total systematic error is the sum in quadrature of the above uncertainties. The ratio R_{DK} is related to ϕ_3 by the following equation

$$R_{DK} = r_B^2 + r_D^2 + 2r_{B^*}r_D \cos \phi_3 \cos \delta, \quad (3.9)$$

where [8]

$$r_B \equiv \left| \frac{A(B^- \rightarrow \bar{D}^0 K^-)}{A(B^- \rightarrow D^0 K^-)} \right| \quad (3.10)$$

$$\delta \equiv \delta_B + \delta_D \quad (3.11)$$

$$r_D \equiv \left| \frac{A(D^0 \rightarrow K^+ \pi^-)}{A(D^0 \rightarrow K^- \pi^+)} \right| = 0.060 \pm 0.003[PDG] \quad (3.12)$$

and δ_B (δ_D) are the strong phase differences between the two B (D) decay amplitudes, respectively. Using the above result, a limit on r_B is obtained. The least restrictive limit is obtained allowing $\pm 2\sigma$ variation on r_D and assuming maximal interference ($\phi_3 = 0^\circ$, $\delta = 180^\circ$ or $\phi_3 = 180^\circ$, $\delta = 0^\circ$) and is found to be

$$r_{B,DK} < 0.23 \text{ at the } 90\% \text{ confidence level} \quad (3.13)$$

as shown in Figure 3.21. And we also compare this result with one of Belle Dalitz analysis [4] and BaBar [14]. These results are consistent within these errors.

$$\text{Belle Dalitz analysis : } r_{B,DK} = 0.26_{-0.14}^{+0.10}(\text{stat}) \pm 0.03(\text{syst}) \pm 0.04(\text{model}) \quad (3.14)$$

$$\text{BaBar : } r_{B,DK} < 0.23 \text{ at the } 90\% \text{ confidence level} \quad (3.15)$$

3.3.3 Charge separated yield

CP violating asymmetry is searched in the $B^\pm \rightarrow D_{sup}K^\pm$ mode. The B^+ and B^- yields separately are determined as shown in Figure 3.22. That yields are found to be 9.64 ± 4.8 events for $B^- \rightarrow D_{sup}K^-$ and 0.00 ± 3.4 events for $B^+ \rightarrow D_{sup}K^+$. And expediently quantities which related to these yields are defined as

$$R_{DK}^\pm \equiv \frac{\mathcal{B}(B^\pm \rightarrow D_{sup}K^\pm)}{(\mathcal{B}(B^- \rightarrow D_{fav}K^-) + \mathcal{B}(B^+ \rightarrow D_{fav}K^+))/2} \quad (3.16)$$

$$R_{DK}^+ = (0.0 \pm 0.9(\text{stat}) \pm 0.1(\text{syst})) \times 10^{-2} \quad (3.17)$$

$$R_{DK}^- = (1.3 \pm 0.9(\text{stat}) \pm 0.1(\text{syst})) \times 10^{-2}. \quad (3.18)$$

Where systematic uncertainties arise from the B^+ and B^- yield extraction (4%; determined as for R_{DK}), detector charge asymmetry (2.5%; determined from the $B^\pm \rightarrow D_{fav}\pi^\pm$ sample), and PID efficiency of prompt K (1%) [12]. The total systematic error is obtained by taking the quadratic sum.

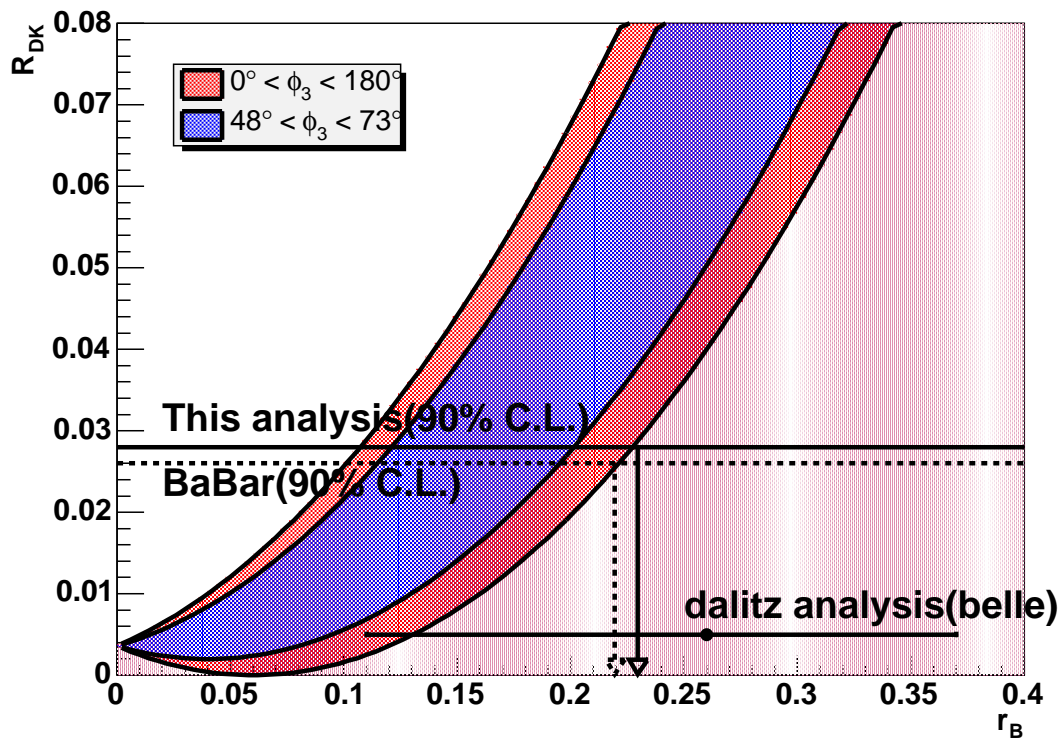


Figure 3.21: r_B dependence of R_{DK} and comparison with results of Belle Dalitz analysis [4] ($r_{B,DK} = 0.26^{+0.10}_{-0.14}(stat) \pm 0.03(syst) \pm 0.04(model)$) and BaBar [14] ($r_{B,DK} < 0.23$ at the 90% confidence level)

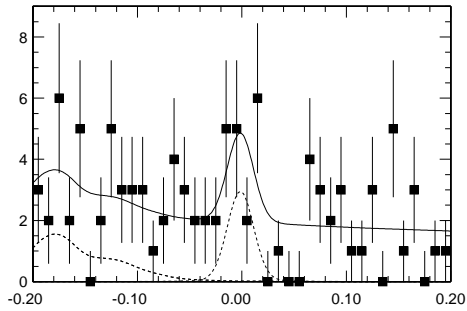
Yield extraction	$\pm 4\%$
Intrinsic detector bias	$\pm 2.5\%$
PID efficiency of prompt K	$\pm 1\%$
Total	$\pm 4.8\%$

Table 3.5: Systematic uncertainties for A_{DK}^{\pm}

MINUIT Likelihood Fit to Plot 101&10
 de
 File: rec_dk.rz 1-FEB-2006 10:30
 Plot Area Total/Fit 97.000 / 97.000 Fit Status 3
 Func Area Total/Fit 96.976 / 96.976 E.D.M. 3.309E-06

Likelihood = 48.6
 $\chi^2 = 40.3$ for 40 - 4 d.o.f., C.L. = 28.7%

Errors	Parabolic	Minos
Function 1: Two Gaussians (sigma)		
AREA	9.6397 ± 4.751	- 4.465 + 5.135
* MEAN	-1.33450E-03 ± 0.000	- 0.000 + 0.000
* SIGMA1	4.49955E-02 ± 0.000	- 0.000 + 0.000
* AR2/AREA	0.94164 ± 0.000	- 0.000 + 0.000
* DELM	0.0000 ± 0.000	- 0.000 + 0.000
* SIG2/SIG1	0.27804 ± 0.000	- 0.000 + 0.000
Function 2: Bifurcated Gaussian (sigma)		
AREA	2.37732E-06 ± 3.4305E-03	- 0.000 + 1.193
* MEAN	4.45131E-02 ± 0.000	- 0.000 + 0.000
* SIGA	1.34583E-02 ± 0.000	- 0.000 + 0.000
* SIGB	1.90876E-02 ± 0.000	- 0.000 + 0.000
Function 3: Chebyshev Polynomial of Order 1		
NORM	189.13 ± 30.40	- 28.42 + 31.17
* CHEB01	-0.12463 ± 0.000	- 0.000 + 0.000
Function 4: Smooth Histogram 201 31(1) Normal errors		
NORM	3.91200E-03 ± 2.4591E-03	- 2.3383E-03 + 2.5290E-03
* OFFSET	0.0000 ± 0.000	- 0.000 + 0.000



MINUIT Likelihood Fit to Plot 102&20
 de
 File: rec_dk.rz 1-FEB-2006 10:30
 Plot Area Total/Fit 88.000 / 88.000 Fit Status 3
 Func Area Total/Fit 87.974 / 87.974 E.D.M. 1.568E-06

Likelihood = 41.8
 $\chi^2 = 37.0$ for 40 - 4 d.o.f., C.L. = 42.1%

Errors	Parabolic	Minos
Function 1: Two Gaussians (sigma)		
AREA	3.60590E-03 ± 3.443	- 3.151 + 3.809
* MEAN	-1.33450E-03 ± 0.000	- 0.000 + 0.000
* SIGMA1	4.49955E-02 ± 0.000	- 0.000 + 0.000
* AR2/AREA	0.94164 ± 0.000	- 0.000 + 0.000
* DELM	0.0000 ± 0.000	- 0.000 + 0.000
* SIG2/SIG1	0.27804 ± 0.000	- 0.000 + 0.000
Function 2: Bifurcated Gaussian (sigma)		
AREA	6.60206E-07 ± 3.4073E-03	- 0.000 + 2.687
* MEAN	4.45131E-02 ± 0.000	- 0.000 + 0.000
* SIGA	1.34583E-02 ± 0.000	- 0.000 + 0.000
* SIGB	1.90876E-02 ± 0.000	- 0.000 + 0.000
Function 3: Chebyshev Polynomial of Order 1		
NORM	170.90 ± 27.12	- 27.66 + 30.29
* CHEB01	-0.12463 ± 0.000	- 0.000 + 0.000
Function 4: Smooth Histogram 201 31(1) Normal errors		
NORM	6.56442E-03 ± 2.4932E-03	- 2.5191E-03 + 2.6928E-03
* OFFSET	0.0000 ± 0.000	- 0.000 + 0.000

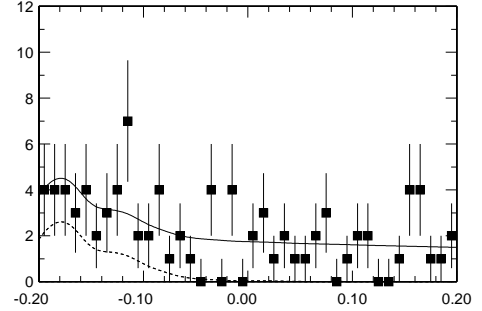


Figure 3.22: charge separated ΔE distribution of $B^- \rightarrow D_{sup}K^-$ (left) and $B^+ \rightarrow D_{sup}K^+$ (right) mode

3.3.4 Constraint for ϕ_3

The constraint for ϕ_3 is determined with the result of $B^- \rightarrow D_{CP}K^-$ analysis. To give a constraint, the result of Belle $B^- \rightarrow D_{cp}K$ analysis [13] as shown in bellow is used.

$$R_{DK}^+ = (0.0 \pm 0.9(stat) \pm 0.1(syst)) \times 10^{-2} \quad (3.19)$$

$$R_{DK}^- = (1.3 \pm 0.9(stat) \pm 0.1(syst)) \times 10^{-2} \quad (3.20)$$

$$A_1 = 0.07 \pm 0.14(stat) \pm 0.06(sys) \quad (3.21)$$

$$A_2 = -0.11 \pm 0.14(stat) \pm 0.05(sys) \quad (3.22)$$

$$R_1 = 0.98 \pm 0.18(stat) \pm 0.10(sys) \quad (3.23)$$

$$R_2 = 1.29 \pm 0.16(stat) \pm 0.08(sys) \quad (3.24)$$

Those observable are represented as

$$R_{DK}^\pm \equiv \frac{\mathcal{B}(B^\pm \rightarrow D_{sup}K^\pm)}{(\mathcal{B}(B^- \rightarrow D_{fav}K^-) + \mathcal{B}(B^+ \rightarrow D_{fav}K^+))/2} \quad (3.25)$$

$$= r_B^2 + r_D^2 + 2r_B r_D \cos(\delta \pm \phi_3) \quad (3.26)$$

$$A_{1,2} \equiv \frac{\mathcal{B}(B^- \rightarrow D_{1,2}K^-) - \mathcal{B}(B^+ \rightarrow D_{1,2}K^+)}{\mathcal{B}(B^- \rightarrow D_{1,2}K^-) + \mathcal{B}(B^+ \rightarrow D_{1,2}K^+)} \quad (3.27)$$

$$= \frac{2r_B \sin \delta'_{cp} \sin \phi_3}{1 + r_B^2 + 2r_B \cos \delta'_{cp} \cos \phi_3} \quad (3.28)$$

$$R_{1,2} \equiv \frac{R^{D_{1,2}}}{R^{D^0}} \quad (3.29)$$

$$= 1 + r_B^2 + 2r_B \cos \delta'_{cp} \cos \phi_3 \quad (3.30)$$

$$\delta'_{cp} \equiv \begin{cases} \delta_{cp} & \text{for } D_1 \\ \delta_{cp} + \pi & \text{for } D_2. \end{cases} \quad (3.31)$$

However $A_{1,2}$ and $R_{1,2}$ are not perfectly independent. There is the correlation as

$$A_1 R_1 = -A_2 R_2. \quad (3.32)$$

So to avoid a complicated situation on χ^2 calculation with a correlation, A_1 and A_2 are converted to AR which is defined as

$$AR \equiv A_1 R_1 - A_2 R_2 \quad (3.33)$$

$$= 4r_B \sin \delta_{cp} \sin \phi_3. \quad (3.34)$$

We have 5 equations and 4 unknown values which are ϕ_3 , r_B , δ and δ_{cp} . Changing these parameters χ^2 between measured value and equation is obtained in each parameter space. Then using $\Delta\chi^2 = \chi^2 - \chi_{min}^2$, favored regions for $r_{B,DK}$ and ϕ_3 is determined. The result is shown in Figure 3.23.

Moreover to determine ϕ_3 with more accuracy, we also use the world average of $B^- \rightarrow D_{cp}K^-$ analysis result [15] and this result is shown in Figure 3.24.

$$A_1 = 0.22 \pm 0.11 \quad (3.35)$$

$$A_2 = 0.02 \pm 0.12 \quad (3.36)$$

$$R_1 = 0.91 \pm 0.12 \quad (3.37)$$

$$R_2 = 1.01 \pm 0.12 \quad (3.38)$$

Up to now we can not give a strict constraint for ϕ_3 because of low statistics In this result. However this method surely has a sensitivity for ϕ_3 . We can expect this method will give a more strict constraint with high statistics, especially certain suppressed mode signals.

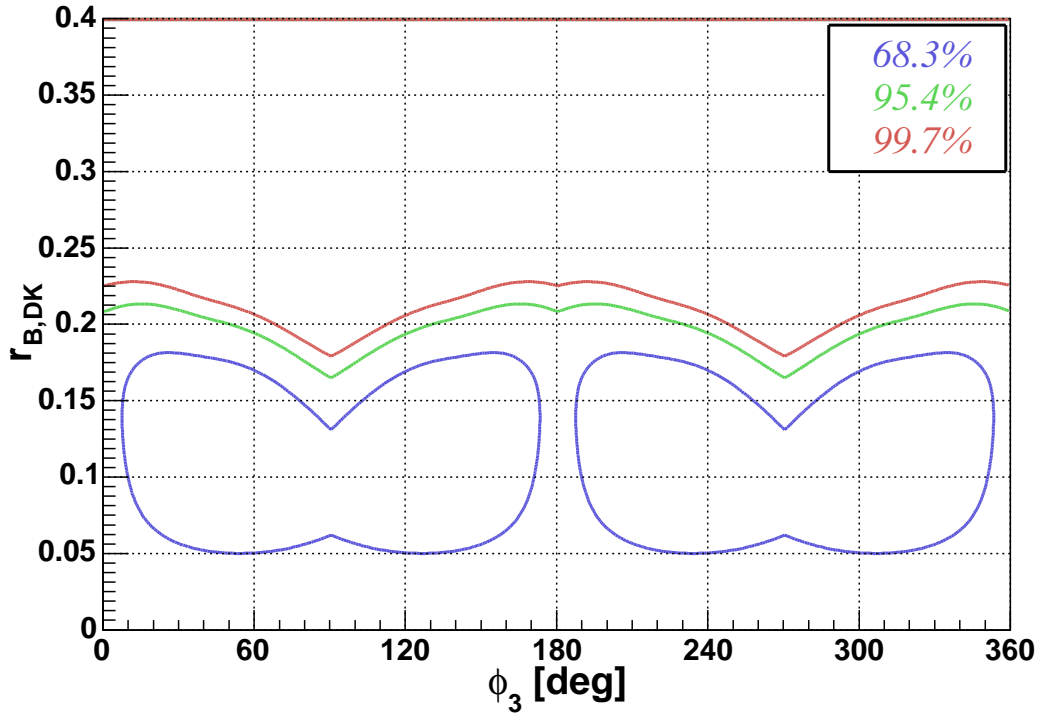


Figure 3.23: Constraint for ϕ_3 and $r_{B,DK}$ with Belle $B^- \rightarrow D_{cp}K^-$ result. These contours show favored region of each confidence levels.

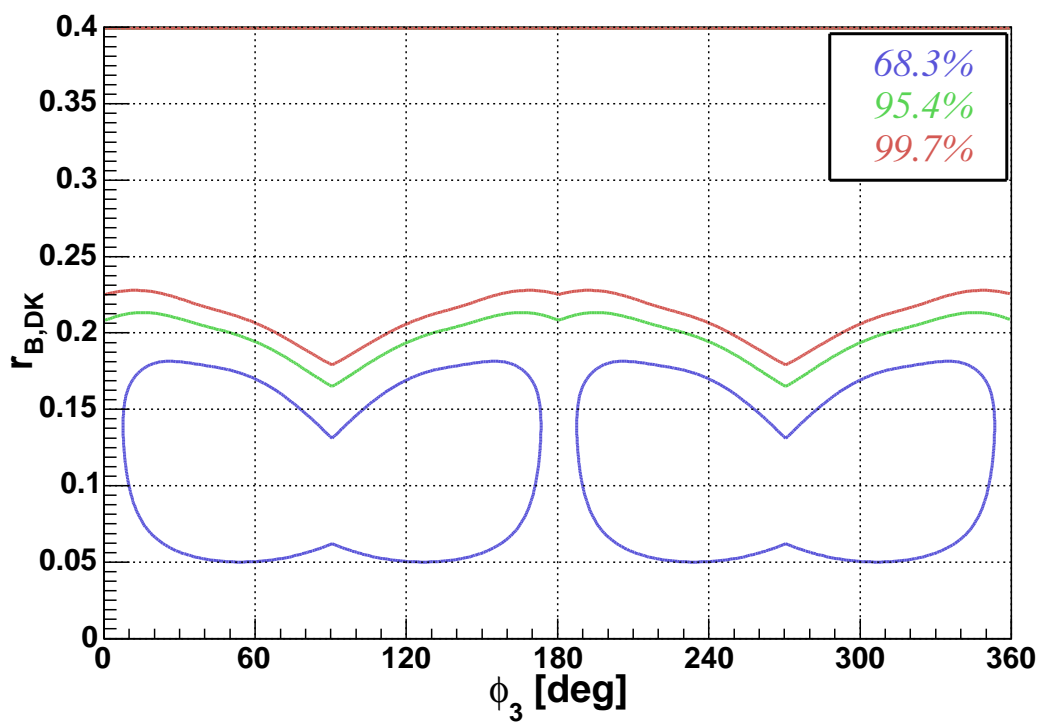


Figure 3.24: Constraint for ϕ_3 and $r_{B,DK}$ with the world average of $B^- \rightarrow D_{cp}K^-$ analysis result. These contours show favored region of each confidence levels.

Chapter 4

$B^- \rightarrow DK^{*-}$ analysis

In this chapter the procedure of $B^- \rightarrow DK^{*-}$ reconstruction is described. Almost of analysis procedures are same as $B^- \rightarrow DK^-$ analysis. So the description of the same cuts is skipped.

Historically the discovery of $B^- \rightarrow D_{fav}[K^-\pi^+]K^{*-}$ decay is earlier than the discovery of $B^- \rightarrow D_{fav}[K^-\pi^+]K^-$ decay. Even if $B^- \rightarrow D_{sup}[K^+\pi^-]K^-$ decay is not found, we may find $B^- \rightarrow D_{sup}[K^+\pi^-]K^{*-}$ decay.

4.1 Event selection criteria

4.1.1 K^{*-} reconstruction

- π tracks : $LR(K/\pi) < 0.7$
- Ks mass : $489 < M_{\pi^+\pi^-} < 507$ [MeV/c²](3σ)
- good K_s : Depending on momentum range these cuts are applied.

Momentum[GeV/c]	dr [cm]	$d\phi$ [cm]	z_{dist} [cm]	l_{flight} [cm]
< 0.5	> 0.05	< 0.3	< 0.8	-
$0.5 - 1.5$	> 0.03	< 0.1	< 1.8	> 0.08
> 1.5	> 0.02	< 0.03	< 2.4	> 0.22

where these parameters are defined as

- dr : This is the smaller of distances from IP in the direction perpendicular to beam axis ($x - y$ plane).
- $d\phi$: This is the angle between Ks and Ks daughter's momentum direction.

- z_{dist} : This is the distance between the two daughter tracks in IP.
- l_{flight} : This is the flight length of K_s candidate in $x - y$ plane.
- K^{*-} mass : $817 < M_{K_s\pi^-} < 967$ [MeV/ c^2]

K^{*-} candidates are reconstructed by combining K_s and π^- . K_s candidates are required to have a mass within ± 9 MeV/ c^2 (3σ) of its nominal mass value(Figure 4.1) and certain flight length depending its momentum. In K^{*-} reconstruction PID cut of π candidates are same as one of D daughter π . K^{*-} candidates are required to have a mass within ± 75 MeV/ c^2 of its nominal mass value as shown in Figure 4.2.

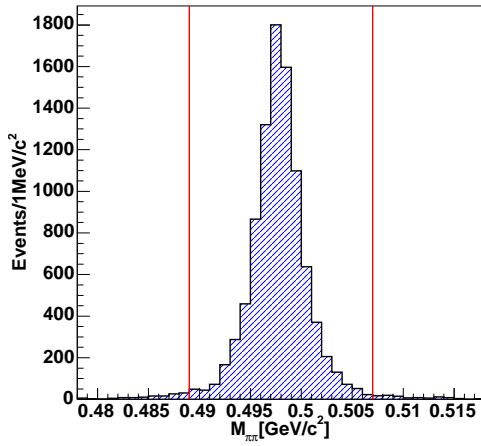


Figure 4.1: K_s mass distribution of signal Monte Carlo evnts

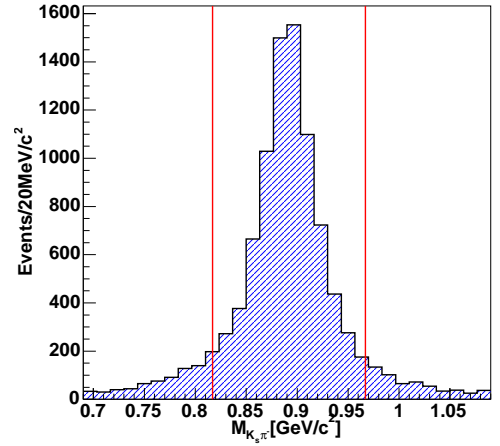


Figure 4.2: K^{*-} mass distribution of signal Monte Carlo events

4.1.2 B^- reconstruction

- $5.27 < M_{bc} < 5.29$ [GeV/ c^2]
- $|\Delta E| < 0.05$ [GeV]
- $|\cos \theta_{hel}| > 0.4$

B^- candidates are reconstructed by combining D and K^{*-} candidate satisfying the condition. In addition to M_{bc} and ΔE cut B^- candidates are required to helicity angle cut, $|\cos \theta_{hel}| > 0.4$. Since $B^- \rightarrow DK^{*-}$ decay is a pseudoscalar to pseudoscalar-vector decay, the K^{*-} is polarized. The K^{*-} helicity angle, θ_{hel} , is defined as angle between the momentum direction of one K^{*-} daughter and B in K^{*-} rest frame. By pseudoscalar to

pseudoscalar-vector decay that helicity angles have $\cos^2 \theta_{hel}$ distribution as shown in Figure 4.3. Moreover this cut is also effective for combinatoric background and $q\bar{q}$ continuum background suppression because those distributions are essentially flat.

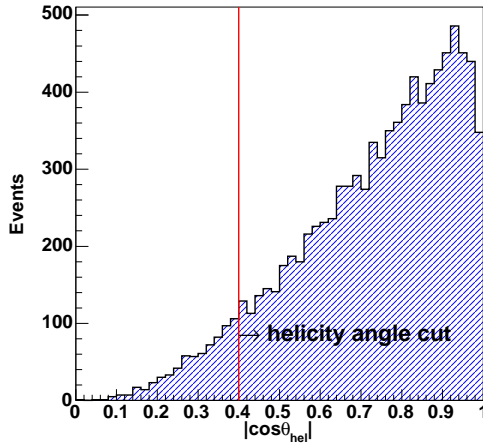


Figure 4.3: helicity angle distribution of signal Monte Carlo events

After applying all these cuts the distributions of ΔE and M_{bc} are shown in Figure 4.4, where the data set is signal Monte Carlo events.

4.1.3 $q\bar{q}$ continuum background suppression

- $LR_{(K_{SFW}, \cos\theta_B)} > 0.88$

Mode	#(signal)	#(background)	Expected \mathcal{B}	Efficiency(%)
$B^- \rightarrow D_{fav} K^{*-}$	362	233	5.2×10^{-6}	18.0
$B^- \rightarrow D_{sup} K^{*-}$	16.9	247	1.9×10^{-8}	19.3

Table 4.1: Expected number of signal and background events with 366 fb^{-1} data set ($386 \times 10^6 B\bar{B}$ pairs). These efficiencies are ones before event shape variable cut. These numbers of background events are estimated from "uds" and "charm" Monte Carlo events whose size are 532 fb^{-1} corresponding to 3 times events of experimental number 21 to 37(177.4 fb^{-1}).

To suppress $q\bar{q}$ continuum background the event shape likelihood ratio cut is optimized for $B^- \rightarrow D_{sup}[K^+\pi^-]K^{*-}$ mode. In that optimization "figure of merit" is used as an indicator. Figure 4.5 shows likelihood ratio distribution of signal Monte Carlo and M_{bc}

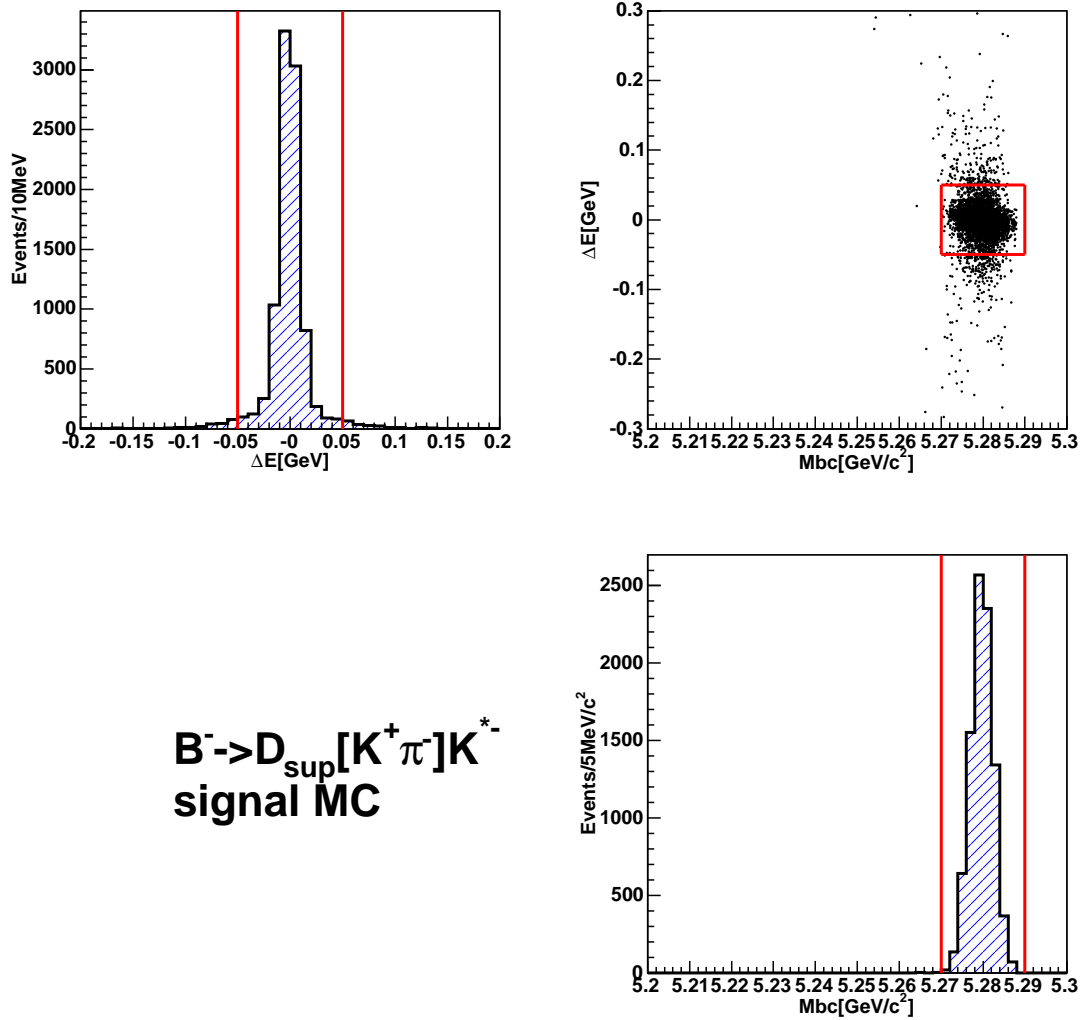


Figure 4.4: ΔE and M_{bc} distribution of signal Monte Carlo events

sideband data and "figure of merit" (F.o.M) distribution as a function of likelihood ratio cut point. The number of $q\bar{q}$ continuum background events is estimated from "uds" and "charm" Monte Carlo. On the other hand the number of signal events is estimated from central value of BaBar's result (R_{DK^*}) [17] and PDG product branching fraction as

$$\begin{aligned}
\mathcal{B}(B^- \rightarrow DK^{*-}) &= 6.1 \times 10^{-4} \\
\mathcal{B}(D^0 \rightarrow K^- \pi^+) &= 3.8 \times 10^{-2} \\
\mathcal{B}(K^{*-} \rightarrow K^0 \pi^-) &= \frac{2}{3} \\
\mathcal{B}(K^0 \rightarrow K_s \rightarrow \pi^+ \pi^-) &= \frac{1}{2} \times \frac{2}{3} \\
R_{DK^*} &= \frac{\mathcal{B}(B^- \rightarrow D_{sup} K^{*-})}{\mathcal{B}(B^- \rightarrow D_{fav} K^{*-})} \\
&= 0.046
\end{aligned}$$

4.1.4 Peaking background

To check the peaking background "generic Monte Carlo" events and "rare Monte Carlo" events are used. The results for ΔE and M_{bc} distributions are shown in Figure 4.6.

But for $B^- \rightarrow D_{sup}[K^+ \pi^-]K^{*-}$ mode particular background source is not found in signal region .

To check the effect of $B^- \rightarrow K^+ \pi^- K^{*-}$ decay we also check the D mass sideband as shown in Figure 4.7. However there is no peak.

4.2 Results

4.2.1 Fitting the ΔE distributions

To extract signal yield ΔE -fit is done assuming some fitting components as shown in Table 4.2.

Backgrounds from other B decays distribute as shown in Figure 4.8. The treatments of background, $B\bar{B}$ background and continuum background, is same as $B^- \rightarrow DK^-$ analysis. However we need not pay attention for feed-across because there is no mode corresponding to $B^- \rightarrow DK^{*-}$ mode such as $B^- \rightarrow D\pi^-$ decay feed-across in $B^- \rightarrow DK^-$ reconstruction. For the signal the sum of two Gaussian distributions which have same mean are used where its relative width and area are determined from signal Monte Carlo.

In the fit of the ΔE distribution for $B^- \rightarrow D_{fav} K^{*-}$ mode, the free parameters are the position, widths and area of the signal peak, the slope and normalization of the continuum component and the normalization of the $B\bar{B}$ background.

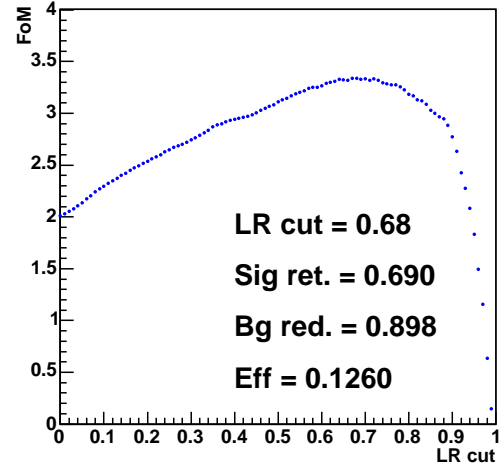
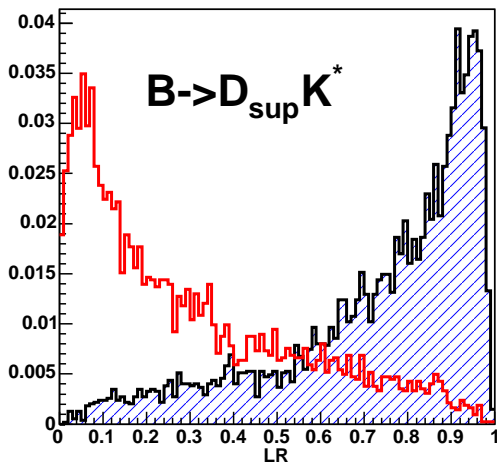
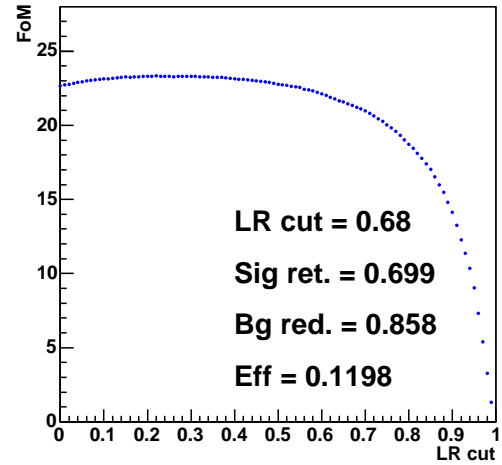
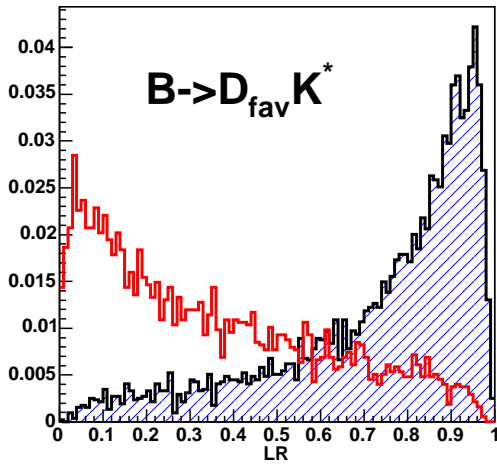


Figure 4.5: The event shape likelihood ratio distribution(left) and The "figure of merit" distribution(right)

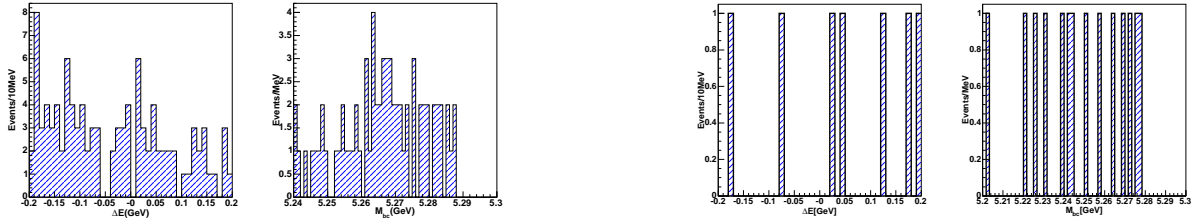


Figure 4.6: ΔE distribution of "generic" (left) and "rare" Monte Carlo evnts(right) for $B^- \rightarrow D_{sup}[K^+\pi^-]K^{*-}$

MINUIT Likelihood Fit to Plot 101&10
 de
 File: rec_dkst_kspi.rz 12-DEC-2005 11:59
 Plot Area Total/Fit 79.000 / 79.000 Fit Status: 3
 Func Area Total/Fit 77.952 / 77.952 E.D.M. 4.049E-06

Likelihood = 48.5
 $\chi^2 = 39.5$ for 40 - 4 d.o.f., C.L. = 31.6%

Errors	Parabolic	Minos	
Function 1: Two Gaussians (sigma)			
AREA	0.35550 ± 2.769	- 0.000	+ 3.269
* MEAN	0.0000 ± 0.000	- 0.000	+ 0.000
* SIGMA1	6.90221E-02 ± 0.000	- 0.000	+ 0.000
* AR2/AREA	0.92879 ± 0.000	- 0.000	+ 0.000
* DELM	0.0000 ± 0.000	- 0.000	+ 0.000
* SIG2/SIG1	0.14333 ± 0.000	- 0.000	+ 0.000
Function 2: Polynomial of Order 1			
NORM	154.29 ± 24.59	- 23.47	+ 24.89
* POLY01	0.0000 ± 0.000	- 0.000	+ 0.000
OFFSET	0.0000 ± 1.414	- 0.000	+ 0.000
Function 3: Smooth Histogram 201 31(1) Normal errors			
NORM	9.09649E-03 ± 3.3755E-03	- 3.1864E-03	+ 3.5617E-03
* OFFSET	0.0000 ± 0.000	- 0.000	+ 0.000

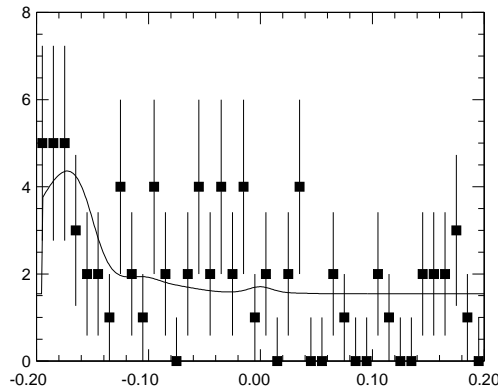


Figure 4.7: ΔE distribution of D mass sideband Data for $B^- \rightarrow D_{sup}[K^+\pi^-]K^{*-}$

Component	Function	Parameter	Fit
Signal	Double-gaussian	area	float
		mean	float→fix
		σ_1	float→fix
		area ₂ /area ₁	fix
		σ_2/σ_1	fix
$q\bar{q}$	Linear function	area	float
		slope	fix
$B\bar{B}$	Smoothed-histogram	area	float

Table 4.2: fitting components for $B^- \rightarrow DK^{*-}$

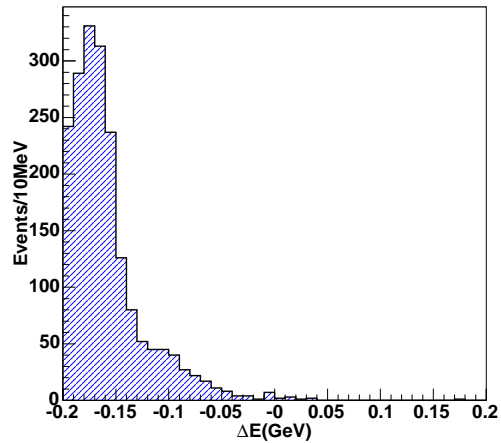


Figure 4.8: ΔE distribution of $B\bar{B}$ background for $B^- \rightarrow D_{fav}[K^-\pi^+]K^{*-}$

For $B^- \rightarrow D_{sup}K^{*-}$, the signal and $B\bar{B}$ background shapes are modeled using the results of the fits to the corresponding favored modes. The free parameters are the normalization of the three components.

The fit results are shown in Figure 4.9. The numbers of signal yield are listed in Table 4.3

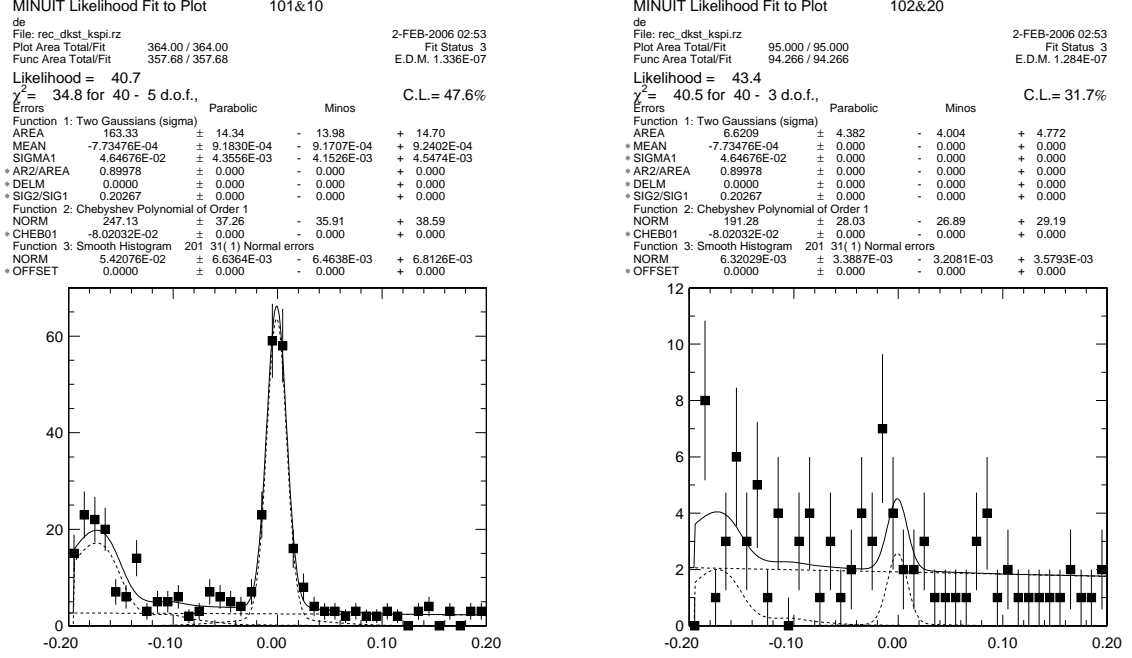


Figure 4.9: ΔE -fit result of $B^- \rightarrow D_{fav}K^{*-}$ (right) and $B^- \rightarrow D_{sup}K^{*-}$ (left)

Mode	Efficiency(%)	Signal Yield
$B^- \rightarrow D_{sup}K^{*-}$	12.0 ± 0.2	163 ± 14.3
$B^- \rightarrow D_{fav}K^{*-}$	12.6 ± 0.2	6.2 ± 4.4

Table 4.3: Efficiency and signal yields of $B^- \rightarrow DK^{*-}$ mode

4.2.2 Ratio of branching fractions R_{Dh}

In $B^- \rightarrow DK^{*-}$ mode the ratio of product branching fraction is calculated using the number of signal events and efficiency listed in Table 4.3.

We obtain

$$R_{DK^*} = (3.9 \pm 2.7(stat) \pm 0.4(sys)) \times 10^{-2}.$$

Since the signal for $B^- \rightarrow D_{sup}K^{*-}$ is not significant, we set an upper limit as

$$R_{DK^{*-}} < 8.7 \times 10^{-2} \quad 90\% \text{ confidence level}$$

,where we take the likelihood function as a Gaussian distribution with width given by the quadratic sum of statistical and systematic errors. The systematic errors are due to uncertainties in the yield extraction and the efficiency difference between $B^- \rightarrow D_{fav}K^{*-}$ and $B^- \rightarrow D_{sup}K^{*-}$ as listed in Table 4.4.

Mode	$B^- \rightarrow D_{fav}K^-$	$B^- \rightarrow D_{sup}K^-$
signal shape	$\pm 0.6\%$	$\pm 18.5\%$
$q\bar{q}$ background	$\pm 0.2\%$	$\pm 6.9\%$
$B\bar{B}$ background	$\pm 1.9\%$	$\pm 1.7\%$
efficiency	$\pm 0.2\%$	$\pm 0.2\%$
total	$\pm 1.4\%$	$\pm 19.8\%$

Table 4.4: Systematic uncertainties for $B^- \rightarrow D_{fav}K^{*-}$ and $B^- \rightarrow D_{sup}K^{*-}$ signal yield

The ratio R_{DK^*} is related to ϕ_3 by following equation

$$R_{DK^*} = r_B^2 + r_D^2 + 2r_{B,DK^*}r^D \cos \phi_3 \cos \delta,$$

where

$$r_{B,DK^*} \equiv \left| \frac{A(B^- \rightarrow \bar{D}^0 K^{*-})}{A(B^- \rightarrow D^0 K^{*-})} \right|$$

and with the same way as $B^- \rightarrow DK^-$ analysis the upper limit is obtained as

$$r_{B,DK^*} < 0.35 \text{ at the } 90\% \text{ confidence level,}$$

as shown in Figure 4.10. And we also compare this result with one of Belle Dalitz analysis [16] and BaBar [17]. These results are consistent within these errors.

$$\text{Belle Dalitz analysis : } r_{B,DK^*} = 0.25_{-0.22}^{+0.21} \quad (4.1)$$

$$\text{BaBar : } r_{B,DK^*} = 0.28_{-0.10}^{+0.06} \quad (4.2)$$

4.2.3 Charge separated yield

CP violating asymmetry is searched in the $B^\pm \rightarrow D_{sup}K^{*\pm}$ mode. The B^+ and B^- yields separately are determined as shown in Figure 4.11. That yields are found to be 4.8 ± 3.1

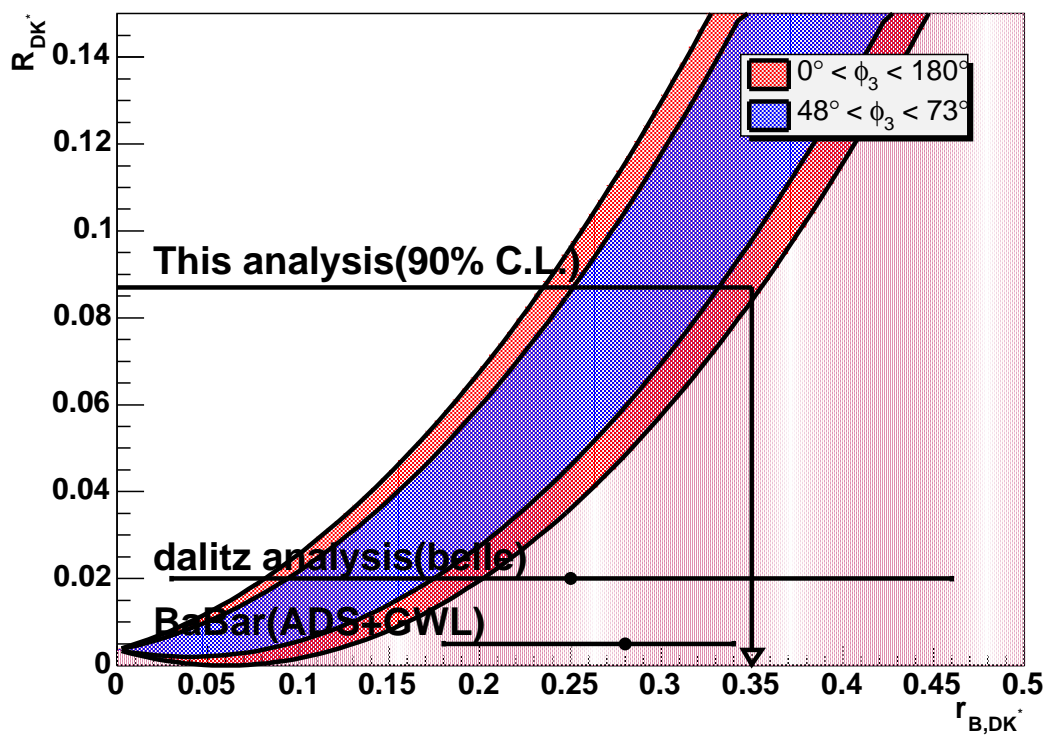
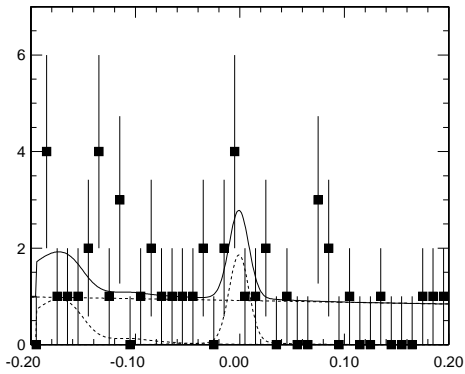


Figure 4.10: r_{B,DK^*} dependence of R_{DK^*} and comparison with results of Belle Dalitz analysis [16] ($r_{B,DK^*} = 0.25_{-0.18}^{+0.17}(stat) \pm 0.09(syst) \pm 0.04(model) \pm 0.08(background)$) and BaBar [17] ($r_{B,DK^*} = 0.28_{-0.10}^{+0.06}$)

MINUIT Likelihood Fit to Plot 101&10
 de
 File: rec_dkst_kspi.rz 2-FEB-2006 02:54
 Plot Area Total/Fit 47.000 / 47.000 Fit Status 3
 Func Area Total/Fit 46.652 / 46.652 E.D.M. 1.453E-08
 Likelihood = 41.9
 $\chi^2 = 37.0$ for 40 - 3 d.o.f., C.L.= 46.9%

Errors	Parabolic	Minos
Function 1: Two Gaussians (sigma)		
AREA	4.7683 ± 3.133 - 2.781 + 3.509	
* MEAN	-7.73476E-04 ± 0.000 - 0.000 + 0.000	
* SIGMA1	4.64676E-02 ± 0.000 - 0.000 + 0.000	
* AR2/AREA	0.89978 ± 0.000 - 0.000 + 0.000	
* DELM	0.0000 ± 0.000 - 0.000 + 0.000	
* SIG2/SIG1	0.20267 ± 0.000 - 0.000 + 0.000	
Function 2: Chebyshev Polynomial of Order 1		
NORM	91.565 ± 19.52 - 18.40 + 20.67	
* CHEB01	-8.02032E-02 ± 0.000 - 0.000 + 0.000	
Function 3: Smooth Histogram 201 31(1) Normal errors		
NORM	2.98398E-03 ± 2.4546E-03 - 2.2584E-03 + 2.6611E-03	
* OFFSET	0.0000 ± 0.000 - 0.000 + 0.000	



MINUIT Likelihood Fit to Plot 102&20
 de
 File: rec_dkst_kspi.rz 2-FEB-2006 02:54
 Plot Area Total/Fit 48.000 / 48.000 Fit Status 3
 Func Area Total/Fit 47.632 / 47.632 E.D.M. 1.253E-05
 Likelihood = 48.5
 $\chi^2 = 43.4$ for 40 - 3 d.o.f., C.L.= 21.6%

Errors	Parabolic	Minos
Function 1: Two Gaussians (sigma)		
AREA	1.1027 ± 3.129 - 0.000 + 3.537	
* MEAN	-7.73476E-04 ± 0.000 - 0.000 + 0.000	
* SIGMA1	4.64676E-02 ± 0.000 - 0.000 + 0.000	
* AR2/AREA	0.89978 ± 0.000 - 0.000 + 0.000	
* DELM	0.0000 ± 0.000 - 0.000 + 0.000	
* SIG2/SIG1	0.20267 ± 0.000 - 0.000 + 0.000	
Function 2: Chebyshev Polynomial of Order 1		
NORM	102.16 ± 20.62 - 19.46 + 21.71	
* CHEB01	-8.02032E-02 ± 0.000 - 0.000 + 0.000	
Function 3: Smooth Histogram 201 31(1) Normal errors		
NORM	3.21682E-03 ± 2.3588E-03 - 2.1940E-03 + 2.5410E-03	
* OFFSET	0.0000 ± 0.000 - 0.000 + 0.000	

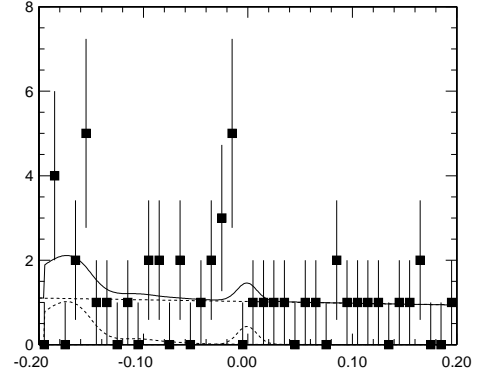


Figure 4.11: charge separated ΔE distribution of $B^- \rightarrow D_{sup}K^{*-}$ (right) and $B^+ \rightarrow D_{sup}K^{*+}$ mode (left)

events for $B^- \rightarrow D_{sup}K^{*-}$ and 1.1 ± 3.1 events for $B^+ \rightarrow D_{sup}K^{*+}$. And expediently quantities which related to these yields are defined as

$$R_{DK^*}^\pm \equiv \frac{\mathcal{B}(B^\pm \rightarrow D_{sup}K^{*\pm})}{(\mathcal{B}(B^- \rightarrow D_{fav}K^{*-}) + \mathcal{B}(B^+ \rightarrow D_{fav}K^{*+}))/2} \quad (4.3)$$

$$R_{DK^*}^+ = (1.4 \pm 3.8(stat) \pm 0.2(sys)) \times 10^{-2} \quad (4.4)$$

$$R_{DK^*}^- = (6.1 \pm 3.8(stat) \pm 0.9(sys)) \times 10^{-2}. \quad (4.5)$$

$$(4.6)$$

where systematic uncertainties arise from the B^+ and B^- yield extraction (11.1%; determined as for R_{DK^*}) and detector charge asymmetry (2.5%; determined from the $B^- \rightarrow D_{fav}\pi^-$ sample). The total systematic error is obtained by taking the quadratic sum.

Yield extraction	$\pm 11.1\%$
Intrinsic detector bias	$\pm 2.5\%$
Total	$\pm 11.2\%$

Table 4.5: Systematic uncertainties for A_{DK^*}

4.2.4 Constraint for ϕ_3

Using result of this analysis and BaBar's measurement of $B^- \rightarrow D_{CP}K^{*-}$ [18] as bellow, a constraint for ϕ_3 is determined.

$$R_{DK^*}^+ = (1.4 \pm 3.8(stat) \pm 0.2) \times 10^{-2} \quad (4.7)$$

$$R_{DK^*}^- = (6.1 \pm 3.8(stat) \pm 0.9) \times 10^{-2} \quad (4.8)$$

$$A_1 = -0.08 \pm 0.19(stat) \pm 0.08(sys) \quad (4.9)$$

$$A_2 = -0.26 \pm 0.40(stat) \pm 0.12(sys) \quad (4.10)$$

$$R_1 = 1.96 \pm 0.40(stat) \pm 0.11(sys) \quad (4.11)$$

$$R_2 = 0.65 \pm 0.26(stat) \pm 0.08(sys) \quad (4.12)$$

The same method as $B^- \rightarrow DK^-$ analysis is used to give a constraint for $\phi_3 - r_{B,DK^*}$. The result as shown in Figure 4.12 is obtained.

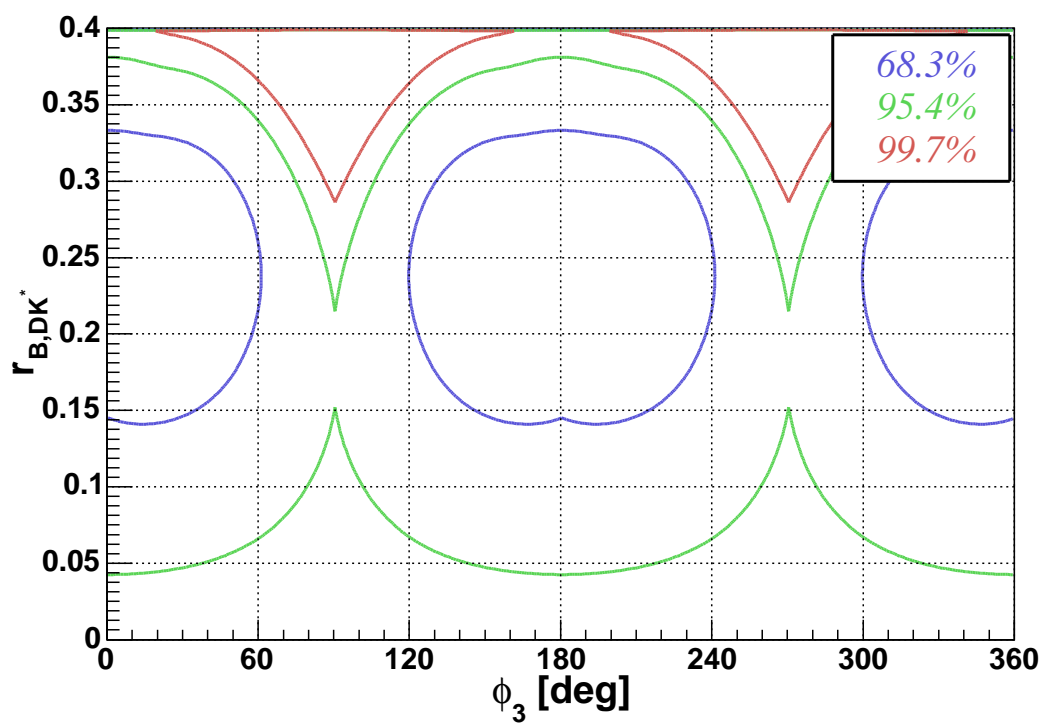


Figure 4.12: Constraint for ϕ_3 and r_{B,DK^*} . These contours show favored region of each confidence levels.

Chapter 5

$B^- \rightarrow D^* K^-$ analysis

In this chapter the procedure of $B^- \rightarrow D^* K^-$ reconstruction is described. But almost of analysis procedures are same as $B^- \rightarrow DK^-$ analysis. So the description of same cuts are skipped. To confirm my analysis method $B^- \rightarrow D^* \pi^-$ mode is also analyzed.

In this analysis product branching ratios, $R_{D^*[D\pi^0]K}$ and $R_{D^*[D\gamma]K}$, are measured. Since there is theoretical relation between product branching ratios and r_{B,D^*K} as $r_{B,D^*K}^2 = \frac{R_{D^*[D\pi^0]K} + R_{D^*[D\gamma]K}}{2} - r_D^2$, strong constraint for r_{B,D^*K} is extracted. That information of r_{B,D^*K} is important input for ϕ_3 determination.

5.1 Event selection criteria

5.1.1 D^{*-} reconstruction

- mass difference : $\Delta m \equiv m_{D^*} - m_D$
 - $139 < \Delta m < 145$ [MeV] (3σ) for $D\pi^0$ mode
 - $131 < \Delta m < 147$ [MeV] (2σ) for $D\gamma$ mode
- π^0 selection
 - γ energy : $E_\gamma > 30$ MeV
 - mass χ^2 : $\chi_{m_{\pi^0}}^2 \equiv \frac{m_{\gamma\gamma} - m_{\pi^0}^{nominal}}{\sigma} < 25$
- γ selection (these cuts is not applied to π daughters)
 - γ energy : $E_\gamma > 150$ MeV
 - π^0 χ^2 : $\chi_{m_{\pi^0}}^2 > 10$

D^* candidates are reconstructed by combination of $D\pi^0$ or $D\gamma$. To get D^* candidates effectively mass difference($\Delta m \equiv M_{D^*cand.} - M_{Dcand.}$) is used instead of D^* mass. Its cut value corresponds to 3σ or 2σ of experimental resolution as Figure 5.1. In the case of $D\gamma$ mode its range is asymmetric because of shower leakage in the calorimeter(ECL).

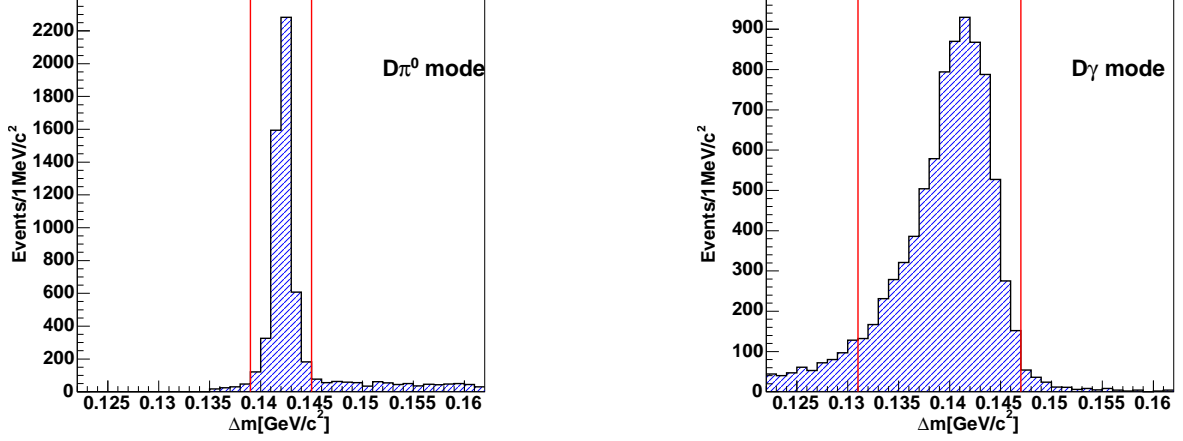


Figure 5.1: Δm distribution of signal Monte Carlo evnts of $D\pi^0$ (right) and $D\gamma$ mode(left)

π^0 candidates are reconstructed by combining of two γ s whose energy is grater than 30 MeV to suppress low energy π^0 fake. And it's mass χ^2 is required to be smaller than 25.

By low energy γ background $B^- \rightarrow Dh^-$ makes background for $B^- \rightarrow D^*h^-$. But that fake γ events are distinguished by γ energy as shown in Figure 5.2. For γ from D^* its energy is required to be grater than 150 MeV. To suppress low energy γ background this cut is tighter than one of π^0 daughters. π^0 veto is also used to suppress the contamination. Checking the all combination of γ s, one which can form π^0 , $\chi^2_{m_{\pi^0}} < 10$, is rejected.

5.1.2 B^- reconstruction

- $5.27 < M_{bc} < 5.29[\text{GeV}/c^2]$
- $|\Delta E| < 0.05[\text{GeV}]$

B^- candidates are reconstructed by combination of D^*K^- or $D^*\pi^-$ candidate satisfying the condition.

Typical ΔE and M_{bc} distributions of $B^- \rightarrow D^*K^-$ modes are plotted in Figure 5.3 and 5.4 .

5.1.3 $q\bar{q}$ continuum background suppression

- $D^*[D\pi^0]\pi^-$ mode : $LR_{(KSF\bar{W}, \cos\theta_B)} > 0.59$

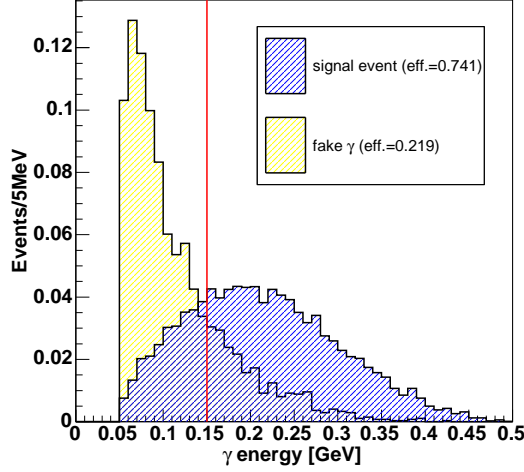


Figure 5.2: γ energy distributions of signal and fake γ events

- $D^*[D\pi^0]K^-$ mode : $LR_{(KSFW, \cos\theta_B)} > 0.80$
- $D^*[D\gamma]\pi^-$ mode : $LR_{(KSFW, \cos\theta_B)} > 0.89$
- $D^*[D\gamma]K^-$ mode : $LR_{(KSFW, \cos\theta_B)} > 0.90$

Mode	#(signal)	#(background)	Expected \mathcal{B}	Efficiency(%)
$B^- \rightarrow D_{fav}^*[D\pi^0]\pi^-$	12825	136	1.2×10^{-4}	13.8
$B^- \rightarrow D_{sup}^*[D\pi^0]\pi^-$	47.4	57	4.2×10^{-7}	14.6
$B^- \rightarrow D_{fav}^*[D\pi^0]K^-$	911	48	9.1×10^{-6}	13.0
$B^- \rightarrow D_{sup}^*[D\pi^0]K^-$	3.3	121	3.3×10^{-8}	13.0
$B^- \rightarrow D_{fav}^*[D\gamma]\pi^-$	10270	487	5.8×10^{-5}	22.9
$B^- \rightarrow D_{sup}^*[D\gamma]\pi^-$	37.2	237	2.1×10^{-7}	23.0
$B^- \rightarrow D_{fav}^*[D\gamma]K^-$	721	138	4.5×10^{-6}	20.7
$B^- \rightarrow D_{sup}^*[D\gamma]K^-$	2.8	343	1.7×10^{-8}	21.4

Table 5.1: Expected number of signal and background events with 366 fb^{-1} data set ($386 \times 10^6 B\bar{B}$ pairs). These efficiencies are ones before event shape variable cut. These numbers of background events are estimated from "uds" and "charm" Monte Carlo events whose size are 532 fb^{-1} corresponding to 3 times events of experimental number 21 to 37(177.4 fb^{-1}).

To suppress $q\bar{q}$ continuum background the event shape likelihood ratio cut is optimized for each suppressed mode based on "figure of merit"(F.o.M) Figure 5.5 shows likelihood

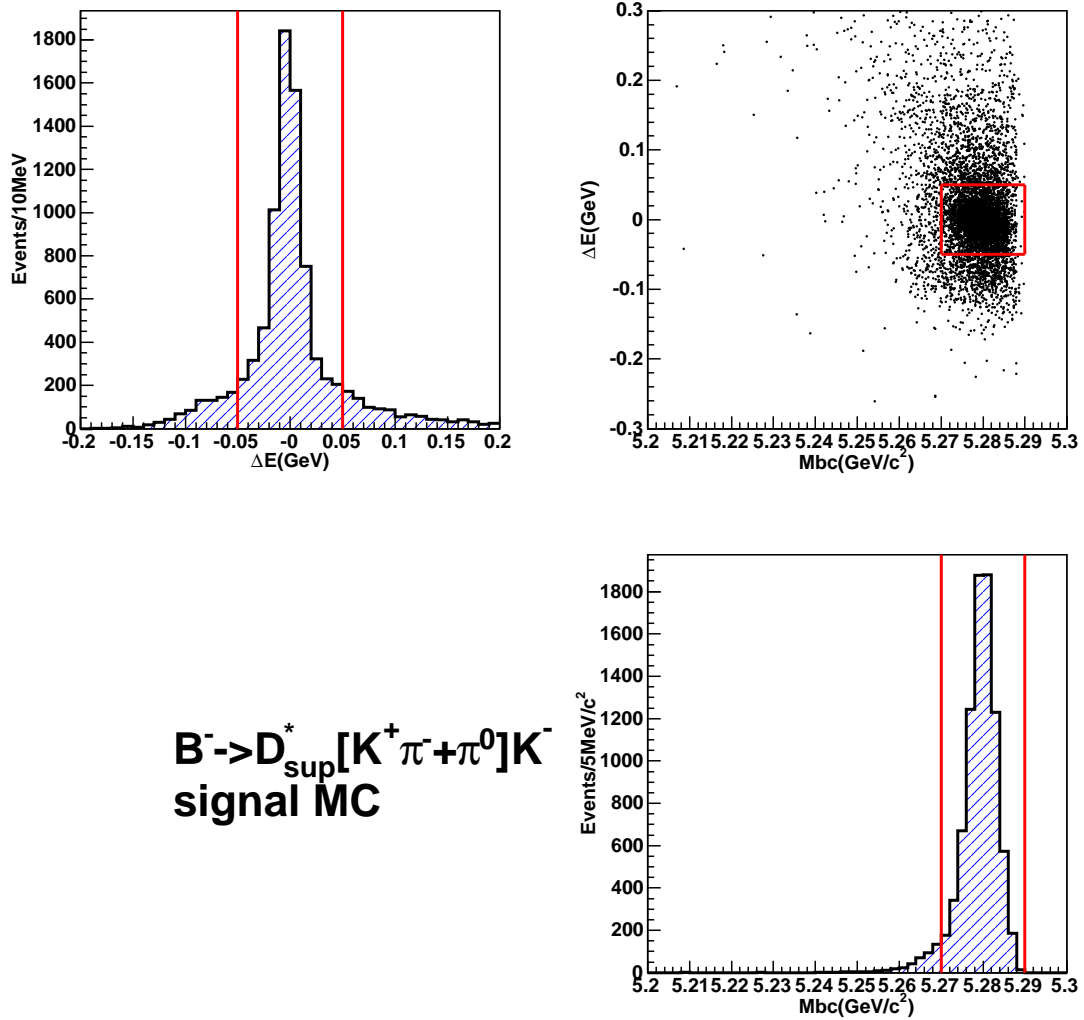


Figure 5.3: ΔE and M_{bc} distribution of signal Monte Carlo events in $B^- \rightarrow D^*[D\pi^0]K^-$ mode

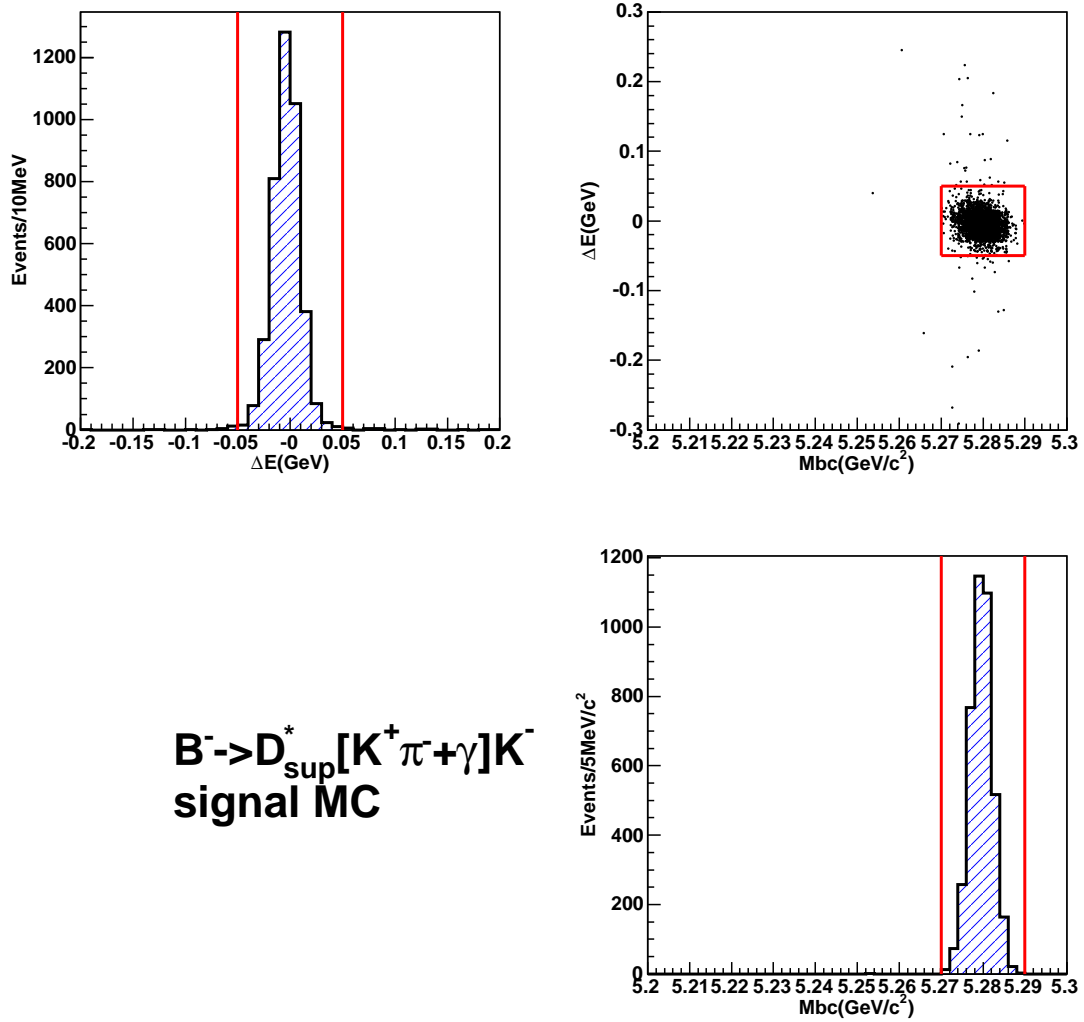


Figure 5.4: ΔE and M_{bc} distributions of signal Monte Carlo events in $B^- \rightarrow D^*[D\gamma]K^-$

ratio distribution of signal Monte Carlo and M_{bc} sideband data and F.o.M distribution as a function of likelihood ratio cut point for each mode. The number of $q\bar{q}$ continuum background events is estimated from Monte Carlo. On the other hand the number of signal events is estimated from PDG product branching fraction as

$$\begin{aligned}\mathcal{B}(B^- \rightarrow D^{*0}\pi^- / D^{*0}K^-) &= 4.6 \times 10^{-3} / 3.6 \times 10^{-4} \\ \mathcal{B}(D^{*0} \rightarrow D^0\pi^0 / D^0\gamma) &= \frac{2}{3} / \frac{1}{3} \\ \mathcal{B}(D^0 \rightarrow K^-\pi^+ / K^+\pi^-) &= 3.8 \times 10^{-2} / 1.38 \times 10^{-4}\end{aligned}$$

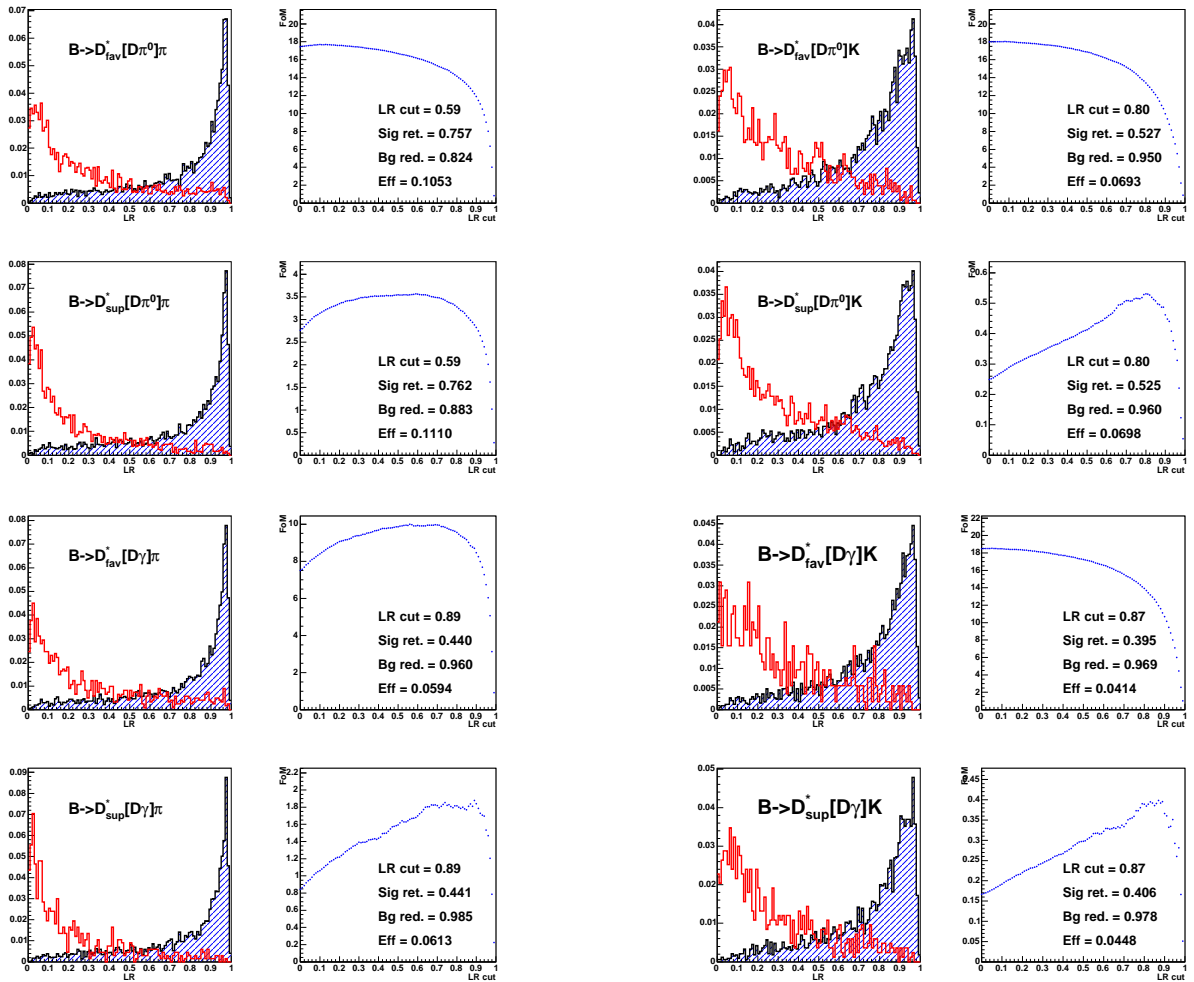


Figure 5.5: Event shape likelihood ratio distribution(left) and The "figure of merit" distribution(right). $B^- \rightarrow D^*[D\pi^0]\pi^-$ (top right), $B^- \rightarrow D^*[D\pi^0]K^-$ (top left), $B^- \rightarrow D^*[D\gamma]\pi^-$ (bottom right) and $B^- \rightarrow D^*[D\gamma]K^-$ (bottom left).

5.1.4 Peaking background

To check the peaking background "generic Monte Carlo" events and "rare Monte Carlo" events are used as shown in 5.6 and Figure 5.7, respectively. But in signal region particular background source is not found.

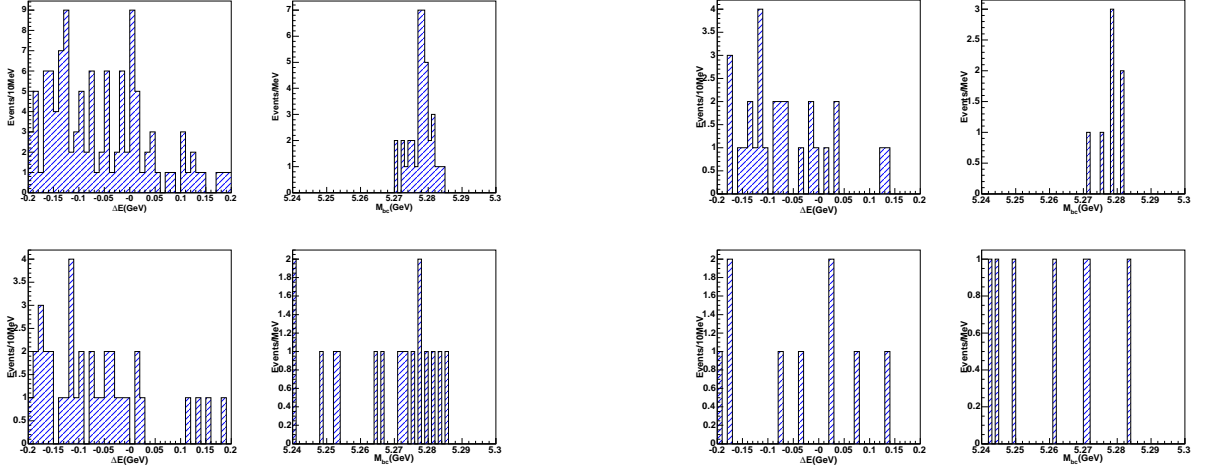


Figure 5.6: ΔE and M_{bc} distributions of "generic Monte Carlo" evnts. $B^- \rightarrow D^*[D\pi^0]\pi^-$ (top right), $B^- \rightarrow D^*[D\pi^0]K^-$ (top left), $B^- \rightarrow D^*[D\gamma]\pi^-$ (bottom right) and $B^- \rightarrow D^*[D\gamma]K^-$ (bottom left).

5.2 Results

5.2.1 Fitting the ΔE distributions

In $B^- \rightarrow D_{fav}^*[D\pi^0]\pi^-$, $B^- \rightarrow D_{fav}^*[D\pi^0]K^-$, $B^- \rightarrow D_{fav}^*[D\gamma]\pi^-$ and $B^- \rightarrow D_{fav}^*[D\gamma]K^-$ decay mode, backgrounds from other B decays distribute as shown in Figure 5.8. The treatments of background, $B\bar{B}$ background and continuum background, is same as $B^- \rightarrow DK^-$ analysis. For fit of signal the sum of two Gaussian distributions which have same mean are used where its relative width and area are determined from signal Monte Carlo.

In the fit of the ΔE distribution for $B^- \rightarrow D_{fav}^*h^-$ mode, the free parameters are the position, widths and area of the signal peak, the slope and normalization of the continuum component and the normalization of the $B\bar{B}$ background.

For $B^- \rightarrow D_{sup}^*h^-$, the signal and $B\bar{B}$ background shapes are modeled using the results of the fits to the corresponding favored modes. The free parameters are the normalization of the three components, and the slope of the continuum.

The fit results are shown in Figure 5.9 and Figure 5.10. The numbers of signal yield are listed in Table 5.2

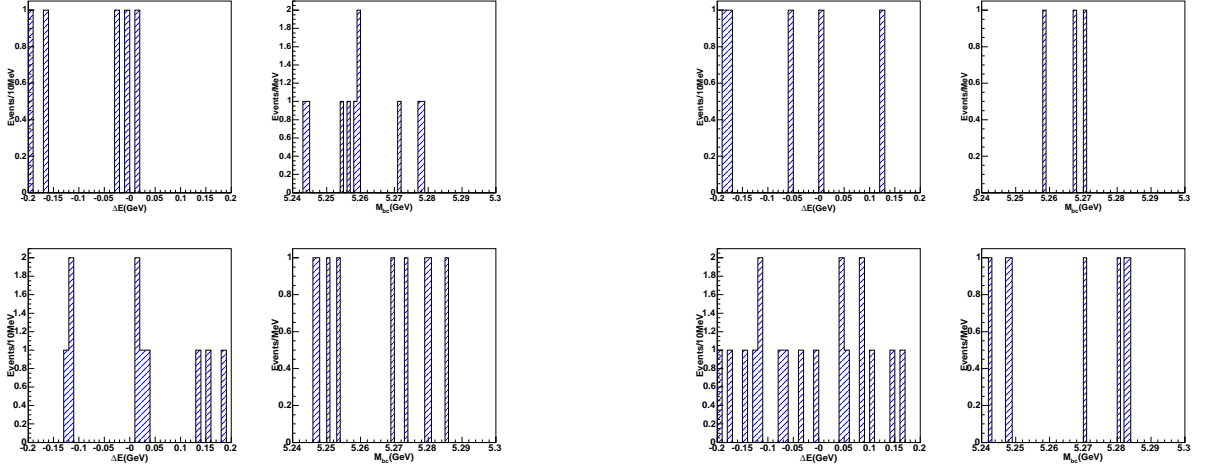


Figure 5.7: ΔE and M_{bc} distributions of "rare Monte Carlo" evnts. $B^- \rightarrow D^*[D\pi^0]\pi^-$ (top right), $B^- \rightarrow D^*[D\pi^0]K^-$ (top left), $B^- \rightarrow D^*[D\gamma]\pi^-$ (bottom right) and $B^- \rightarrow D^*[D\gamma]K^-$ (bottom left).

Mode	Efficiency(%)	Signal Yield
$B^- \rightarrow D_{fav}^*[D\pi^0]\pi^-$	10.5 ± 0.2	4801 ± 82
$B^- \rightarrow D_{sup}^*[D\pi^0]\pi^-$	11.1 ± 0.2	23.6 ± 6.8
$B^- \rightarrow D_{fav}^*[D\pi^0]K^-$	6.9 ± 0.2	176 ± 18.7
$B^- \rightarrow D_{sup}^*[D\pi^0]K^-$	7.0 ± 0.2	0.0 ± 0.0
$B^- \rightarrow D_{fav}^*[D\gamma]\pi^-$	5.9 ± 0.2	1481 ± 52
$B^- \rightarrow D_{sup}^*[D\gamma]\pi^-$	6.1 ± 0.2	4.4 ± 4.2
$B^- \rightarrow D_{fav}^*[D\gamma]K^-$	4.1 ± 0.1	43.4 ± 8.9
$B^- \rightarrow D_{sup}^*[D\gamma]K^-$	4.5 ± 0.1	2.9 ± 1.8

Table 5.2: Efficiency and signal yields.

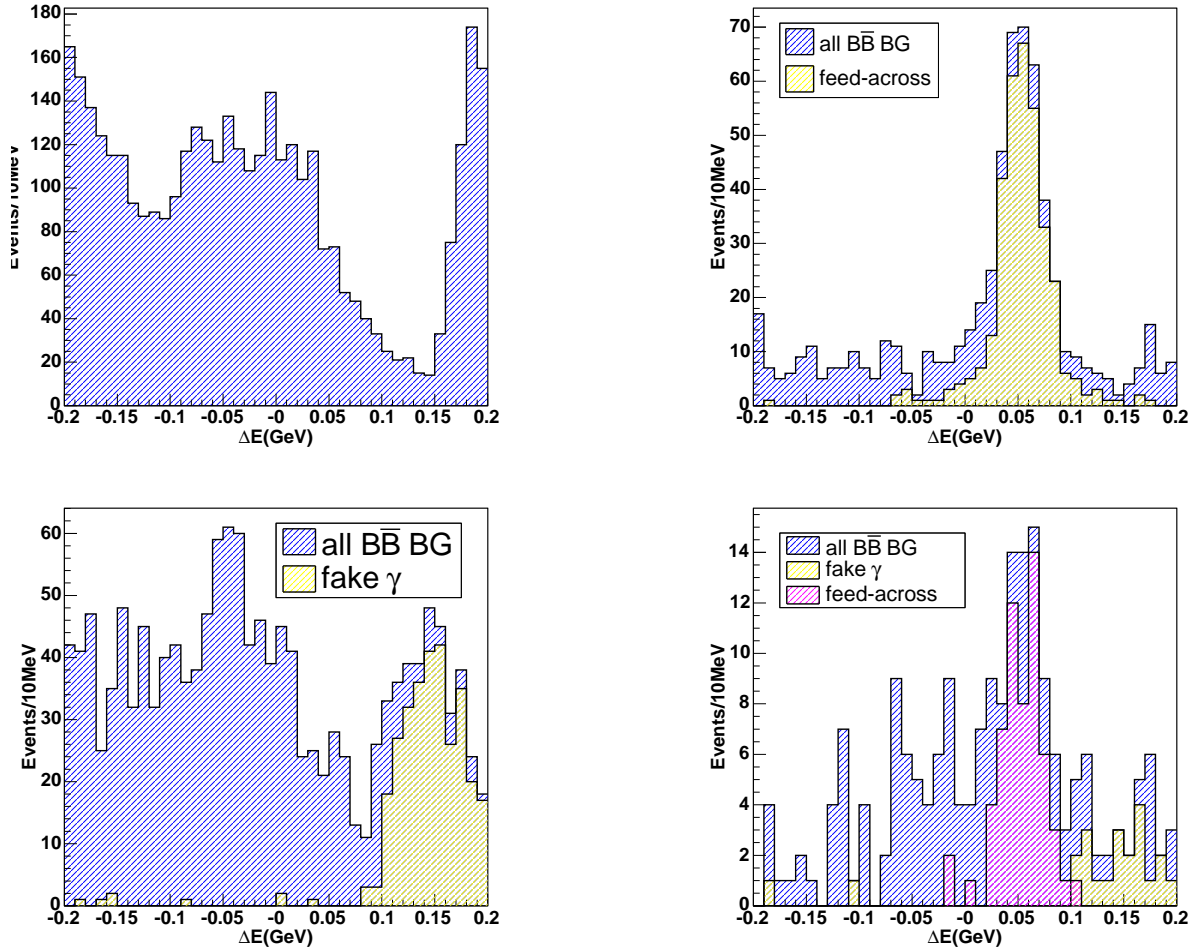
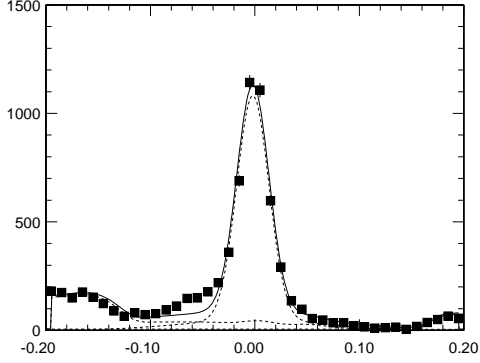


Figure 5.8: ΔE distributions of $B\bar{B}$ background. $B^- \rightarrow D_{fav}^*[D\pi^0]\pi^-$ (top right), $B^- \rightarrow D_{fav}^*[D\pi^0]K^-$ (top left), $B^- \rightarrow D_{fav}^*[D\gamma]\pi^-$ (bottom right) and $B^- \rightarrow D_{fav}^*[D\gamma]K^-$ (bottom left).

MINUIT Likelihood Fit to Plot 101&10
 de
 File: rec_dstpl.rz
 Plot Area Total/Fit 7141.0 / 7141.0
 Func Area Total/Fit 7026.2 / 7026.2
 15-DEC-2005 09:38
 Fit Status 3
 E.D.M. 8.154E-09

Likelihood = 317.3
 $\chi^2 = 349.9$ for 40 - 6 d.o.f.,
 C.L. = 0.00 %

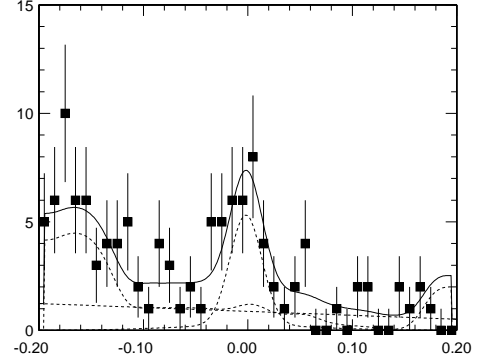
Errors	Parabolic	Minos	
Function 1: Two Gaussians (sigma)			
AREA	4800.8 ± 82.49	- 82.01	+ 82.80
MEAN	-1.87791E-03 ± 3.0543E-04	- 3.0191E-04	+ 3.0035E-04
SIGMA1	1.53928E-02 ± 3.2193E-04	- 3.1710E-04	+ 3.2543E-04
* AR2/AREA	0.16837 ± 0.000	- 0.000	+ 0.000
* DELM	0.0000 ± 0.000	- 0.000	+ 0.000
* SIG2/SIG1	4.4889 ± 0.000	- 0.000	+ 0.000
Function 2: Polynomial of Order 1			
NORM	1261.7 ± 118.0	- 0.000	+ 0.000
* POLY01	-181.00 ± 0.000	- 0.000	+ 0.000
OFFSET	3.9258 ± 0.6983	- 0.000	+ 0.000
Function 3: Smooth Histogram 201 31(1) Normal errors			
NORM	1.8276 ± 6.2421E-02	- 6.2057E-02	+ 6.2337E-02
* OFFSET	0.0000 ± 0.000	- 0.000	+ 0.000



MINUIT Likelihood Fit to Plot 102&20
 de
 File: rec_dstpl.rz
 Plot Area Total/Fit 117.00 / 117.00
 Func Area Total/Fit 112.88 / 112.88
 15-DEC-2005 09:39
 Fit Status 3
 E.D.M. 8.333E-07

Likelihood = 41.2
 $\chi^2 = 34.4$ for 40 - 4 d.o.f.,
 C.L. = 54.3%

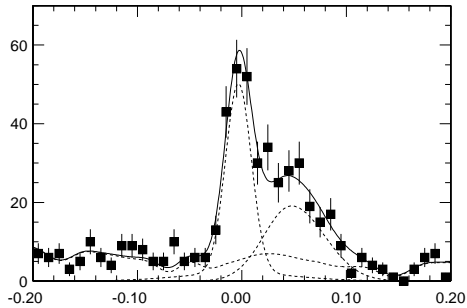
Errors	Parabolic	Minos	
Function 1: Two Gaussians (sigma)			
AREA	23.582 ± 6.839	- 6.471	+ 7.219
* MEAN	-1.87791E-03 ± 0.000	- 0.000	+ 0.000
* SIGMA1	1.53928E-02 ± 0.000	- 0.000	+ 0.000
* AR2/AREA	0.16837 ± 0.000	- 0.000	+ 0.000
* DELM	0.0000 ± 0.000	- 0.000	+ 0.000
* SIG2/SIG1	4.4889 ± 0.000	- 0.000	+ 0.000
Function 2: Polynomial of Order 1			
NORM	68.131 ± 524.7	- 0.000	+ 0.000
* POLY01	-181.00 ± 0.000	- 0.000	+ 0.000
OFFSET	0.10689 ± 2.898	- 0.000	+ 0.5442
Function 3: Smooth Histogram 201 31(1) Normal errors			
NORM	4.9417E-02 ± 1.0701E-02	- 1.0449E-02	+ 1.0963E-02
* OFFSET	0.0000 ± 0.000	- 0.000	+ 0.000



MINUIT Likelihood Fit to Plot 101&10
 de
 File: rec_dstk.rz
 Plot Area Total/Fit 513.00 / 513.00
 Func Area Total/Fit 513.03 / 513.03
 2-FEB-2006 09:35
 Fit Status 3
 E.D.M. 1.035E-06

Likelihood = 39.3
 $\chi^2 = 37.4$ for 40 - 6 d.o.f.,
 C.L. = 31.5%

Errors	Parabolic	Minos	
Function 1: Two Gaussians (sigma)			
AREA	176.36 ± 18.68	- 18.08	+ 19.29
MEAN	-3.18989E-03 ± 1.6007E-03	- 1.5499E-03	+ 1.6626E-03
SIGMA1	5.39874E-02 ± 6.3516E-03	- 5.9466E-03	+ 6.7765E-03
* AR2/AREA	0.84354 ± 0.000	- 0.000	+ 0.000
* DELM	0.0000 ± 0.000	- 0.000	+ 0.000
* SIG2/SIG1	0.22841 ± 0.000	- 0.000	+ 0.000
Function 2: Bifurcated Gaussian (sigma)			
AREA	138.92 ± 17.43	- 17.14	+ 17.73
* MEAN	4.75517E-02 ± 0.000	- 0.000	+ 0.000
* SIGA	2.63686E-02 ± 0.000	- 0.000	+ 0.000
* SIGB	3.16026E-02 ± 0.000	- 0.000	+ 0.000
Function 3: Chebyshev Polynomial of Order 1			
NORM	8.5838 ± 104.2	- 0.000	+ 109.6
* CHEB01	-3.22289E-02 ± 0.000	- 0.000	+ 0.000
Function 4: Smooth Histogram 201 31(1) Normal errors			
NORM	0.67141 ± 0.1588	- 0.1604	+ 7.9872E-02
* OFFSET	0.0000 ± 0.000	- 0.000	+ 0.000



MINUIT Likelihood Fit to Plot 102&20
 de
 File: rec_dstk.rz
 Plot Area Total/Fit 21.000 / 21.000
 Func Area Total/Fit 20.997 / 20.997
 2-FEB-2006 09:43
 Fit Status 3
 E.D.M. 3.046E-06

Likelihood = 43.0
 $\chi^2 = 45.9$ for 40 - 4 d.o.f.,
 C.L. = 12.5%

Errors	Parabolic	Minos	
Function 1: Two Gaussians (sigma)			
AREA	9.07919E-11 ± 3.4832E-05	- 0.000	+ 1.682
* MEAN	-3.17838E-03 ± 0.000	- 0.000	+ 0.000
* SIGMA1	5.39874E-02 ± 0.000	- 0.000	+ 0.000
* AR2/AREA	0.84354 ± 0.000	- 0.000	+ 0.000
* DELM	0.0000 ± 0.000	- 0.000	+ 0.000
* SIG2/SIG1	0.22841 ± 0.000	- 0.000	+ 0.000
Function 2: Bifurcated Gaussian (sigma)			
AREA	0.93904 ± 3.163	- 0.000	+ 3.429
* MEAN	4.75517E-02 ± 0.000	- 0.000	+ 0.000
* SIGA	2.63686E-02 ± 0.000	- 0.000	+ 0.000
* SIGB	3.16026E-02 ± 0.000	- 0.000	+ 0.000
Function 3: Chebyshev Polynomial of Order 1			
NORM	4.86370E-08 ± 1.4127E-03	- 0.000	+ 10.03
* CHEB01	-0.10040 ± 0.000	- 0.000	+ 0.000
Function 4: Smooth Histogram 201 31(1) Normal errors			
NORM	6.92712E-02 ± 1.8643E-02	- 1.8886E-02	+ 1.9398E-02
* OFFSET	0.0000 ± 0.000	- 0.000	+ 0.000

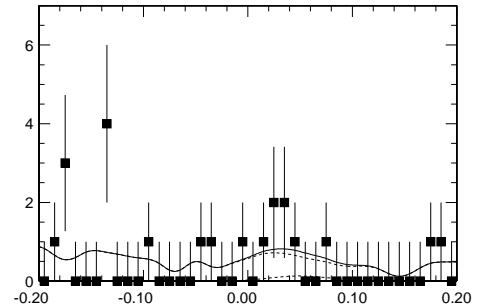
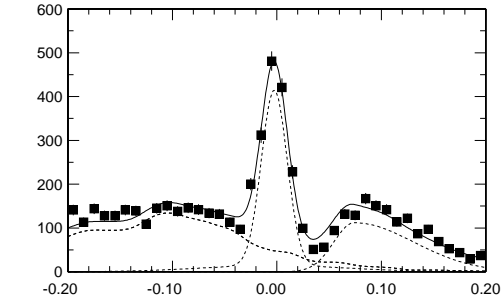


Figure 5.9: ΔE -fit result. $B^- \rightarrow D_{fav}^*[D\pi^0]\pi^-$ (top right), $B^- \rightarrow D_{sup}^*[D\pi^0]\pi^-$ (top left), $B^- \rightarrow D_{fav}^*[D\pi^0]K^-$ (bottom right), $B^- \rightarrow D_{sup}^*[D\pi^0]K^-$ (bottom left).

MINUIT Likelihood Fit to Plot 101&10
 de
 File: rec_dstpl.rz 17-JAN-2006 10:16
 Plot Area Total/Fit 5556.0 / 5556.0 Fit Status 3
 Func Area Total/Fit 5555.4 / 5555.4 E.D.M. 1.622E-07

Likelihood = 104.4
 $\chi^2 = 102.9$ for 40 - 7 d.o.f., C.L.=0.417E-06%

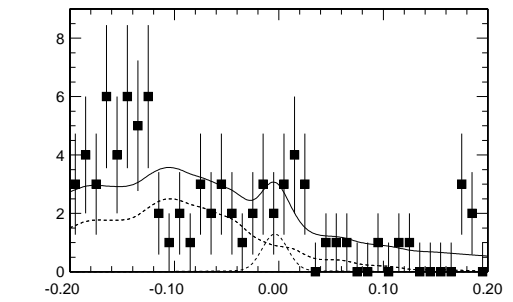
Errors	Parabolic	Minos	
Function 1: Two Gaussians (sigma)			
AREA	1480.6 ± 52.16	- 51.21	+ 51.97
MEAN	-2.43193E-03 ± 4.7466E-04	- 4.7270E-04	+ 4.7155E-04
SIGMA1	6.87301E-02 ± 2.3507E-03	- 2.2945E-03	+ 2.3587E-03
* AR2/AREA	0.83348 ± 0.000	- 0.000	+ 0.000
* DELM	0.0000 ± 0.000	- 0.000	+ 0.000
* SIG2/SIG1	0.17303 ± 0.000	- 0.000	+ 0.000
Function 2: Bifurcated Gaussian (sigma)			
AREA	1073.0 ± 64.78	- 65.14	+ 65.15
* MEAN	7.4000E-02 ± 0.000	- 0.000	+ 0.000
* SIGA	1.94073E-02 ± 0.000	- 0.000	+ 0.000
* SIGB	5.70325E-02 ± 0.000	- 0.000	+ 0.000
Function 3: Polynomial of Order 1			
NORM	1967.7 ± 237.4	- 0.000	+ 0.000
* POLY01	-181.00 ± 0.000	- 0.000	+ 0.000
OFFSET	-0.53380 ± 0.8400	- 0.000	+ 0.000
Function 4: Smooth Histogram 201 31(1) Normal errors			
NORM	0.64367 ± 2.7859E-02	- 2.8121E-02	+ 2.7713E-02
* OFFSET	0.0000 ± 0.000	- 0.000	+ 0.000



MINUIT Likelihood Fit to Plot 102&20
 de
 File: rec_dstpi.rz 17-JAN-2006 10:54
 Plot Area Total/Fit 82.000 / 82.000 Fit Status 3
 Func Area Total/Fit 81.608 / 81.608 E.D.M. 5.930E-06

Likelihood = 42.0
 $\chi^2 = 41.6$ for 40 - 5 d.o.f., C.L.= 20.6%

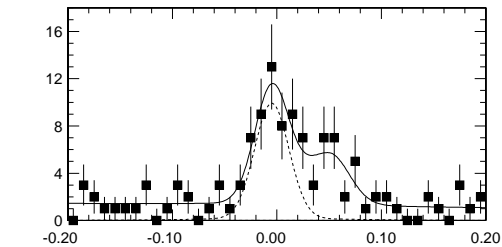
Errors	Parabolic	Minos	
Function 1: Two Gaussians (sigma)			
AREA	4.4019 ± 4.176	- 3.806	+ 4.562
* MEAN	-3.78409E-03 ± 0.000	- 0.000	+ 0.000
* SIGMA1	7.07619E-02 ± 0.000	- 0.000	+ 0.000
* AR2/AREA	0.86352 ± 0.000	- 0.000	+ 0.000
* DELM	0.0000 ± 0.000	- 0.000	+ 0.000
* SIG2/SIG1	0.17073 ± 0.000	- 0.000	+ 0.000
Function 2: Bifurcated Gaussian (sigma)			
AREA	2.76371E-06 ± 4.0139E-03	- 0.000	+ 1.403
* MEAN	7.4000E-02 ± 0.000	- 0.000	+ 0.000
* SIGA	1.94073E-02 ± 0.000	- 0.000	+ 0.000
* SIGB	5.70325E-02 ± 0.000	- 0.000	+ 0.000
Function 3: Polynomial of Order 1			
NORM	65.243 ± 393.1	- 0.000	+ 0.000
* POLY01	-181.00 ± 0.000	- 0.000	+ 0.000
OFFSET	0.12063 ± 2.174	- 0.000	+ 0.5003
Function 4: Smooth Histogram 201 31(1) Normal errors			
NORM	1.19850E-02 ± 3.0338E-03	- 2.9929E-03	+ 3.0921E-03
* OFFSET	0.0000 ± 0.000	- 0.000	+ 0.000



MINUIT Likelihood Fit to Plot 101&10
 de
 File: rec_dstk.rz 2-FEB-2006 09:39
 Plot Area Total/Fit 118.00 / 118.00 Fit Status 3
 Func Area Total/Fit 117.98 / 117.98 E.D.M. 1.673E-05

Likelihood = 33.0
 $\chi^2 = 27.4$ for 40 - 7 d.o.f., C.L.= 74.4%

Errors	Parabolic	Minos	
Function 1: Two Gaussians (sigma)			
AREA	43.372 ± 8.870	- 9.440	+ 9.381
MEAN	-4.82808E-03 ± 3.8529E-03	- 3.8065E-03	+ 4.0206E-03
SIGMA1	7.55542E-02 ± 1.5571E-02	- 1.4249E-02	+ 1.8506E-02
* AR2/AREA	0.92495 ± 0.000	- 0.000	+ 0.000
* DELM	0.0000 ± 0.000	- 0.000	+ 0.000
* SIG2/SIG1	0.21724 ± 0.000	- 0.000	+ 0.000
Function 2: Bifurcated Gaussian (sigma)			
AREA	9.20502E-07 ± 7.1255E-03	- 0.000	+ 5.322
* MEAN	7.46458E-02 ± 0.000	- 0.000	+ 0.000
* SIGA	1.72062E-02 ± 0.000	- 0.000	+ 0.000
* SIGB	6.49166E-02 ± 0.000	- 0.000	+ 0.000
Function 3: Bifurcated Gaussian (sigma)			
AREA	23.958 ± 7.263	- 6.937	+ 7.627
* MEAN	5.01873E-02 ± 0.000	- 0.000	+ 0.000
* SIGA	2.50828E-02 ± 0.000	- 0.000	+ 0.000
* SIGB	1.88688E-02 ± 0.000	- 0.000	+ 0.000
Function 4: Chebyshev Polynomial of Order 1			
NORM	126.70 ± 22.57	- 34.07	+ 23.83
* CHEB01	-0.14420 ± 0.000	- 0.000	+ 0.000
Function 5: Smooth Histogram 201 31(1) Normal errors			
NORM	2.06913E-09 ± 5.6220E-05	- 0.000	+ 0.1478
* OFFSET	0.0000 ± 0.000	- 0.000	+ 0.000



MINUIT Likelihood Fit to Plot 102&20
 de
 File: rec_dstk.rz 2-FEB-2006 09:39
 Plot Area Total/Fit 4.0000 / 4.0000 Fit Status 3
 Func Area Total/Fit 4.0000 / 4.0000 E.D.M. 3.973E-09

Likelihood = 9.8
 $\chi^2 = 33.5$ for 40 - 5 d.o.f., C.L.= 54.1%

Errors	Parabolic	Minos	
Function 1: Two Gaussians (sigma)			
AREA	2.9414 ± 1.786	- 1.465	+ 2.142
* MEAN	-4.82808E-03 ± 0.000	- 0.000	+ 0.000
* SIGMA1	7.55542E-02 ± 0.000	- 0.000	+ 0.000
* AR2/AREA	0.92495 ± 0.000	- 0.000	+ 0.000
* DELM	0.0000 ± 0.000	- 0.000	+ 0.000
* SIG2/SIG1	0.21724 ± 0.000	- 0.000	+ 0.000
Function 2: Bifurcated Gaussian (sigma)			
AREA	2.95929E-11 ± 3.4188E-05	- 0.000	+ 0.5220
* MEAN	7.46458E-02 ± 0.000	- 0.000	+ 0.000
* SIGA	1.72062E-02 ± 0.000	- 0.000	+ 0.000
* SIGB	6.49166E-02 ± 0.000	- 0.000	+ 0.000
Function 3: Bifurcated Gaussian (sigma)			
AREA	5.29308E-10 ± 3.4188E-05	- 0.000	+ 0.5519
* MEAN	5.01873E-02 ± 0.000	- 0.000	+ 0.000
* SIGA	2.50828E-02 ± 0.000	- 0.000	+ 0.000
* SIGB	1.88688E-02 ± 0.000	- 0.000	+ 0.000
Function 4: Chebyshev Polynomial of Order 1			
NORM	2.6511 ± 2.856	- 2.025	+ 3.876
* CHEB01	-0.10504 ± 0.000	- 0.000	+ 0.000
Function 5: Smooth Histogram 201 31(1) Normal errors			
NORM	1.11295E-12 ± 1.999E-07	- 0.000	+ 8.9807E-03
* OFFSET	0.0000 ± 0.000	- 0.000	+ 0.000

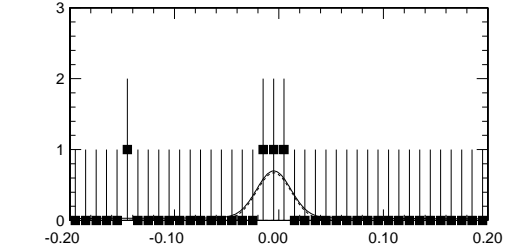


Figure 5.10: ΔE -fit result. $B^- \rightarrow D_{fav}^* [D\gamma] \pi^-$ (top right), $B^- \rightarrow D_{sup}^* [D\gamma] \pi^-$ (top left), $B^- \rightarrow D_{fav}^* [D\gamma] K^-$ (bottom right), $B^- \rightarrow D_{sup}^* [D\gamma] K^-$ (bottom left).

5.2.2 Ratio of branching fractions R_{Dh}

In $B^- \rightarrow D^*K^-$ mode the ratio of product branching fraction is calculated using the number of signal events and efficiency listed in Table 5.2.

The ratios are obtained as

$$R_{D^*[D\pi^0]\pi^-} = (4.6 \pm 1.4(stat)) \times 10^{-3},$$

$$R_{D^*[D\pi^0]K^-} = 0.0 \pm 0.0(stat) \pm 0.0(sys)$$

$$R_{D^*[D\gamma]\pi^-} = (2.8 \pm 2.8(stat)) \times 10^{-3},$$

$$R_{D^*[D\gamma]K^-} = (6.7 \pm 4.3(stat)) \times 10^{-2}.$$

In this mode using the identity [19]

$$r_{B,D^*K}^2 = \frac{R_{D^*[D\pi^0]K} + R_{D^*[D\gamma]K}}{2} - r_D^2$$

r_{B,D^*K} is calculated as

$$r_{B,D^*K} = 0.17 \pm 0.07(stat) \pm 0.04(sys)$$

The systematic error comes from each yield extractions and is estimated in the same way as $B^- \rightarrow DK^-$ analysis. And we also compare this result with one of Belle Dalitz analysis [4] and BaBar [14]. These results are consistent within these errors.

$$\text{Belle Dalitz analysis : } r_{B,DK} = 0.20_{-0.17}^{+0.19}(stat) \pm 0.02(sys) \pm 0.04(model) \quad (5.1)$$

$$\text{BaBar : } r_{B,DK} = 0.06_{-0.09}^{+0.12} \quad (5.2)$$

Moreover the upper limit is set as

$$r_{B,D^*K} < 0.31 \text{ at the } 90\% \text{ confidence level.}$$

5.2.3 Constraint for ϕ_3

Using the value of r_{B,DK^*} and Belle measurement for $B^- \rightarrow D_{CP}^*K^-$ [10] as bellow, a constraint for ϕ_3 and δ is determined.

$$A_1 = -0.27 \pm 0.25(stat) \pm 0.04(sys) \quad (5.3)$$

$$A_2 = 0.26 \pm 0.26(stat) \pm 0.03(sys) \quad (5.4)$$

$$R_1 = 1.43 \pm 0.28(stat) \pm 0.06(sys) \quad (5.5)$$

$$R_2 = 0.94 \pm 0.28(stat) \pm 0.06(sys) \quad (5.6)$$

The same method as $B^- \rightarrow DK^-$ analysis is used to give a constraint for $\phi - \delta$. The result as shown in Figure 5.11 is obtained.

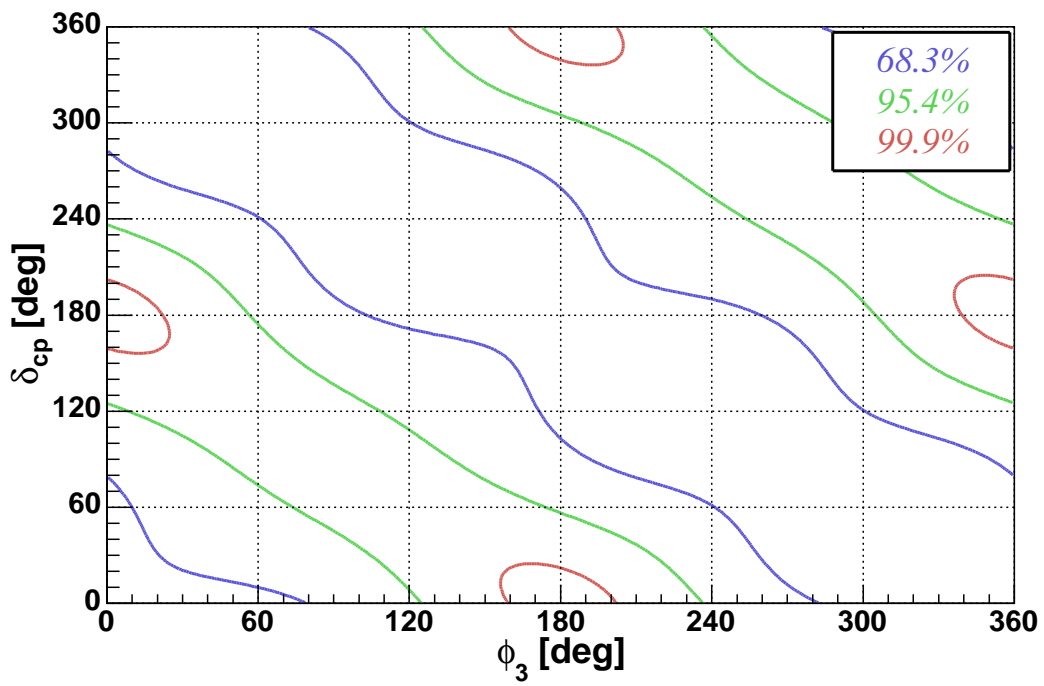


Figure 5.11: Constraint for ϕ_3 and δ . These contours show favored region of each confidence levels.

Chapter 6

Combining fit result

ϕ_3 fit combining $B^- \rightarrow DK^-$, $B^- \rightarrow DK^{*-}$ and $B^- \rightarrow D^*K^-$ is performed using χ^2 method. Its result is obtained as Figure 6.1.

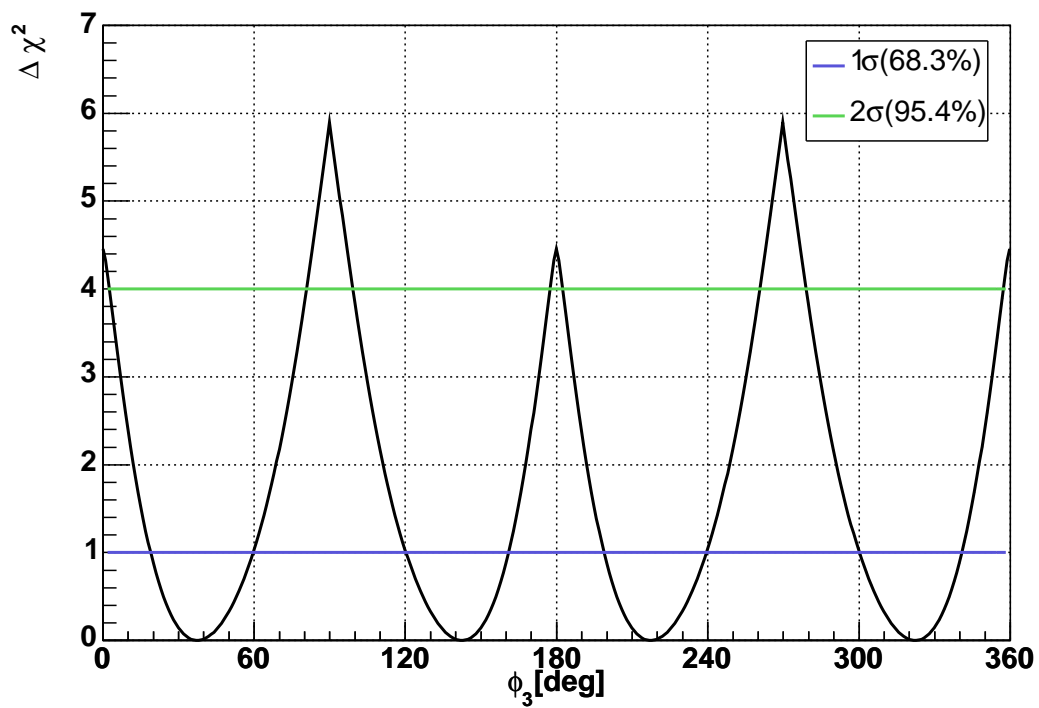


Figure 6.1: Constraint for ϕ_3

Chapter 7

Conclusions

In this thesis we searched suppressed decay modes such as $B^- \rightarrow D_{sup}K^-$, $B^- \rightarrow D_{sup}K^{*-}$ and $B^- \rightarrow D_{sup}^*K^-$. We can't find any significant signal.

So we set upper limits for $R_{Dh} = \frac{B^- \rightarrow D_{sup}h^-}{B^- \rightarrow D_{fav}h^-}$ and $r_B = \left| \frac{B^- \rightarrow \bar{D}^0 K^-}{B^- \rightarrow D^0 K^-} \right|$. Using these results and results of $B^- \rightarrow D_{CP}K^-$ analysis, we perform constraints for ϕ_3 and r_B s. Up to now although this method doesn't give a certain constraint for ϕ_3 because of small statistics, the new method of ϕ_3 measurement is established. This fact is important.

Acknowledgments

I can not express my acknowledgments for many people with my English ability. So I want to express it in Japanese.

まずはじめに、指導教官となり、このようなとてもチャレンジングなテーマを与えていただいた山本均先生、ならびにこの高エネルギー物理という素敵な世界へ誘っていた山口晃先生には本当にお世話になりました。この修士論文を一人で書き上げるまでに成長出来たのは、まさに先生方の指導の賜物です。長嶺忠先生には、常日頃からコンピュータのテクニカルな問題や物理に関する質問に応じていただき、大変助かりました。Jerriさんには、Belleの解析について分からない事があったときに、度々助けて頂き、ありがとうございました。

2003年泡箱幼稚園入園、2006年卒園(2006年2月16日現在では予定)の安東慎一郎くん、小川桃世さん、藤川智暁くん、竹内慎くんには同期として様々な面で助けられました。安東くんには度々KEKまでのドライバーとなってもらったこと、そして居るだけで癒し系の不思議なところはきっと忘れません。藤川君はリニアコライダーの研究になってしまい、研究の事で直接話す事はあまりありませんでしたが、その研究に伴う困難を乗り越える藤川君の姿は、何かと将来の明るくないこのご時世、「自分の力を信じればなんとかなる」という一筋の光を僕に与えてくれました。KamLANDグループの竹内くん、小川さんのB II グループとは異なる日々研究に真摯に取り組む姿勢は、おなじ学生として大きな励みになりました。さらに、小川さんにはなぜかKamLANDについて詳しくなってしまうような機会を与えて頂いた事に感謝します。また、KamLANDグループのスタッフの池田晴雄さん、榎本三四郎さん、丸藤祐仁さん、岸本康宏さん、清水格さん、吉田斉さん、中島亨さんにはおそらく忙しいにも関わらず、スキーに連れて行って頂いたり、解析上の相談にのって頂いたり、おやつを持ってきて頂き、ありがとうございました。さらに、2004年泡箱幼稚園入園の中島恭平くん、谷宣廣くんには忙しい中、僕の修論を手伝ってもらい、大変助かりました。

KEKで僕の研究を支え、アドバイスを頂き、時に無茶とも言える注文だしていただいたTim Gershonさん、阿部和雄さん、Karim Trabelsiさん、堺井義秀さん、Tom Browderさんには深く感謝したいと思います。同じKLMグループとして中野英一さん、三上恵成さん、遊佐洋右さん、Tapas Sarangiさんには数々のご迷惑おかけしつつも、常に助けてくださり、ありがとうございました。また、物理をする以外なんにも無いKEKで、心が枯れてしまいそうな僕と遊んでくれた、井本絢子お姉様、日下暁人さん、でいびつとくん、藤川美幸希さん、藤山幸生くん、森隆志さん、渡辺みのりさんには多いに助けられました。と

くに渡辺みのりさんには例え忘れようとしても、忘れさせてもらえないだけのご恩があります。

東北大の学部以来の(悪?)友である飯沢洋平くん、大嵐浩暢くん、小川洋人くんとは数々の思い出となるような出来事とともに過ごせた事を多分誇りに思います。さらに長い付き合いの、小北諭くん、斎木真くん、三井寛之くんには、僕が人生をあらん方向に歩もうとした時に、力一杯背中を押してくれた事に対し、心よりの感謝を表したいと思います。また、 M^2 さんには色々な面で助けて頂き、ありがとうございました。

最後に、この修論を書き上げるまで精神面、経済面で常に僕を支えてくれた父、母にこっ恥ずかしいですがこの場を借りて、心よりありがとうございましたと言いたいと思います。

Appendix A

Cotinum background suppression

Thrust angle

Firstly we determine the thrust axis which is maximize the projection momentums of daughter particles in signal candidate and the others. Then we calculate the angle between these axes. In the case of $B\bar{B}$ event it distributes flat. On the other hand in the case of $q\bar{q}$ event it makes peak in the edge.

Super Fox-Wolfram method / SFW

Super Fox-Wolfram method [20] are composed of Fisher discriminant with super Fox-wolfram moments. Super Fox-Wolfram moments are defined as

$$H_n \equiv \sum_{i,j} |\vec{p}_i^*| |\vec{p}_j^*| P_n(\cos \theta_{ij}) \quad (\text{A.1})$$

where \vec{p}^* is momentum in the CM system, indices distinguish particles in a event, θ_{ij} is a decay angle and P_n is n -th Legendre polynomial.

H_n is decomposed to 3 components expediently

$$H_n \equiv H_n^{ss} + H_n^{so} + H_n^{oo} \quad (\text{A.2})$$

$$H_n^{ss} \equiv \sum_{i,j} |\vec{p}_i^*| |\vec{p}_j^*| P_n(\cos \theta_{ij}) \quad (\text{A.3})$$

$$H_n^{so} \equiv \sum_{j,k} |\vec{p}_j^*| |\vec{p}_k^*| P_n(\cos \theta_{jk}) \quad (\text{A.4})$$

$$H_n^{oo} \equiv \sum_{k,l} |\vec{p}_k^*| |\vec{p}_l^*| P_n(\cos \theta_{kl}). \quad (\text{A.5})$$

where i and j represent tracks of signal candidate and k and l represent ones of remaining tracks in a event. In Belle Fisher discriminant is used using six term Fow-Wolfram moments

as

$$SFW = \sum_{n=2,4} \alpha_n \frac{H_n^{so}}{H_o^{so}} + \sum_{n=1}^4 \beta_n \frac{H_n^{oo}}{H_o^{oo}} \quad (\text{A.6})$$

where α_n and β_n are Fisher coefficients which maximize the separation between signal and background. Here H_n for $n > 4$ is not used because of less ability of separation between signal and continuum. And H_1^{so} , H_3^{so} and H_n^{ss} are also not used because of strong correlations with M_{bc} od ΔE .

improved Super Fox-Wolfram method / KSFW

To suppress continuum background effectively KSFW is developed [20]. KSFW is defined as

$$KSFW \equiv \sum_{l=0}^4 R_l^{so} + \sum_{l=0}^4 R_l^{oo} + \gamma \sum_{n=1}^{N_t} |p_{t,n}| \quad (\text{A.7})$$

where p_t is transverse momentum, N_t is the number of tracks in a event and γ is Fisher coefficient.

- R_l^{so}

In this method H_l^{so} is decomposed to 3 components, "charged", "neutral" and "missing".

$$R_l^{so} \equiv \frac{(\alpha_c)_l (H_{\text{charged}})_l^{so} + (\alpha_n)_l (H_{\text{neutral}})_l^{so} + (\alpha_c)_l (H_{\text{missing}})_l^{so}}{E_{beam} - \Delta E} \quad (\text{A.8})$$

For $l = 1$ and 3,

$$(H_{\text{charged}})_l^{so} \equiv \sum_i \sum_j \beta_l^{so} Q_i Q_j |\vec{p}_j| P_l(\cos \theta_{ij}) \quad (\text{A.9})$$

$$(H_{\text{neutral}})_l^{so} = H_{\text{missing}} = 0 \quad (\because Q=0) \quad (\text{A.10})$$

For $l = 0, 2$ and 4,

$$(H_{\text{charged,neutral,missing}})_l^{so} \equiv \sum_i \sum_j \beta_l^{so} |\vec{p}_j| P_l(\cos \theta_{ij}) \quad (\text{A.11})$$

The index i iterates over the tracks of signal candidate and the index j iterates over same category(charged, neutral or missing) tracks of the rest. Q_i is charge of particle i . In these equation α and β are fisher coefficients. So there are 11 parameters ($(l = 0, 3) \times (\text{charged}) + (l = 0, 2, 4) \times (\text{charged, neutral, missing}) = 2 \times 1 + 3 \times 3$) in the R_l^{so} optimization

- R_l^{oo}
For $l = 1, 3$

$$R_l^{oo} \equiv \frac{\sum_j \sum_k \beta_l^{oo} Q_j Q_k |p_j| |p_k| P_l(\cos \theta_{jk})}{(E_{beam} - \Delta E)^2} \quad (\text{A.12})$$

For $l = 0, 2, 4$

$$R_l^{oo} \equiv \frac{\sum_j \sum_k \beta_l^{oo} |p_j| |p_k| P_l(\cos \theta_{jk})}{(E_{beam} - \Delta E)^2} \quad (\text{A.13})$$

In these equation index j and k iterate over the rest tracks of the signal candidate. There are 5 parameters in optimaizatoin.

- $\sum_{n=1}^{N_t} |p_{t,n}|$
This is the sum of transverse momentum in a event. This has a optimization coefficient.

This method has totally 17 ($= 11 + 5 + 1$) parameters. And empirically the value of "KSFW" strongly depends on mm^2 defined as

$$mm^2 = (E_{\Upsilon(4S)} - \sum_i E_i)^2 - \sum_i |p_i|^2. \quad (\text{A.14})$$

So in optimization of these parameters mm^2 regions are divided to 7 regions ($-0.5 \sim 6.0[\text{GeV}]$).

Appendix B

Figure of merit technique

In physics analysis we need the indicator to optimize a cut value. Figure of merit(F.o.M) is a good indicator. It's defined as

$$F.o.M = \frac{S}{\sqrt{S + N}}$$

,where S is number of signal and N is number of background.

This roughly means the significance of the signal. Because if we get number of total events, $S + N$, its fluctuation is about $\sqrt{S + N}$. So if number of signal is S , its significance is represented as $S/\sqrt{S + N}$. Then by optimization based on this technique we can get signal with higher significance.

For example, let's consider ΔE -fit under the condition as

$$\left\{ \begin{array}{ll} \text{signal shape} & : \text{ gaussian} \\ \#(\text{signal}) & = 30 \\ \sigma_{\text{signal}} & = 0.01 \\ \text{background shape} & : \text{ constant} \\ \#(\text{background}) : N(x) & = 7 \end{array} \right.$$

and make ΔE distribution sample using random numbers as Figure B.1.

Actually I do ΔE -fit for this sample and calculate the significance. And changing the integration range of background we know the range which equalize F.o.M to significance. In this sample when we integrate the background within $2.2\sigma_{\text{signal}}$ the F.o.M is equal to the signal significance.

To confirm this statically I repeat this process 1000 times as Figure B.2. By this if we integrate the background within 2.3σ we can get the F.o.M closing to significance.

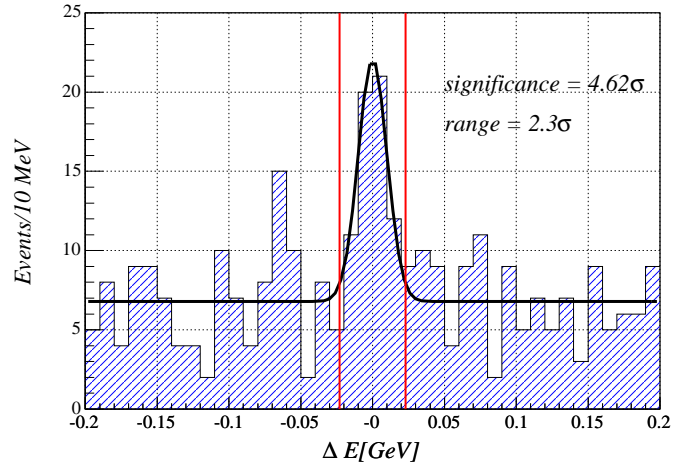


Figure B.1: ΔE distribution using random numbers.

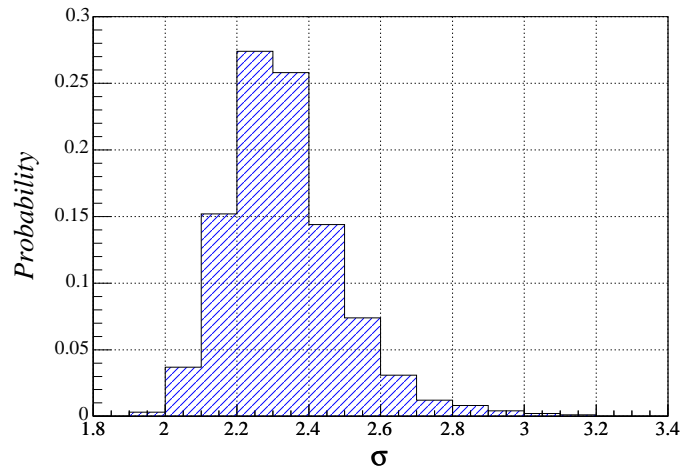


Figure B.2: Integration range of background estimation

Bibliography

- [1] M. Kobayashi and T. Masukawa, *Prog.Theor.Phys.* 49, 652 (1973).
- [2] L.Wolfenstein and F.Wu, *Europhys.Lett.* 58, 49 (2002).
- [3] A.Giri, Yu.Grossman, A.Soffer and j.Zupan, *Phys.Rev. D* 68, 0504018 (2003)
- [4] Belle Collaboration, A.Poluektov et al., *Phys.Rev. D* 70, 072003 (2004)
- [5] M. Gronau and D. Wyler, *Phys.Lett. B* 165, 172 (1991); M. Gronau and D. London, *Phys.Lett. B* 253, 483 (1991).
- [6] D. Atwood, I. Dunietz, and A. Soni, *Phys. Rev. Lett.* 78, 3257 (1997); *Phys. Rev. D* 63, 036005 (2001).
- [7] Belle Collaboration, P.Krokovny et al., hep-ex/0212066 (2002), Belle Collaboration, K.Abe et al., *Phys.Rev.Lett.* 87, 111801 (2001).
- [8] Particle Data Group, S. Eidelman et al., *Phys.Lett. B* 592, 1 (2004).
- [9] Belle collaboration, A. Abashian et al., *Nucl.Instrum.Meth. A* 479 117-232 (2002).
- [10] Belle collaboration, M. Saigo et al., *Phys.Rev.Lett.* 94, 091601 (2005).
- [11] K. Huitu, C.D. Lu, P. Singer, D.X. Zhang, *Phys.Rev.Lett.* 81, 4313 (1998).
- [12] Belle Collaboration, S.K.Swain et al., *Phys.Rev. D* 68, 051101 (2003).
- [13] Belle Collaboration, K.Abe et al., hep-ex/0601032 (2005).
- [14] BaBar collaboration, B. Aubert et al., hep-ex/0504047.
- [15] Heavy Flavor Averaging Group, <http://www.slac.stanford.edu/xorg/hfag> (2005).
- [16] Belle Collaboration, K.Abe et al., hep-ex/0504013 (2005).
- [17] BaBar collaboration, B. Aubert et al., *Phys.Rev. D* 72, 071104 (2005).

- [18] BaBar collaboration, B. Aubert et al., hep-ex/0507002 (2005).
- [19] Alex Bondar and Tim Gershon, *Phys.Rev. D* 70, 091503 (2004).
- [20] N.Abe(Tokyo Institute of Technology), Doctor thesis (2003).